CHEMICAL REVIEWS

pubs.acs.org/CR

Review

Isotope Labels Combined with Solution NMR Spectroscopy Make Visible the Invisible Conformations of Small-to-Large RNAs

Theodore K. Dayie,* Lukasz T. Olenginski, and Kehinde M. Taiwo

Cite This: *Chem. Rev.* 2022, 122, 9357−9394

Read Online

ACCESS | Metrics & More | Article Recommendations

ABSTRACT: RNA is central to the proper function of cellular processes important for life on earth and implicated in various medical dysfunctions. Yet, RNA structural biology lags significantly behind that of proteins, limiting mechanistic understanding of RNA chemical biology. Fortunately, solution NMR spectroscopy can probe the structural dynamics of RNA in solution at atomic resolution, opening the door to their functional understanding. However, NMR analysis of RNA, with only four unique ribonucleotide building blocks, suffers from spectral crowding and broad linewidths, especially as RNAs grow in size. One effective strategy to overcome these challenges is to introduce NMR-active stable isotopes into RNA. However, traditional uniform labeling methods introduce scalar and dipolar couplings that complicate the implementation and analysis of NMR measurements. This challenge can be circumvented with selective isotope labeling. In this review, we outline the development of labeling technologies and their application to study biologically relevant RNAs and their complexes ranging in size from 5 to 300 kDa by NMR spectroscopy.

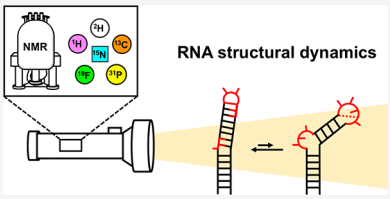

CONTENTS

Special Issue: Biomolecular NMR Spectroscopy

Received: September 30, 2021
Published: April 20, 2022

https://doi.org/10.1021/acs.chemrev.1c00845
Chem. Rev. 2022, 122, 9357−9394

1. INTRODUCTION

RNA is central to medicine, chemical and structural biology, and basic research. For more than a half-century, it has been known that the code of life is imprinted in DNA sequences, following the so-called "sequence hypothesis", usually wrongly labeled as the "central dogma" in the popular parlance.[1] In the last several decades, it has become increasingly clear that the functions of cells are also transacted by DNA's lesser-known relative, RNA.[2] Indeed, the varied roles that RNAs play in both normal and dysfunctional cells have motivated RNA-based therapeutic development, as highlighted by the recent SARS COV-2 mRNA vaccines.[3−9] Additionally, RNAs are central to the workings of molecular nanomachines such as the ribosome[10−12] and the spliceosome[13−15] to name a few. Moreover, thanks to the advent of genomic sequencing efforts, we now understand that the amount of RNA sequence transcribed in humans exceeds the number of protein sequences translated by at least 50-fold (Figure 1A).[16] Paradoxically, the number of RNA-only structures deposited in the Protein Data Bank (PDB) remains below 1%, whereas the number of protein-only structures is a staggering 87% (Figure 1B). This paucity undercuts current understanding of RNA structure−function relationships.

Nuclear magnetic resonance (NMR) spectroscopy accounts for ∼35% of the RNA structures deposited in the PDB and ∼7% of the protein structures, making it competitive with other biophysical tools such as X-ray crystallography and more recently cryo-electron microscopy (cryo-EM) (Figure 1C).[17] Moreover, NMR spectroscopy provides high-resolution structural dynamic information in solution, rendering it an ideal tool to study RNA and its interactions with macromolecules or small drug-like compounds or both.[18−25] However, unlike proteins, which are made up of 20 unique amino acid building blocks, RNAs are composed of only four aromatic nucleotides [i.e., adenosine (Ade or A), guanosine (Gua or G), cytidine (Cyt or C), and uridine (Uri or U)] that resonate over a very narrow chemical shift region. This poor chemical shift dispersion is further exacerbated with increasing RNA size. To overcome these limitations, novel isotope labeling strategies that incorporate atom-specific labels (e.g., uridine ^{13}C6) or expand the number of NMR probes beyond the traditional ^{1}H−^{15}N and ^{1}H−^{13}C spin pairs (e.g., ^{13}C−^{19}F) have been developed.

In this review, we will outline the development of isotope labeling technologies for RNA NMR and some of the exciting new applications enabled by these labels to study small-to-large RNAs. Specifically, we will begin by detailing the benefits afforded by each common NMR-active isotope (Section 2). Next, we outline the various technologies that incorporate such labels into RNA building blocks and eventually into RNA (Section 3). This discussion will center around chemoenzymatic labeling, a method that our group has extensively developed for the past near-decade. Next, we will examine how these labels benefit dynamics measurements (Section 4) and can be leveraged to study interactions involving large RNA systems (Section 5). Finally, to conclude, we will comment on how isotope labeling can advance the field of RNA chemical and structural biology (Section 6).

2. STABLE ISOTOPES IN NMR SPECTROSCOPY

Frederick Soddy is credited with coining the word "isotope" from the Greek *isos* (ἴσος) and *topos* (τόπος) meaning "same place",[26] with the idea that stable isotopes are chemical elements that occupy the same position in the periodic table but differ in mass due to a different number of neutrons within the atomic nucleus. Stable isotopes have been used in a wide range of applications in industry, academia, and medicine.[26] In particular, stable isotopes have significantly impacted methods such as NMR and mass spectrometry (MS). For this work, we will focus on how these probes impact RNA NMR spectroscopy, with special emphasis on proton (hydrogen-1 or ^{1}H), deuterium (hydrogen-2 or ^{2}H), carbon-13 (^{13}C), nitrogen-15 (^{15}N), fluorine-19 (^{19}F), and phosphorus-31 (^{31}P) (Table 1).

2.1. Proton Isotope

The proton isotope has high natural abundance (∼100%) and the highest sensitivity of NMR receptive and stable nuclei (Table 1). Therefore, homonuclear two-dimensional (2D) ^{1}H−^{1}H NMR methods were attractive in the early days of NMR analysis. However, the very limited resolution of ribose and aromatic nucleobase resonances in the RNA ^{1}H spectra restricted such studies to small RNAs (<5 kDa). Within the ribose, all protons with the exception of H1′ (i.e., H2′, H3′, H4′, H5′, and H5′′) are clustered within a narrow ∼0.6−0.8 ppm range (Figure 2A).[29] Within the nucleobase, the chemical shift distribution of all protons is limited to 1 ppm or less, except for imino protons with a dispersion of ∼4 ppm (Figure 2A).[30,31] Taken together, the distribution of proton resonances leads to severe chemical shift overlap that worsens as RNAs grow in size due to increased line broadening (Figure 2B). This, in part, explains the paucity of NMR structures of large RNAs (e.g., > 60 nt) (Figure 2C).

2.2. Heteronuclear ^{15}N and ^{13}C Isotopes

Unlike protons, with a chemical shift span of 2−15 ppm, ^{15}N and ^{13}C nuclei in nucleic acids have larger chemical shift distributions among the various atomic sites. For example, ^{13}C nuclei in RNA have chemical shifts from 61 (C5′-ribose) to 170 (nonprotonated pyrimidine nucleobase C4) ppm, and ^{15}N nuclei from 70 (amino nitrogen) to 240 (nonprotonated purine nucleobase N7) ppm.[29−31] Introduction of the ^{15}N isotope (0.37%) into RNA nucleobases circumvents the extensive line broadening arising from the electric quadrupole moment of the naturally abundant ^{14}N isotope (99.63%) (Table 1). Incorporation of the ^{15}N isotope has several additional advantages. As a spin 1/2 nucleus with low gyromagnetic ratio (γ) (Table 1), the ^{15}N isotope provides very narrow spectral lines. Nitrogen atoms, like protons and carbon, are distributed in nucleic acid major and minor grooves, and both grooves serve as important sites for metal, drug, or macromolecule interactions. However, given the wider chemical shift dispersion of ^{15}N over the ^{1}H nucleus and its narrower linewidths over ^{13}C and ^{1}H nuclei, ^{15}N is more suited to monitor those grooves, especially in larger RNAs. However, nitrogen's low-γ is also an "Achilles heel". In the absence of appropriate NMR cryogenic probes and the availability of high magnetic fields, detecting low-γ nuclei such as ^{15}N has been very unattractive. Increasing the availability of such probes is expected to reverse this trend. Nevertheless, these considerations suggest that the shortcomings of proton NMR can be overcome by heteronuclear NMR methods.[32]

https://doi.org/10.1021/acs.chemrev.1c00845
Chem. Rev. 2022, 122, 9357−9394

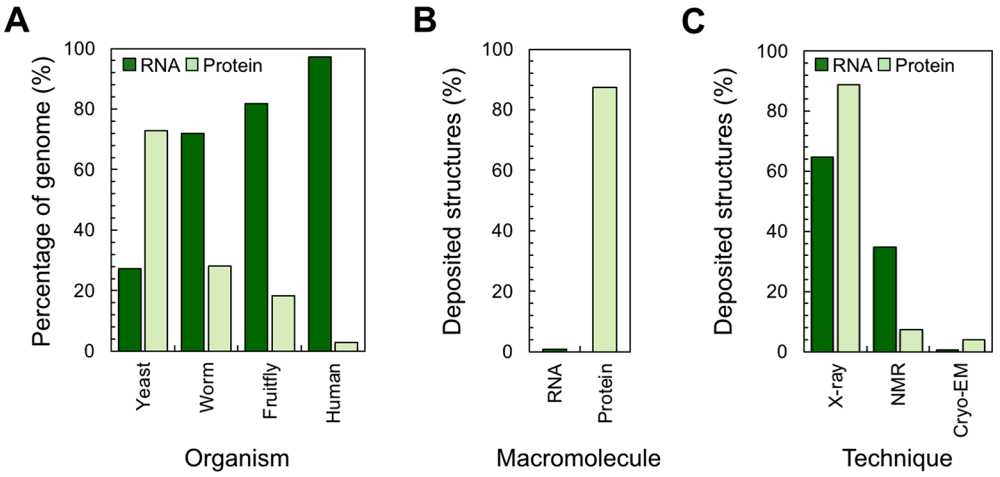

Figure 1. (A) Percentage of protein coding and nonprotein coding genomic material in selected genomes.[16] Organismal complexity increases with RNA coding but decreases with protein coding capacity as a percentage of the DNA genomic output. (B) Percentage of RNA-only and protein-only structures deposited in the PDB. Given that this analysis excluded DNA-only structures and structures of protein−DNA/RNA complexes, the percentages do not sum to 100%. (C) Percentage of RNA-only and protein-only structures deposited in the Nucleic Acid Database (NDB) and PDB, sorted by structure determination technique. Given that this analysis is self-contained within categories, the percentages sum to 100%. NMR accounts for a larger fraction of RNA structures as compared to proteins. PDB and NDB statistics were accessed from https://www.rcsb.org/ and http://ndbserver.rutgers.edu/ in January 2022.

Beginning in the 1980s, several groups introduced ^{15}N, ^{2}H, and ^{13}C labels to facilitate NMR studies of RNAs and proteins.[33−42] Depending on the scientific question, these labels were introduced uniformly or selectively using bacteria *in vivo* or enzyme catalyzed synthesis *in vitro*. Selective enrichment was achieved by growing auxotrophs on obligate chemically synthesized compounds. ^{13}C-labeling of bacterial tRNAs[33−35] and ^{15}N-labeling of tRNA and 5S rRNA enabled various atomic sites in these RNAs to be monitored by NMR. Uniform ^{15}N-labeling was also applied to 5S rRNA *in vivo*.[36−39] To extend this labeling to additional RNAs, several research groups developed *in vitro* methods to convert ribonucleoside 5′-monophosphates isolated from bacteria grown on ^{15}N-, ^{2}H-, and ^{13}C-sources into the corresponding triphosphates for *in vitro* transcription.[43−47] These uniform ^{15}N- and ^{13}C-labeling technologies did extend the use of NMR to medium-sized RNAs (MW < 20 kDa). However, two perennial challenges of low signal-to-noise and decreased spectral resolution remained. The latter problem arises from the reintroduction of spectral overlap along the heteronuclear dimension as the RNA grows in size, and the former arises from increased relaxation that results from the slower overall tumbling of large biomolecules. The next section will describe recent labeling methods to overcome both problems.

2.3. Deuteration in Context of Heteronuclear ^{15}N and ^{13}C Isotopes

Deuteration (i.e., replacement of protons with deuterons) simplifies the multiplicity of spin−spin interactions, eliminates nonessential resonance lines, reduces spectral crowding, helps to identify coupling patterns, and improves calculation of coupling constants with precision.[48] Given the smaller γ of the deuterium spin relative to proton ($\gamma_D \approx \gamma_H/6.5$) (Table 1), the relaxation rates for deuterated nuclei are scaled proportionally by 2% [$(\gamma_D/\gamma_H)^2 \approx 0.02$]. By eliminating competing relaxation pathways of dipolar coupled protons, deuteration suppresses spin diffusion within a relaxation network, leading to smaller linewidths and higher signal-to-noise for the remaining protons and directly attached ^{13}C and ^{15}N nuclei.[47−49] Given these advantages, ^{2}H-labeling has played an important role in probing the structure, dynamics, and interactions of large RNAs by NMR.[17,50−55]

Table 1. Stable Isotopes Relevant to RNA NMR Spectroscopy[27,28]

isotope	natural abundance (%)	γ (rad Hz T^{-1})	spin
^{1}H	99.99	26.752×10^7	1/2
^{2}H	0.01	4.107×10^7	1
^{12}C	98.90	NMR inactive	NMR inactive
^{13}C	1.10	6.728×10^7	1/2
^{14}N	99.63	1.934×10^7	1
^{15}N	0.37	-2.713×10^7	1/2
^{19}F	100.00	25.181×10^7	1/2
^{31}P	100.00	10.839×10^7	1/2

2.4. Fluorination in Context of ^{15}N, ^{2}H, and ^{13}C Isotopes

In addition to ^{2}H, magnetically active nuclei such as ^{19}F have valuable spectroscopic properties that confer clear advantages in the study of macromolecular structure and conformational changes.[56] These benefits include the 100% natural abundance of ^{19}F (Table 1), a comparably large γ (94% of ^{1}H) (Table 1), and a superior chemical shift dispersion that is ∼6-fold that of ^{1}H.[18,57] Furthermore, ^{19}F is sensitive to changes in its local chemical environment, making it a useful probe of conformational changes.[18,56,57] Finally, fluorine has an atomic radius (1.35 Å) slightly larger than that of a hydrogen (1.20 Å) but slightly smaller than that of a methyl group (2.00 Å). The ^{19}F nuclei is therefore expected to substitute for either group without serious structural perturbations,[58] making it a valuable tool for the *in vitro* study of medically important RNAs.[59] Finally, ^{19}F is virtually absent in biological systems and therefore offers ^{19}F NMR a biorthogonal advantage of background-free drug screening.[60] Taken together, ^{19}F is an attractive probe for studying RNAs in solution. Details of new technologies developed to incorporate ^{19}F into nucleobases

https://doi.org/10.1021/acs.chemrev.1c00845
Chem. Rev. 2022, 122, 9357−9394

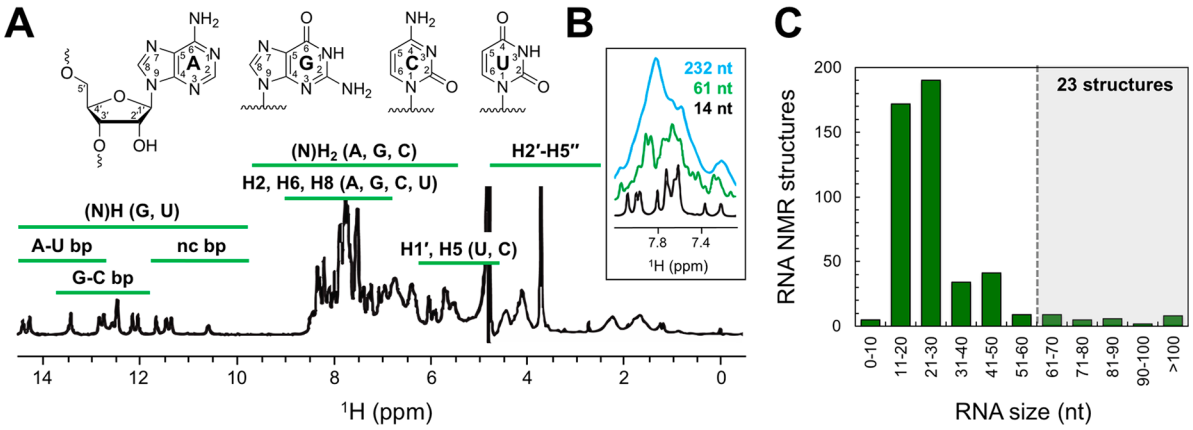

Figure 2. (A) ^{1}H NMR spectrum of a 61 nt RNA emphasize the narrow chemical shift dispersion of RNA protons. Here, bp and nc refer to canonical Watson−Crick base pair and noncanonical base pairs, respectively. A schematic of RNA ribose and nucleobase structures and numbering are shown above the spectrum. (B) Nucleobase region of ^{1}H NMR spectra for RNAs of increasing size. Both signal overlap and broad linewidths worsen as RNAs grow in size. In fact, for the best visual representation, the signals corresponding to the 61 and 232 nt RNAs were increased to display them on a similar scale to that of the 14 nt RNA. (C) Histogram of RNA NMR structures in the NDB, sorted by RNA size (in nt, bin = 10 nt). Given the challenges faced by RNA NMR, there are only 23 NMR structures corresponding to RNAs > 60 nt. NDB statistics were accessed from http://ndbserver.rutgers.edu/ in January 2022.

Scheme 1. Synthetic Route to [6-^{13}C, 5-^{2}H]-Uracil[82,85]

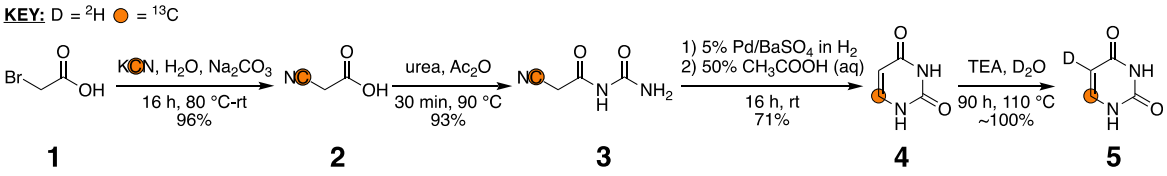

will be presented in Section 3.1.1, and its utility to expand NMR studies to larger RNAs will be discussed in Section 5.

3. PREPARATION OF ^{15}N, ^{2}H, ^{13}C, AND ^{19}F ISOTOPE-LABELED RNA

A number of companies (Cassia LLC, Cambridge Isotope Laboratories (CIL), INNotope, Sigma-Aldrich, and Silantes) offer isotope-labeled RNA building blocks with uniform and selective labeling. However, most comprehensive labels are made by academic laboratories using biochemical, biomass, chemical, and chemo-enzymatic approaches, as reviewed in the past.[61−67] In this section, we outline promising developments in the chemical synthesis of isotope-labeled purine [i.e., adenine (Ade or A) and guanine (Gua or G)] and pyrimidine [i.e., cytosine (Cyt or C) and uracil (Ura or U) (in RNA) or thymine (Thy or T) (in DNA)] nucleobases and their incorporation into RNA. The main approaches to obtain isotope-labeled RNA are enzymatic or solid-phase chemical synthesis. The enzymatic approach involves DNA template-directed T7 RNA polymerase-based *in vitro* transcription using ribonucleoside 5′-triphosphates (rNTPs).[44,45,68−76] The alternative method is chemical solid-phase synthesis using RNA phosphoramidites (amidites).[77−80] Both methods can use unlabeled and isotope-labeled building blocks (rNTPs and amidites) to generate versatile RNA labeling patterns, as recently reviewed.[61,62,66,67]

3.1. Chemical Synthesis of Nucleobases

In this section, we give a general overview of the chemical synthetic methods to label RNA nucleobases at specific positions with ^{15}N, ^{2}H, ^{13}C, and ^{19}F isotopes. These nucleobases can then serve as the building blocks for the synthesis of the rNTPs or amidites that enable the eventual enzymatic or chemical production of labeled RNAs of defined sequence and length.

3.1.1. Specific ^{13}C Labeling. *3.1.1.1. Pyrimidine Synthesis with ^{15}N, ^{2}H, ^{13}C, and ^{19}F Labels.* The uracil nucleobase is easily assembled using a method initially devised by Roberts and Poulter,[81] later streamlined by SantaLucia and Tinoco and co-workers,[71] and further improved by Kreutz and co-workers.[82] In the original synthetic eight-step pathway described by Roberts and Poulter, the ^{13}C label can be placed in any position of the six-membered ring simply by changing the ^{13}C-source.[81] SantaLucia and Tinoco and co-workers streamlined this to a three-step reaction scheme to make ^{13}C-labeled cyanoacetyl urea from inexpensive commercially available ^{13}C-labeled precursors.[71] A slightly modified approach from Kreutz and co-workers uses bromoacetic rather than chloroacetic acid. Bromoacetic acid is the preferred starting material due to the lower costs and better handling of the cyanide reagent.[74,82] Other methods with fewer steps exist such as condensation of malic or propiolic acid and urea.[83,84] Even though these are straightforward two-step reactions, execution is not as convenient or cost-effective.

Using the Poulter-SantaLucia-Kreutz approach,[71,74,81,82] [1-^{13}C]- and [2-^{13}C]-bromoacetic acid selectively incorporate ^{13}C at uracil C4 and C5, respectively. Use of ^{13}C-urea, on the other hand, delivers ^{13}C at the C2 site, and that of ^{13}C-potassium cyanide (^{13}C-KCN) labels the C6 site. Finally, ^{15}N-urea installs ^{15}N at N1 and N3. All possible uracil heteroatom positions can therefore be labeled in good yields, and these reactions can be easily scaled to gram quantities.[74,82] An example of a synthetic scheme using the Poulter-SantaLucia-Kreutz approach[71,74,81,82] is shown for uracil C6 labeling

https://doi.org/10.1021/acs.chemrev.1c00845
Chem. Rev. 2022, 122, 9357−9394

Scheme 2. Synthetic Route to [6-^{2}H]-5FU[18,57,82,85,86]

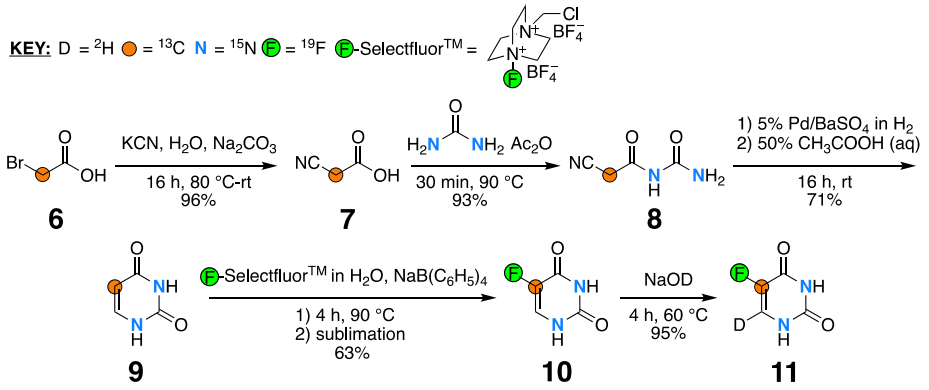

Scheme 3. Synthetic Route to [6-^{13}C]-Thymine[89]

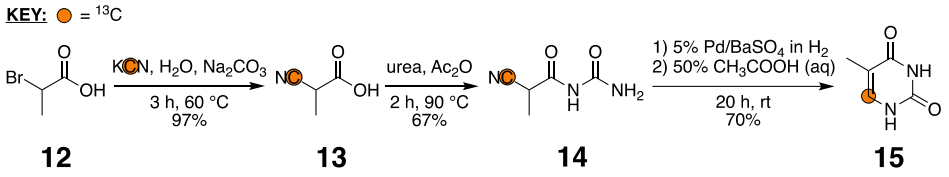

(Scheme 1).[82,85] In brief, bromoacetic acid **1** reacts with ^{13}C-KCN and sodium carbonate (Na_2CO_3) in a Kolbe nitrile reaction to form 2-[cyano-^{13}C]acetic acid **2**. Treatment of **2** with urea in the presence of acetic anhydride (Ac_2O) then yields a urea intermediate **3** that can be readily converted to [6-^{13}C]-uracil **4** using a palladium catalyst (e.g., Pd/$BaSO_4$) under hydrogen atmosphere (H_2). Given that pyrimidine H5/H6 protons have three-bond scalar coupling ($^{3}J_{H5/H6} \approx 8$ Hz[29]) and strong dipolar coupling (H5−H6 distance of 2 Å) that complicate NMR experiments, selective and quantitative deuteration can be achieved by reacting **4** with triethylamine (TEA) to form the desired [6-^{13}C, 5-^{2}H]-uracil **5**.[85] Taken together, **5** was synthesized with four-steps in 63% overall yield (Scheme 1).[82,85]

Given the valuable spectroscopic properties of ^{19}F (Section 2.4), uracil can be fluorinated with the commercially available Selectfluor, as recently reported.[18,57,86] This synthetic scheme is similar to that described for uracil C6 labeling (Scheme 1),[82,85] except using [2-^{13}C]-bromoacetic acid **6** as starting material. Kolbe nitrile reaction of **6** forms an intermediate **7** that reacts with ^{15}N-urea and Ac_2O to yield **8**. Addition of Pd/$BaSO_4$ in H_2 to **8** then forms [5-^{13}C, 1,3-$^{15}N_2$]-uracil **9**, which can then be fluorinated with Selectfluor to yield [5-^{13}C, 5-^{19}F, 1,3-$^{15}N_2$]-uracil (5FU) **10**. Again, selective and quantitative deuteration of H6 can remove coupling ($^{3}J_{H6F5} \approx 7.1$ Hz[88]) that complicates NMR spectra by heating **10** 5FU in sodium deuteroxide (NaOD) to form [6-^{2}H]-5FU **11**.[18,86,87] In summary, **11** was synthesized in five-steps with a total yield of 38% (Scheme 2).[18,57,82,85,86]

Finally, thymine C6 can be selectively labeled with a three-step synthesis in a manner similar to uracil labeling (Schemes 1 and 2).[18,57,82,85,86] In brief, bromopropionic acid **12** is used in a Kolbe nitrile reaction followed by addition of urea and Ac_2O to form intermediates **13** and **14**.[89,90] Then reaction of **14** with Pd/$BaSO_4$ in H_2 forms the desired [6-^{13}C]-thymine **15** in 45% overall yield (Scheme 3).[89]

3.1.1.2. Purine Synthesis with C8 Specific Labeling. As with pyrimidines, purine nucleobases can be selectively labeled with ^{13}C and ^{15}N isotopes using commercially available precursor compounds. In the early 1990s, SantaLucia and Tinoco and co-workers described an effective purine synthesis using ^{13}C-formic acid to label purine C8.[71] More recently, Kreutz and co-workers streamlined and improved the efficiency of such labeling in one-step reactions.[75,85,91] Here, the condensation of ^{13}C-formic acid **16** with morpholine forms morpholinium formate intermediate that immediately reacts with either 4,5,6-triaminopyrimidine **17** to yield [8-^{13}C]-adenine **18** (Scheme 4) or 2,5,6-triaminopyrimidin-4-ol sulfate **19** to form [8-^{13}C]-guanine **20** (Scheme 5) with 64% and 94% yield, respectively.[75,85]

Scheme 4. Synthetic Route to [8-^{13}C]-Adenine[75,85]

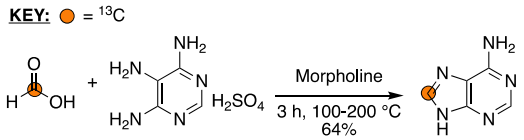

Scheme 5. Synthetic Route to [8-^{13}C]-Guanine[75,85]

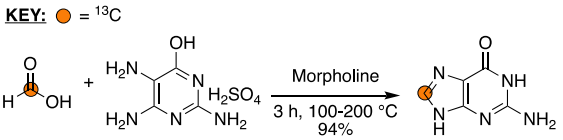

3.1.1.3. Purine Synthesis with C2 Specific Labeling. As with purine C8 labeling, adenine C2 can be readily labeled. Labeling C2 is attractive because its chemical shift can monitor protonation at adenine N1,[92] which cannot be achieved with ^{15}N NMR experiments due to severe line broadening.[92−94] Unlike the environments of single-stranded RNA, those in structured RNAs can shift the pK_a values of protonated adenosine or cytidines significantly toward neutrality, serving both catalytic and structural functions in RNA enzymes.[94−97]

https://doi.org/10.1021/acs.chemrev.1c00845
Chem. Rev. 2022, 122, 9357−9394

Scheme 6. Synthetic Route to [2-^{13}C]-Adenine[a]

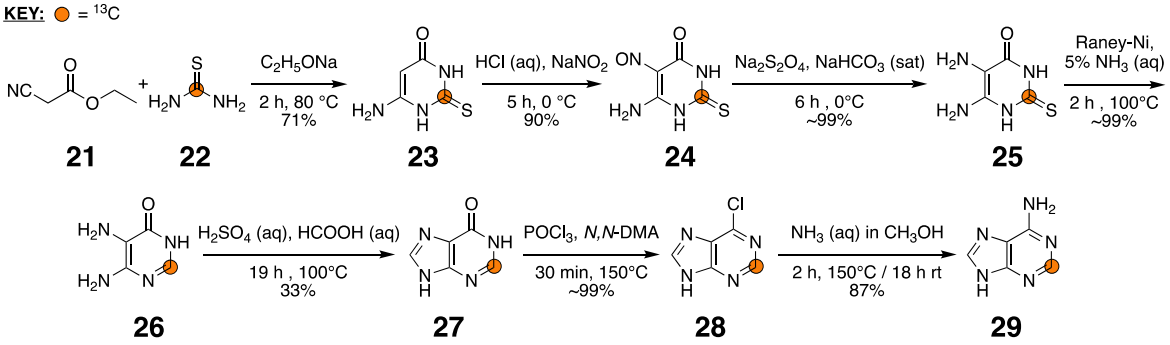

[a]Adapted with permission from Dayie and co-workers. Copyright 2020 Springer Nature.[104] Adenine can be labeled at N7 by using ^{15}N-labeled sodium nitrite in the second chemical step.

Scheme 7. Synthetic Route to [1-^{15}N]-Adenine[101]

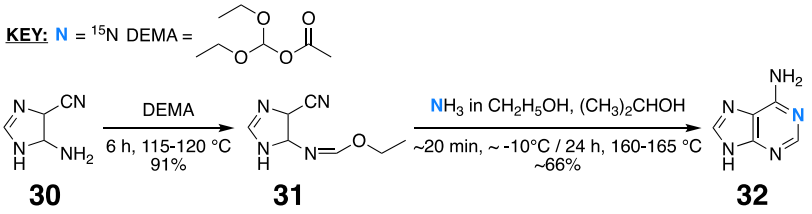

The ^{13}C isotope can be incorporated at the purine C2 site starting with 5-aminoimidazole-4-carboxamide (AICA) and ethylsodium ^{13}C-xanthate to form [2-^{13}C]-hypoxanthine, [2-^{13}C]-adenine, or [2-^{13}C]-guanine.[98]

A preferred alternative for purine C2 labeling uses the method of Battaglia and Ouwerkerk and co-workers, wherein sodium ethoxide (C_2H_5ONa) mediates cyclization of ethyl cyanoacetate **21** with ^{13}C-thiourea **22** to give [2-^{13}C]-6-amino-2-thiouracil **23**.[99,100] Unlabeled sodium nitrite ($NaNO_2$) is then used for nitrosylation (the ^{15}N-labeled form can also be used to introduce a second isotope label) to form **24**. Then sodium dithionite ($Na_2S_2O_4$) mediates the reduction of the nitroso group to yield **25** followed by desulfurization over Raney-Nickel to form the diaminopyrimidine **26**.[101] Treatment of the product with sulfuric (H_2SO_4) and formic (HCOOH) acids yields [2-^{13}C]-hypoxanthine **27**.[102] Subsequent reaction with phosphorus oxychloride ($POCl_3$) and *N*,*N*-dimethylaniline (*N*,*N*-DMA) yields [2-^{13}C]-6-chloropurine **28**.[103] In the final step, reaction with methanolic NH_3 in a microwave reactor yields the desired [2-^{13}C]-adenine **29** (Scheme 6).[100] Alternative purine synthesis pathways have been devised to enable specific labeling of adenine C2 or any purine nitrogen position.[98,100,102,104−108] We recently synthesized [7-^{15}N]-labeled **29** through intermediates **21**−**23** and ^{15}N-labeled intermediates **24**−**28** using the Battaglia-Ouwerkerk approach[99,100] and demonstrated its utility in NMR analysis of RNA structure and dynamics (Scheme 6).[104]

3.1.2. Specific ^{15}N Labeling. Several approaches have been reported for the synthesis of atom-specific ^{15}N-labeled nucleobases and nucleosides as well as their incorporation into the corresponding rNTPs and amidites for RNA synthesis.[98,100−102,104−114] Here, we highlight those methods that allow streamlined ^{15}N-labeled nucleobase synthesis in high yield. These labeling patterns permit direct monitoring of Watson−Crick base pairs or analysis of interconverting duplex, triplex, and quadruplex structures by multidimensional NMR.[110−113]

3.1.2.1. Pyrimidine N1, N3, and N4 Labeling. As described above, using the Poulter-SantaLucia-Kreutz approach,[71,74,81,82] ^{15}N-urea delivers ^{15}N at uracil N1 and N3 sites. Cytosine labeling, on the other hand, occurs through uracil, given that the corresponding CTP can be built directly from enzymatic conversion (with ammonium chloride, NH_4Cl) from UTP[74,115] or by chemical synthesis from a transiently protected uridine amidite.[85] In this way, all uracil isotope labeling patterns will be retained in CTP and cytidine amidites. Moreover, additional ^{15}N-labeling of the cytidine N4 amino group can be achieved using $^{15}NH_4Cl$ in the enzymatic[74] or chemical[85] reaction, as will be described in Sections 3.2 and 3.3.

3.1.2.2. Purine N1, N3, N7, and N9 Labeling. Synthesis of adenine N1 labeling occurs in two-steps.[101] Here, commercially available 5-aminoimidazole-4-carbonitrile **30** reacts with diethoxymethyl acetate (DEMA) to yield intermediate **31**. Subsequent reaction of **31** with aqueous ammonia (NH_3) readily forms the desired product [1-^{15}N]-adenine **32** with a total yield of 60% (Scheme 7)[101]

Adenine labeled at N3, on the other hand, can be synthesized in six steps.[108] In brief, commercially available 4-imidazolecarboxylic acid **33** is nitrated with ammonium nitrate ($NH_4{}^{15}NO_3$) to afford 5-[nitro-^{15}N]1H-imidazole-4-carboxylic acid **34**. Activation of **34** with 1,1′-carbonyldiimidazole (CDI) in dimethylformamide (DMF) and excess NH_3 forms carboxamide **35**. Importantly, addition of $^{15}NH_4Cl$ in this step can also introduce a ^{15}N label at the N1 site, permitting the eventual production of [1,3-$^{15}N_2$]-adenine.[108] Catalytic reduction of **35** affords [5-^{15}N]-AICA **36**. Ring closure of **36** with triethyl orthoformate ($HC(OC_2H_5)_3$) gives a hypoxanthine intermediate **37**, which readily forms [3-^{15}N]-6-chloropurine **38** upon chlorination with $POCl_3$ and *N*,*N*-DMA. Finally, ammonolysis with ammonium hydroxide (NH_4OH) yields the desired [3-^{15}N]-adenine **39** with ∼47% total yield (Scheme 8).[108]

https://doi.org/10.1021/acs.chemrev.1c00845
Chem. Rev. 2022, 122, 9357−9394

Scheme 8. Synthetic Route to [3-^{15}N]-Adenine[108a]

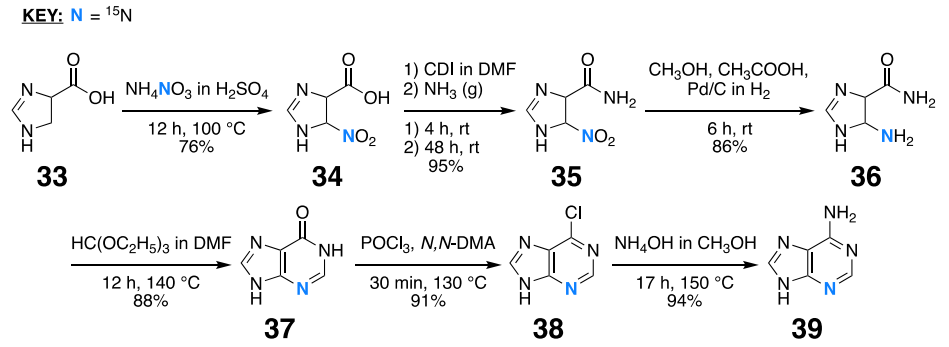

[a]Adenine N3 and its amino group can also be labeled at by $^{15}NH_4Cl$ and $^{15}NH_4OH$ in the second and final chemical steps, respectively.

Scheme 9. Synthetic Route to [7-^{15}N]-Guanine[a]

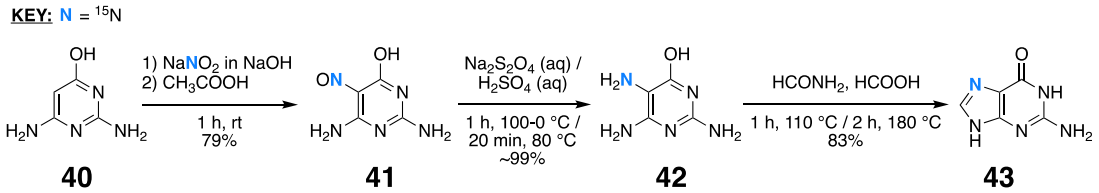

[a]Dayie and co-workers.[116]

Scheme 10. Synthetic Route to [7-^{15}N]-Adenine[a]

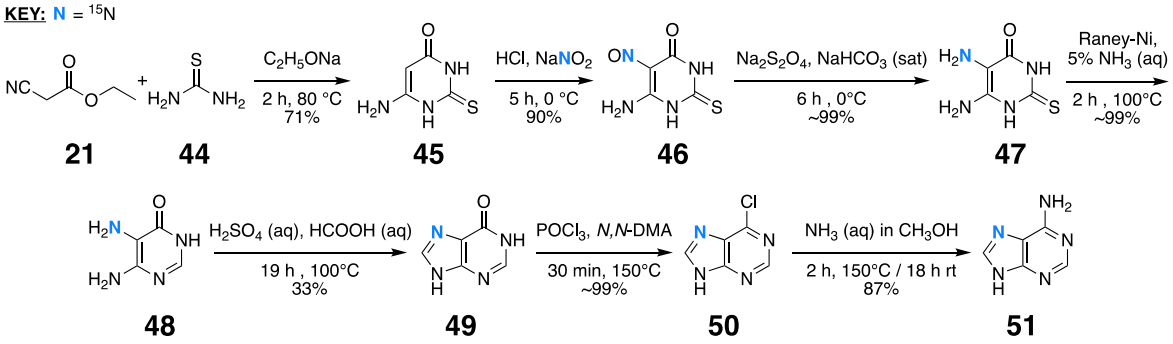

[a]Adapted with permission from Dayie and co-workers. Copyright 2020 Springer Nature.[104] Adenine C2 can also be labeled if ^{13}C-labeled thiourea is used as the starting material.

In addition, purine N7 labeling is readily achieved and has been widely adapted.[99,100,102,104,106,111] For example, synthesis of [7-^{15}N]-guanine is achieved in three-steps. Nitrosylation of commercially available 2,6-diaminopyrimidin-4-ol **40** by $Na^{15}NO_2$ yields 2,6-diamino-5-[nitroso-^{15}N]pyrimidin-4-ol **41**. Reduction of **41** with sodium dithionite followed by acidification by H_2SO_4 forms 2,6-diamino-5-[amino-^{15}N]-pyrimidin-4-ol **42**. In the final step, reflux with formamide ($HCONH_2$) followed by HCOOH provides the desired [7-^{15}N]-guanine **43** with a total yield of 65%[116] (Scheme 9).

Several direct routes to ^{15}N-labeled adenine initiate from commercially available aminopyrimidines.[102,106] However, Micura and Kreutz and co-workers[111] employed a sodium ethoxide mediated cyclization of **21** with **44** to form 6-amino-2-thiouracil **45**.[117] Subsequent nitrosylation of **45** installs the ^{15}N label using $Na^{15}NO_2$ to yield the nitroso-containing **46**.[102] A sodium dithionite mediated reduction of the nitroso group forms **47** and desulfurization over Raney-Nickel affords **48**.[102] Subsequent treatment with H_2SO_4 and HCOOH yields hypoxanthine **49**,[102] which was then reacted with $POCl_3$ and *N,N*-DMA to give [7-^{15}N]-6-chloropurine **50**.[103] In the final step, reaction with methanolic NH_3 in a microwave reactor gives the desired [7-^{15}N]-adenine **51** with a total yield of 18% (Scheme 10).[100,104,106,111] As mentioned above, we recently showcased the same synthetic scheme while also incorporating selective ^{13}C2 labeling.[104]

Finally, in the synthesis of N9-labeled adenine, 5-amino-4,6-dichloropyrimidine **52** is converted to a [9-^{15}N]-6-chloropurine **53** using aqueous $^{15}NH_3$ and DEMA.[118] Then a reaction with aqueous NH_3 yields the desired [9-^{15}N]-adenine **54**. This simple three-step reaction proceeds with an overall yield of 79% (Scheme 11).[118]

3.1.3. Nucleobase Labels: Summary and Outlook. As described in Sections 3.1.1 and 3.1.2, and shown in Schemes 1−11, a wide range of isotope-labeled nucleobases (Table 2) are now available to the scientific community. Of all synthetic procedures, purine C8 sites are most readily labeled in one chemical step in a single day and with high yield (64−94%) (Table 2). Conversely, adenine N3 is the least readily labeled, taking 11 days (Figure 2). Adenine C2 and N7 have the lowest

https://doi.org/10.1021/acs.chemrev.1c00845
Chem. Rev. 2022, 122, 9357−9394

Scheme 11. Synthetic Route to [9-^{15}N]-Adenine[118]

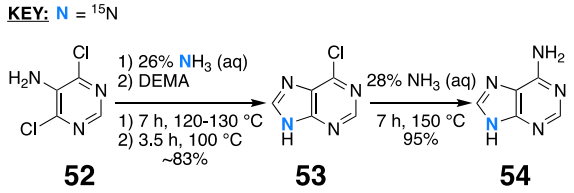

Table 2. Summary of All Nucleobase Labels As Outlined in Schemes 1−11

nucleobase label	time (days)[a]	chemical steps[b]	yield (%)	ref
[8-^{13}C]-adenine	1	1	64	75, 85
[8-^{13}C]-guanine	1	1	94	75, 85
[2-^{13}C]-adenine[c]	2.5	7 (1)	18	104
[1-^{15}N]-adenine	2.5	2 (1)	60	101
[3-^{15}N]-adenine	11	6 (2)	47	108
[7-^{15}N]-adenine[c]	2.5	7 (1)	18	104
[7-^{15}N]-guanine[d]	1.5	3	65	
[9-^{15}N]-adenine	5.5	3 (3)	79	118
[6-^{13}C, 5-^{2}H]-uracil	7	4	63	82, 85
[5-^{13}C, 5-^{19}F, 6-^{2}H]-uracil	8	5	38	18, 57, 82, 85, 86
[6-^{13}C]-thymine	2.5	3	45	89

[a]Total reaction time was based on the time required for all chemical steps. In addition, 16 h were added for any explicit mention of overnight procedures, and 24 h were added for any chromatographic purifications. [b]Number in parentheses represents the number of chromatographic purification steps. [c]All data for [2-^{13}C]-adenine and [7-^{15}N]-adenine labeling came from the same doubly labeled [2-^{13}C, 7-^{15}N]-adenine labeling scheme.[104] [d]This synthetic procedure is from Dayie and co-workers.[116]

overall yields of 18% (Table 2). In future work, it would be advantageous to focus on improving yields and reducing the number of chemical steps. Nevertheless, these RNA labeling patterns are commonly chosen based on the experimental information required and less often dictated by the relative time and yield of the building blocks.

3.2. Chemo-enzymatic Labeling

With chemically synthesized isotope-labeled nucleobases in-hand, this section outlines the various enzymatic methods that can be used to build them into isotope-labeled rNTPs (and dNTPs). Alternatively, this can be accomplished using *Escherichia coli*[45,119−121] or *Methylophilus methylotrophus*[44] grown on ^{13}C- or ^{15}N-enriched media, as reviewed elsewhere.[62,66]

3.2.1. Enzymatic Coupling of Nucleobase and Ribose Sources. The first enzymatic approach to prepare isotope-labeled rNTPs was the Gilles-Schramm-Williamson pentose phosphate pathway method,[65,122−125] which uses isotope-labeled D-glucoses as the precursor and requires 14 enzymes (Table 3) and several coenzymes. This method is appealing for uniform ribose labeling using commercially available uniformly ^{13}C- or ^{2}H-labeled D-glucoses.

In brief, hexokinase (HXK) (EC 2.7.1.1) phosphorylates ^{13}C-labeled D-glucose **55** at its O6 position to yield glucose-6-phosphate **56**. Then glucose-6-phosphate dehydrogenase (ZWF) (EC 1.1.1.49) oxidizes **56** to 6-phosphogluconate **57**, and phosphogluconate dehydrogenase (GND) (EC 1.1.1.44) further oxides **57** to **58**. Finally, ribose-5-phosphate isomerase (RPI1) (EC 5.3.1.6) isomerizes **58** to ribose-5-phosphate **59**. Following isomerization, phosphoribosylpyrophosphate synthetase (PRPPS) (EC 2.7.6.1) pyrophosphorylates **59** at its O1′ site to yield **60**. Then, adenine (APRT) (EC 2.4.2.7), guanine (XGPRT) (EC 2.4.2.22), or uridine (UPRT) (2.4.2.9) phosphoribosyl transferases facilitate the nucleophilic attack of the adenine or guanine N9 or uracil N1 to the C1′ of **60** to yield 5′-monophosphates **61−63**, respectively. Adenylate (MK) (EC 2.7.4.3), guanylate (GK) (EC 2.7.4.8), or nucleoside monophosphate (NMPK) (EC 2.7.4.4) kinases phosphorylate **61−63** to form the 5′-diphosphates **64−66**, respectively. Pyruvate kinase (PYKF) (EC 2.7.1.40) then catalyzes the final phosphorylation to form the 5′-triphosphates **67−69** (Scheme 12).[65,122−125] Finally, UTP **69** can be converted to CTP **70** by CTP synthase (CTPS) (EC 6.3.4.2) (Scheme 12).[65,122−125] Importantly, ^{15}N-labeling of the cytidine amino group can be achieved by using $^{15}NH_3$ in the final step (Scheme 12).[65,122−125]

Moreover, Williamson and Hennig and co-workers demonstrated that the Gilles-Schramm-Williamson method[65,122−125] is compatible with ^{19}F-labeled nucleobases[58,126,127] by synthesizing [2-^{19}F]-ATP,[127] [5-^{19}F]-UTP,[126] and [5-^{19}F]-CTP.[126] However, D-ribose is a more cost-effective labeled precursor than D-glucose for the selective ^{13}C- or ^{2}H-ribose labeling of rNTPs.[128]

On the basis of earlier work by Whitesides and co-workers,[131−133] our group truncated the relatively complex Gilles-Schramm-Williamson method[65,122−125] to use 10 enzymes instead of 18, and two cofactor regeneration systems (dATP and creatine phosphate) (Table 3). This chemo-enzymatic labeling[74,75,129] is a versatile technology to couple nucleobase to ribose followed by subsequent phosphorylation to the rNTP in a one-pot enzymatic reaction.[74,75,129] The nucleobase and ribose building blocks can be unlabeled, isotope-labeled, chemically synthesized, or commercially available. This method therefore permits a diverse set of labeling patterns. Moreover, this approach has many advantages over previously reported *de novo*[72,73] or chemical[134−138] synthesis methods including fewer enzymes, fewer synthetic steps, and greater yields. This method affords the facile coupling of chemically synthesized uniformly ^{15}N- and ^{13}C/^{15}N-labeled uracil (Scheme 1)[82,85] to commercially available unlabeled D-ribose and ^{13}C-labeled D-ribose. The resulting uniformly ^{15}N-labeled and uniformly ^{13}C/^{15}N-labeled UTP provided 338- and 14-fold savings over the commercially available material from CIL, respectively. However, the main advantage of chemo-enzymatic synthesis is the ability to generate noncommercially available atom-specific labeling patterns.

We showcased the power of this method with the synthesis of [1′,5′,6-$^{13}C_3$, 1,3-$^{15}N_2$]-pyrimidine rNTPs using six enzymes (Table 3).[74] We also used this method to synthesize [1′,8-$^{13}C_2$]-, or [2′,8-$^{13}C_2$]-, or [1′,5′,8-$^{13}C_3$]-ATPs and -GTPs with five enzymes (Table 3).[75] First, ^{13}C-labeled D-ribose **71** was phosphorylated at its O5 position by ribokinase (RK) (EC 2.7.1.15) to yield ribose-5-phosphate **72** followed by pyrophosphorylation at the O1 site by PRPPS to afford **73**. Then APRT, XGPRT, or UPRT catalyzed the nucleophilic attack of the adenine or guanine N9 or uracil N1 to the C1′ of **73** to yield 5′-monophosphates **74−76**, respectively. Phosphorylation of **74−76** is achieved by MK, GK, or UMP kinase (UMPK) (EC 2.7.4.22) to form the 5′-diphosphates **77−79**, respectively. Creatine kinase (CK) (EC 2.7.3.2) then facilitates

https://doi.org/10.1021/acs.chemrev.1c00845
Chem. Rev. 2022, 122, 9357−9394

Table 3. Enzymes of Glycolysis, Pentose Phosphate, and Nucleotide Biosynthesis and Salvage Pathway for rNTP Synthesis

enzyme[a]	abbreviation	EC number	source
Gilles-Schramm-Williamson and Co-workers[65,122−125]			
Hexokinase	HXK	2.7.1.1	Baker's yeast
Glucose-6-phosphate isomerase	PGI1	5.3.1.9	Baker's yeast
Glucose-6-phosphate dehydrogenase	ZWF	1.1.1.49	*L. mesenteroides*
Phosphogluconate dehydrogenase	GND	1.1.1.44	*Torula* yeast
Ribose-5-phosphate isomerase	RPI1	5.3.1.6	Spinach
Phosphoribosylpyrophosphate synthetase	PRPPS	2.7.6.1	*E. coli*
Adenine phosphoribosyltransferase	APRT	2.4.2.7	JM109/pTTA6
Uracil phosphoribosyltransferase	UPRT	2.4.2.9	JM109/pTTU2
Xanthine-guanine phosphoribosyltransferase	XGPRT	2.4.2.22	JM109/pTTG2
Nucleoside-monophosphate kinase	NMPK	2.7.4.4	Bovine liver
Myokinase (Adenylate kinase)	MK	2.7.4.3	Rabbit muscle
Guanylate kinase	GK	2.7.4.8	Porcine brain
3-Phosphoglycerate mutase	YIBO	5.4.2.1	Rabbit muscle
Enolase	ENO	4.2.1.11	Baker's yeast
Pyruvate kinase	PYKF	2.7.1.40	Rabbit muscle
Glutamate dehydrogenase (NAD(P)+)	GLUD	1.4.1.3	Bovine liver
CTP synthase	CTPS	6.3.4.2	JM109/pMW5
L-Lactate dehydrogenase	LDH	1.1.1.27	Rabbit muscle
Dayie and Co-workers[74,75,129]			
Ribokinase	RK	2.7.1.15	*E. coli*
Creatine kinase	CK	2.7.3.2	Chicken muscle
UMP kinase	UMPK	2.7.4.22	*E. coli*
Serianni and Co-workers[130]			
Purine nucleoside phosphorylase	PNPase	2.4.2.1	*E. coli*
Xanthine oxidase	XO	1.1.3.22	Buttermilk
Catalase	CT	1.11.1.6	Bovine liver
Uridine phosphorylase	UPase	2.4.2.3	*E. coli*

[a]Given that there is overlap in the enzymes used in the methods of Schramm-Williamson and co-workers[65,122−125] and Dayie and co-workers,[74,75,129] only the unique enzymes are listed for the latter. All enzymes are commercially available except APRT, UPRT, XGPRT, CTPS, and RK.[129] These are currently only available in a few academic laboratories. At some point, these plasmids would be available at Addgene.

the final phosphorylation to afford the 5′-triphosphates **80**−**82** (Scheme 13).[74,75,129] Similar to the Gilles-Schramm-Williamson method,[65,122−125] a final ^{15}N label can be introduced at the CTP **83** amino group if $^{15}NH_4Cl$ is used alongside CTPS in the final enzymatic step (Scheme 13).[74,75,129] These atom-specifically labeled rNTPs can then be used with *in vitro* transcription to make RNAs without any size limit. Importantly, these labeling patterns reduced spectral crowding, increased signal-to-noise ratios, facilitated direct carbon detection experiments, and eliminated $^{13}C-^{13}C$ scalar and dipolar couplings.[63,74,75,86,104]

As with the Gilles-Schramm-Williamson method,[65,122−125] the approach developed by Dayie and co-workers[74,75,129] is also compatible with ^{19}F-labeled nucleobases (e.g., [2-^{19}F]-adenine and [5-^{19}F]-uracil[18,86]). It is worth noting that Serianni and co-workers have also developed a complementary approach to enzymatically couple nucleobase and ribose sources using four enzymes (Table 3).[130] Their method uses hypoxanthine **84** and 1-*O*-acetyl-2,3,5-tri-*O*-benzoyl-α-D-ribofuranoside (ATBR) **85** in a Vorbrüggen reaction (detailed in Scheme 15) to yield inosine **86**. Then purine nucleoside phosphorylase (PNPase) (EC 2.4.2.1) replaces the hypoxanthine moiety on the C1 position of **86** with a phosphate group to give α-D-ribofuranosyl-1-phosphate sodium salt (αR1P) **87** (Table 3).[130] Then **87** is glycosylated by PNPase with adenine or guanine or by UPase (EC 2.4.3.2) with uracil to form nucleosides **88**−**90**, respectively (Scheme 14).[130] Products **88**−**90** can then be converted to the desired rNTP or amidite with further enzymatic or chemical synthesis.

3.2.2. Enzymatic Methods for Position-Specific Labeling. While these chemo-enzymatic methods enable straightforward atom-specific labeling, they rely solely on DNA template-directed T7 RNA polymerase-based *in vitro* transcription and are therefore unable to incorporate these labels position-specifically (e.g., nucleotide 5). Fortunately, there are two alternative enzymatic methods capable of such position-specific labeling, both of which are compatible with the isotope-labeled rNTP building blocks described above. Wang and co-workers developed a hybrid solid−liquid phase transcription technique that employs an automated robotic platform known as position-selective labeling of RNA (PLOR).[139] In PLOR, the DNA template is attached to beads and RNA synthesis is initiated by the addition of T7 RNA polymerase and a mixture of three of the four rNTP building blocks (e.g., ATP, GTP, and CTP). The beads are then washed and a new rNTP mixture is added, this time containing the previously omitted building block. Thus, PLOR can incorporate any isotope-labeled rNTP (e.g., [6-^{13}C, 5-^{2}H]-UTP) position-specifically, assuming the desired labeling site (e.g., uridine 10) does not coincide with a stretch of identical nucleotides (e.g., UUU). While isotope labeling by PLOR has aided NMR studies of RNA,[139−141] its widespread use is still limited due to the requisite equipment needed and its laborious nature.

Schwalbe and co-workers developed an alternative chemo-enzymatic approach for position-specific labeling.[142] Impor-

https://doi.org/10.1021/acs.chemrev.1c00845
Chem. Rev. 2022, 122, 9357−9394

Scheme 12. Enzymatic Synthesis of Isotope-Labeled rNTPs from D-Glucose Sources[65,122−125]

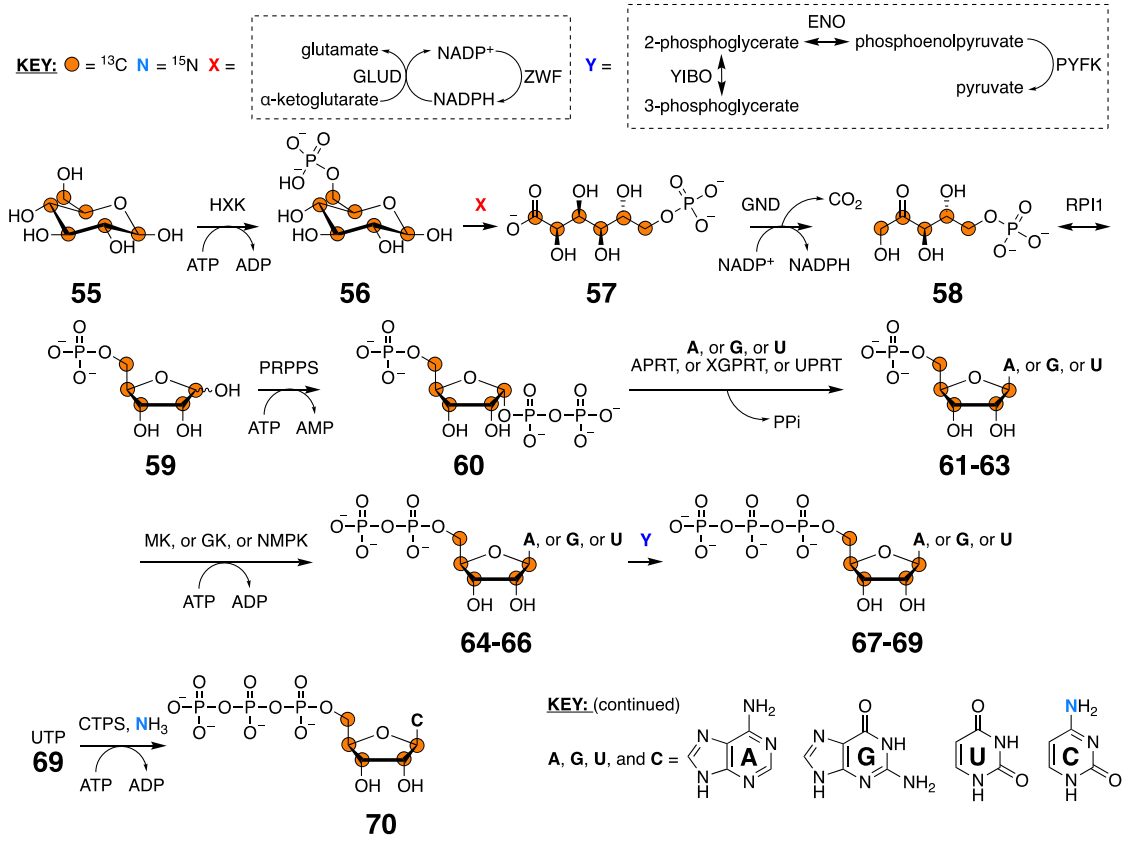

Scheme 13. Enzymatic Synthesis of Isotope-Labeled rNTPs from D-Ribose Sources[74,75,129]

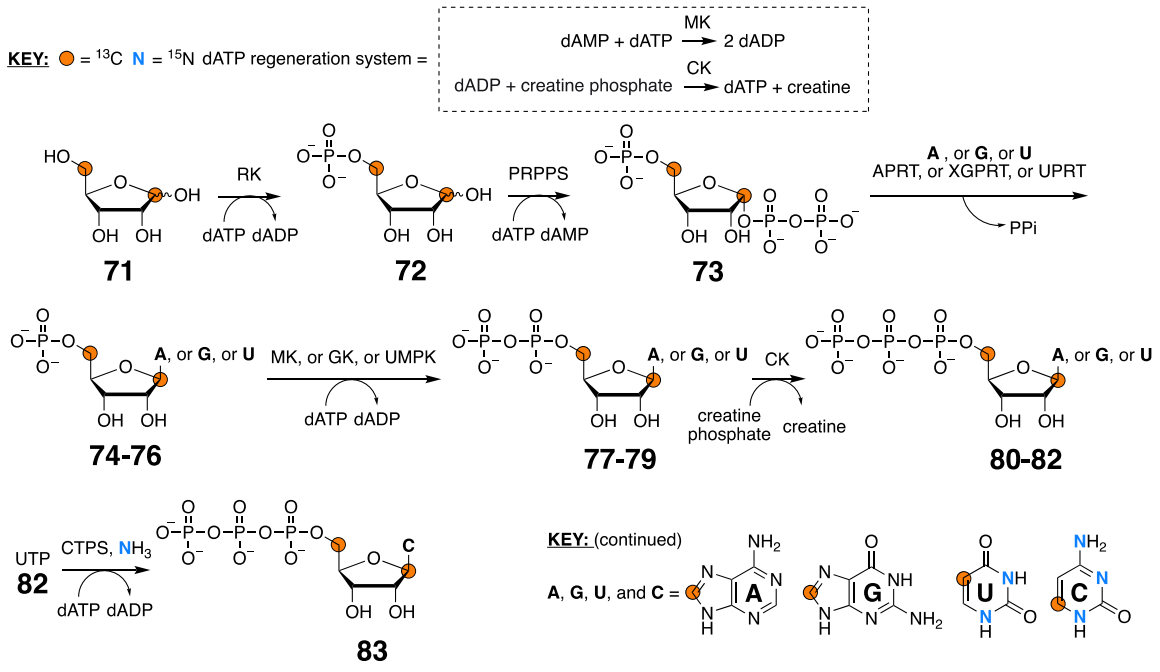

tantly, this method uses standard laboratory equipment and commercially available enzymes T4 RNA ligase 1 (EC 6.5.1.3), recombinant shrimp alkaline phosphatase (rSAP) (EC 3.1.3.1), and T4 RNA ligase 2 (EC 6.5.1.3), making it more accessible than PLOR. In their method, a modified nucleoside 3′,5′-biphosphate is incorporated at the 3′-end of an RNA fragment by T4 RNA ligase 1 followed by dephosphorylation by rSAP and DNA-splinted ligation by T4 RNA ligase 2. This technique has been used to introduce modified nucleosides (i.e., photocaged, photoswitchable, and isotope-labeled) into RNAs up to 392 nts. While this method holds great promise for NMR applications, low yields of bis-phosphorylation (6−

https://doi.org/10.1021/acs.chemrev.1c00845
Chem. Rev. 2022, 122, 9357−9394

Scheme 14. Enzymatic Synthesis of Isotope-Labeled Nucleosides from Inosine[130]

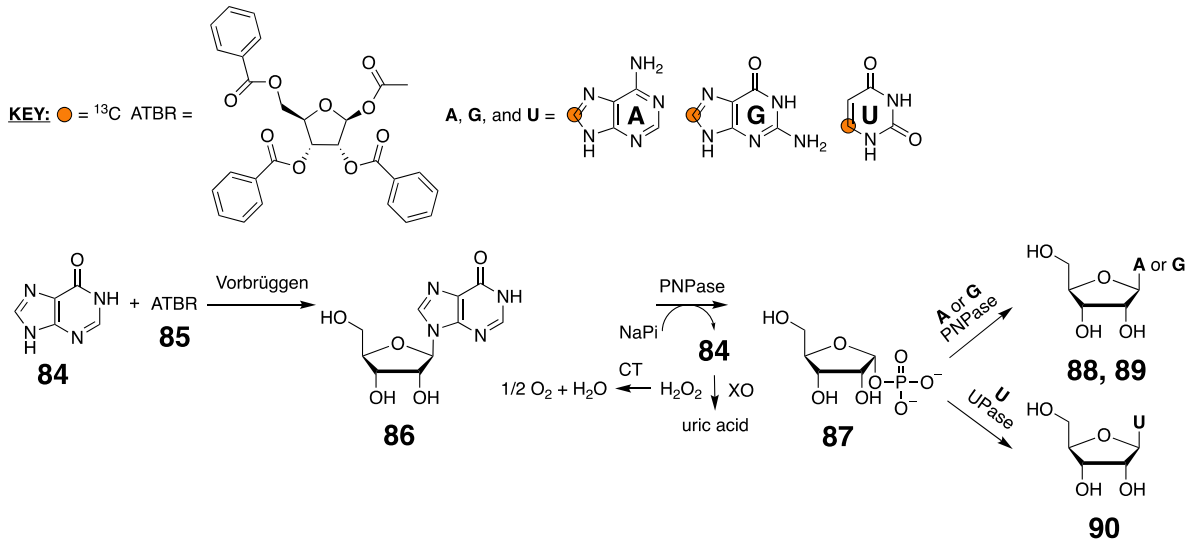

22%) and ligation (9−49%) reactions are a major drawback.[142] More recent efforts by Schwalbe and co-workers to improve this technology include the addition of magnetic streptavidin beads as a solid-support and 5′-biotinylated RNA.[143]

3.2.3. rNTP Labels: Summary and Outlook. As described in Section 3.2.1 and shown in Scheme 13, the chemo-enzymatic labeling method developed by Dayie and co-workers[74,75,129] permits the synthesis of a versatile assortment of rNTPs with atom-specific isotope labels (Table 4). While there are other enzymatic methods to generate both atom-specific (e.g., the Gilles-Schramm-Williamson[65,122−125] or Serriani[130] methods shown in Schemes 12 and 14, respectively) and position-specific (e.g., PLOR[139] and the Schwalbe method[142,143]) labels, no other technique offers the versatility and simplicity that is afforded by the Dayie method. Our one-pot chemo-enzymatic approach can produce isotope-labeled purine and pyrimidine rNTPs in a few days and with high yield (75−95%) (Table 4). The main disadvantage of this method is the need to express and purify five noncommercial enzymes in-house (Table 3). However, providing these plasmids to Addgene will make our method widely accessible to the field.

Table 4. Summary of rNTP Labels Made from Chemo-enzymatic Synthesis[74,75,129]

rNTP label[a]	time (days)[b]	enzymatic steps[c]	yield (%)	ref
[8-^{13}C]-ATP	1.5	1 (1)	90	75
[8-^{13}C]-GTP	1.5	1 (1)	75	75
[1′,5′,6-$^{13}C_3$, 1,3-$^{15}N_2$]-CTP	3	3 (2)	95	74
[1′,5′,6-$^{13}C_3$, 1,3-$^{15}N_2$]-UTP	2.5	2 (2)	90	74

[a][8-^{13}C]-adenine and -guanine were coupled to [1-^{13}C]-, or [2-^{13}C]-, or [1,5-$^{13}C_2$]-D-ribose to generate a variety of ATPs and GTPs.[75] The [6-^{13}C, 1,3-$^{15}N_2$]-uracil and -cytosine nucleobases, on the other hand, were coupled to [1′,5′-$^{13}C_2$]-D-ribose only.[74] Nevertheless, the reported times, enzymatic steps, and yields are representative of all ATP, GTP, CTP, and UTP reactions made with this method. [b]Total reaction time was based on the time required for all chemical steps. In addition, 24 h were added for any chromatographic purification. [c]Number in parentheses represents the number of chromatographic purification steps. Since the time of our original publication,[74] pyrimidine rNTP synthesis now only requires one chromatographic purification.[18,86]

3.3. Synthesis of Labeled RNA Phosphoramidites

While the enzymatic production of RNA with isotope-labeled rNTPs[44,45,69−75] is the most widely used approach to obtain labeled RNA, an attractive alternative is to use isotope-labeled amidites and solid-phase synthesis. Like PLOR introduced by Wang and co-workers[139] and the chemo-enzymatic approach developed by Schwalbe and co-workers,[142,143] the amidite method offers the advantage of position-specific RNA labeling. However, even though amidite labeling is currently the most effective and widely used method for position-specific labeling, its utility for NMR studies is limited to RNAs ≈ 60 nt.

3.3.1. ^{15}N and ^{13}C Labeling. The Kreutz and Micura groups have used isotope-labeled nucleobases to prepare 2′-*O*-*tert*-butyldimethylsilyl (*t*BDMS) and 2′-*O*-[(triisopropylsilyl)-oxy]methyl (TOM) phosphoramidites for NMR studies,[57,82,85,89,110,111,144,145] as recently reviewed.[61] A representative example of [6-^{13}C, 5-^{2}H]-pyrimidine 2′-*O*-TOM amidite syntheses is shown in Schemes 15 and 16.[85] In brief, [6-^{13}C, 5-^{2}H]-uracil **5** is coupled to ATBR under Vorbrüggen conditions[138] to give the 2′,3′,5′-O-benzoyl (Bz)-protected **91**, which is then fully deprotected to nucleoside **92** after treatment with methylamine (CH_3NH_2) in ethanol (C_2H_5OH). Addition of 4,4′-dimethoxytrityl chloride (DMT-Cl) and TOM-Cl protects the 5′- and 2′-hydroxyl (OH) to form **93** and **94**, respectively. Finally, phosphitylation of the 3′-OH of **94** with 2-cyanoethyl *N*,*N*-diisopropyl-chlorophosphoramidite (CEP-Cl) and *N*,*N*-diisopropyl-ethylamine (DiPEA) yields the desired [6-^{13}C, 5-^{2}H]-uridine 2′-*O*-TOM amidite **95** with five-steps in 22% total yield (Scheme 15).[85]

The corresponding cytidine derivative is obtained from **94** in four additional steps (Scheme 16).[85] First, the 3′-OH of **94** is transiently acetylated with Ac_2O to afford **96**. Then treatment with 2,4,6-triisopropylbenzenesulfonyl chloride (TiBSC) and TEA yields the 5′-*O*-DMT-2′-*O*-TOM cytidine **97**, which is immediately N^4-acetylated (Ac) with Ac_2O to form **98**. Finally, 3′-OH phosphitylation yields the desired [6-^{13}C, 5-^{2}H]-N^4−

https://doi.org/10.1021/acs.chemrev.1c00845
Chem. Rev. 2022, 122, 9357−9394

Scheme 15. Synthetic Route to [6-^{13}C, 5-^{2}H]-Uridine 2′-*O*-TOM Amidite[85]

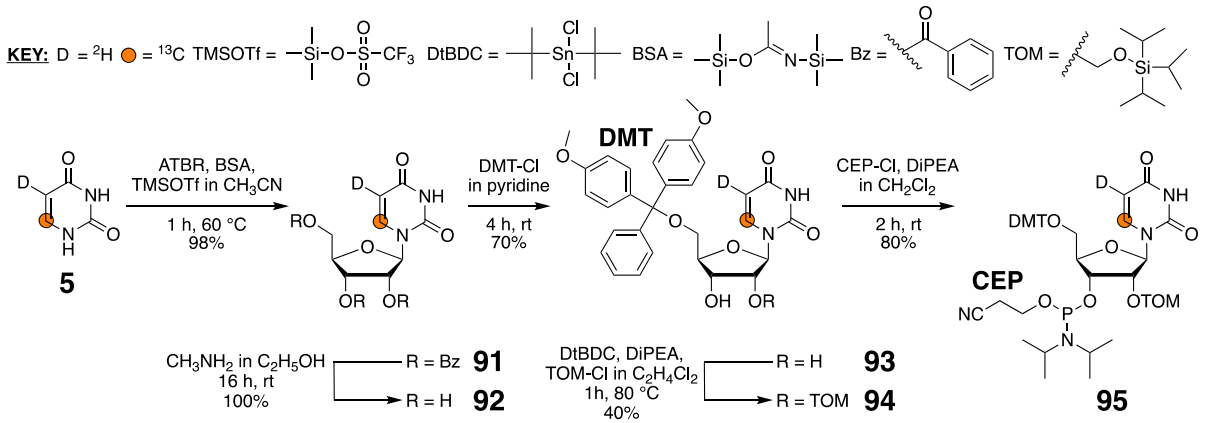

Scheme 16. Synthetic Route to [6-^{13}C, 5-^{2}H]-N^{4}–Ac-Cytidine 2′-*O*-TOM Amidite[85]

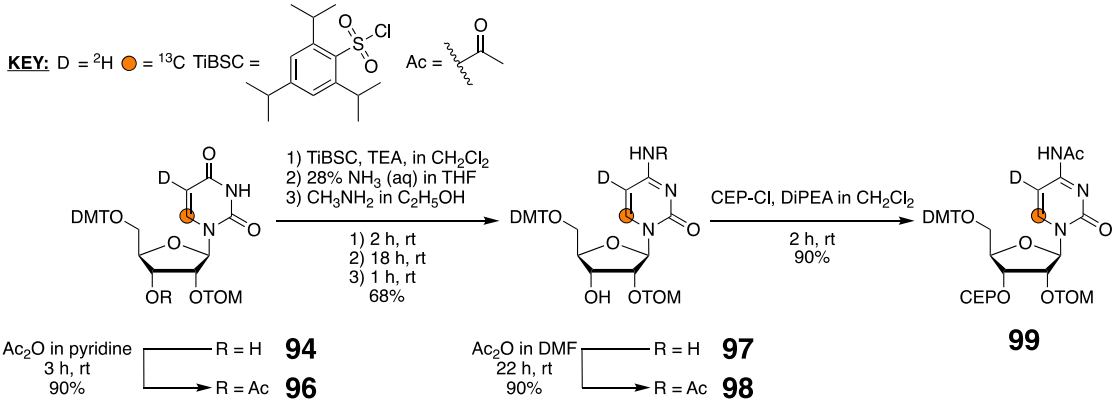

Scheme 17. Synthetic Route to [8-^{13}C]-N^{6}-Bz-Adenosine 2′-*O*-TOM Amidite[85]

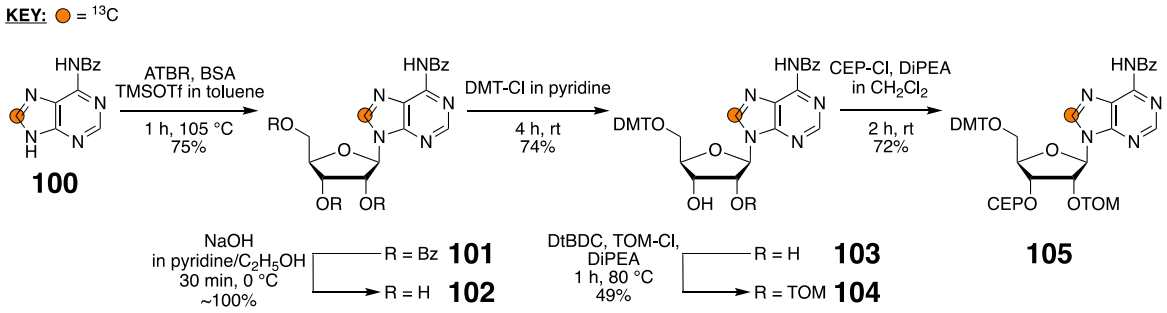

Scheme 18. Synthetic Route to [8-^{13}C]-N^{2}-iBu-Guanosine 2′-*O*-TOM Amidite[85]

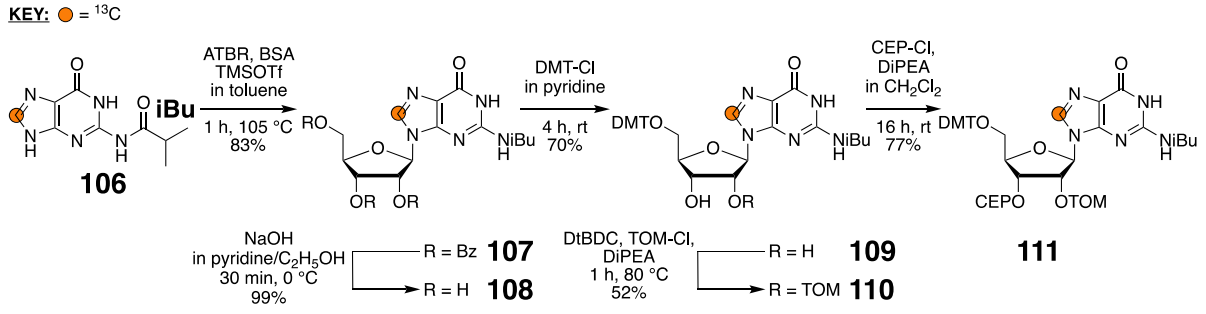

Ac-cytidine 2′-*O*-TOM amidite **99**. Starting from uracil **5**, this cytidine synthesis has an overall yield of 14% (Scheme 16).[85]

In contrast to pyrimidines, the starting purine is protected before beginning the nucleosidation reaction. Representative examples of [8-^{13}C]-purine 2′-O-TOM amidite syntheses are

https://doi.org/10.1021/acs.chemrev.1c00845
Chem. Rev. 2022, 122, 9357−9394

Scheme 19. Synthetic Route to [1,3-$^{15}N_2$]-cmo^5-Uridine 2′-*O*-*t*BDMS Amidite[149]

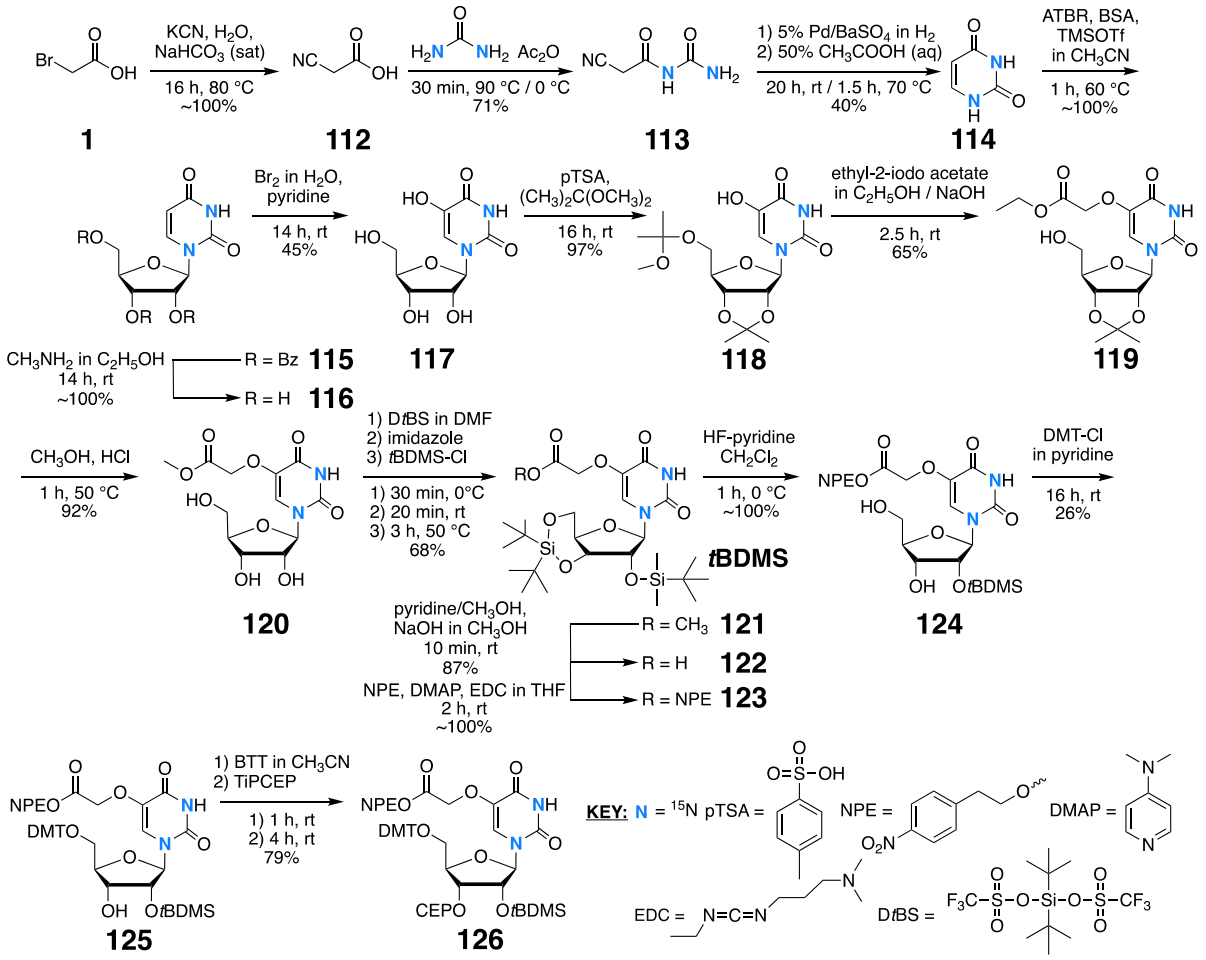

shown in Schemes 17 and 18.[85] Starting with [8-^{13}C]-adenine **18**, N^6-Bz-protected adenine **100** is formed with a yield of 86%. A subsequent Vorbrüggen reaction[138] gives the 2′,3′,5′-O-Bz-protected **101**, which is readily 2′,3′,5′-*O*-deprotected to nucleoside **102** after treatment with sodium hydroxide (NaOH) in pyridine and C_2H_5OH. Then, 5′-OH tritylation, 2′-OH TOM protection, and 3′-OH phosphitylation yields **103**, **104**, and **105**, respectively. Taken together, [8-^{13}C]-N^6-Bz-adenosine 2′-*O*-TOM amidite **105** was synthesized with 17% total yield (Scheme 17).[85]

Guanosine synthesis, on the other hand, proceeds from a N^2-isobutyryl (iBu) protected guanine **106** made from [8-^{13}C]-guanine **20** with a yield of 77%. From there, however, synthesis proceed as with adenine. That is, **106** is reacted under Vorbrüggen conditions[138] to form **107**, which is then 2′,3′,5′-*O*-deprotected to nucleoside **108**. Again, 5′-OH tritylation, 2′-OH TOM protection, and 3′-OH phosphitylation yields **109**, **110**, and **111**, respectively. In summary, [8-^{13}C]-N^2-iBu-guanosine 2′-*O*-TOM amidite **111** was synthesized with an overall yield of 18% (Scheme 18).[85] Importantly, Schemes 15−18 can be adapted to prepare 2′-*O*-*t*BDMS amidites simply by altering the 2′-OH protection reaction steps.

However, these 2′-*O*-*t*BDMS or 2′-*O*-TOM amidites are not suitable for producing RNAs > 60 nts. Instead, amidites with 2-cyanoethoxymethyl (CEM) as the 2′-OH protecting group[146,147] are used, due to its increased coupling efficiency, which rivals that in DNA synthesis.[80] Using a protocol developed by Yano and co-workers,[146,147] Kreutz and co-workers prepared [6-^{13}C, 5-^{2}H]-pyrimidine, [8-^{13}C]-purine, and the modified [1,3-$^{15}N_2$]-dihydrouridine and [2,8-$^{13}C_2$]-inosine 2′-*O*-CEM amidites.[91] While the benefits of the CEM amidite method are attractive for obvious reasons, it has not gained widespread use due to the commercial unavailability of both unlabeled and isotope-labeled CEM amidites.

3.3.2. ^{19}F Labeling and Post-transcriptional Modifications. Another benefit of labeling with amidites is the position-specific incorporation of modified building blocks. Indeed, many epigenetic and post-transcriptional modifications modulate the structure, dynamics, and folding of RNAs, and NMR is providing new insights into their functions.[148] These studies have been greatly aided by the synthesis of ^{13}C- or ^{15}N-labeled amidites bearing modifications such as uridine 5-oxyacetic acid (cmo^{5}U)[149] and N^6-methyladenine (m^{6}A).[150,151] In collaboration with the Al-Hashimi group, Kreutz and co-workers synthesized a ^{15}N-labeled cmo^{5}U amidite.[149] Their synthetic route begins from bromoacetic acid **1** and through intermediates **112** and **113** to assemble [1,3-$^{15}N_2$]-uracil **114**, as in Schemes 1[82,85] and 2.[18,57,82,86] Then **114** was coupled to ATBR under Vorbrüggen conditions, 2′,3′,5′-*O*-deprotected, and hydroxylated at the C5 position to yield **115**, **116**, and **117**, respectively. Addition of para-toluene sulfonic acid (pTSA) and dimethoxypropane ($(CH_3)_2C(OCH_3)_2$) then formed the 2′,3′,5′-*O*-protected nucleoside **118**. Reacting **118** with ethyl-2-iodo acetate in C_2H_5OH and NaOH transformed the 5-OH into an ethylcarboxymethoxy group while also deprotecting the 5′-

https://doi.org/10.1021/acs.chemrev.1c00845
Chem. Rev. 2022, 122, 9357−9394

Scheme 20. Synthetic Route to [2,8-$^{13}C_2$]-N^6-Methyladenosine 2′-*O*-*t*BDMS Amidite[150]

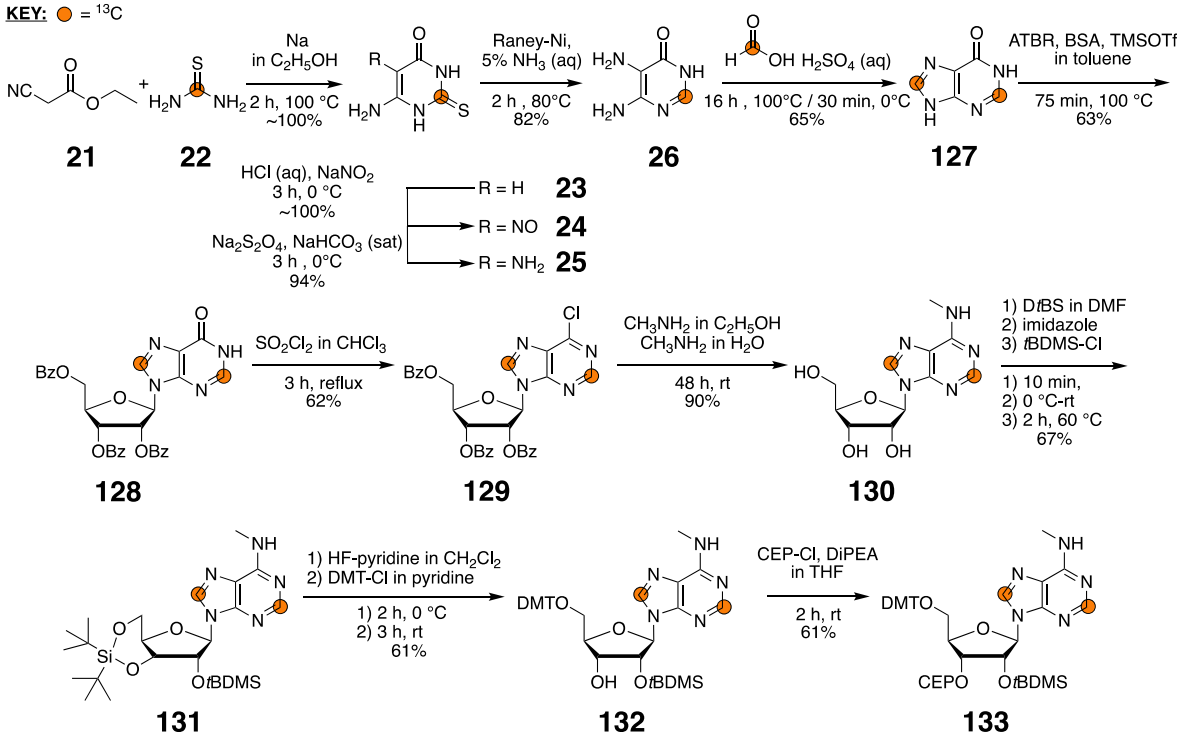

Scheme 21. Synthetic Route to [5-^{13}C, 5-^{19}F]-Uridine 2′-*O*-*t*BDMS Amidite[57]

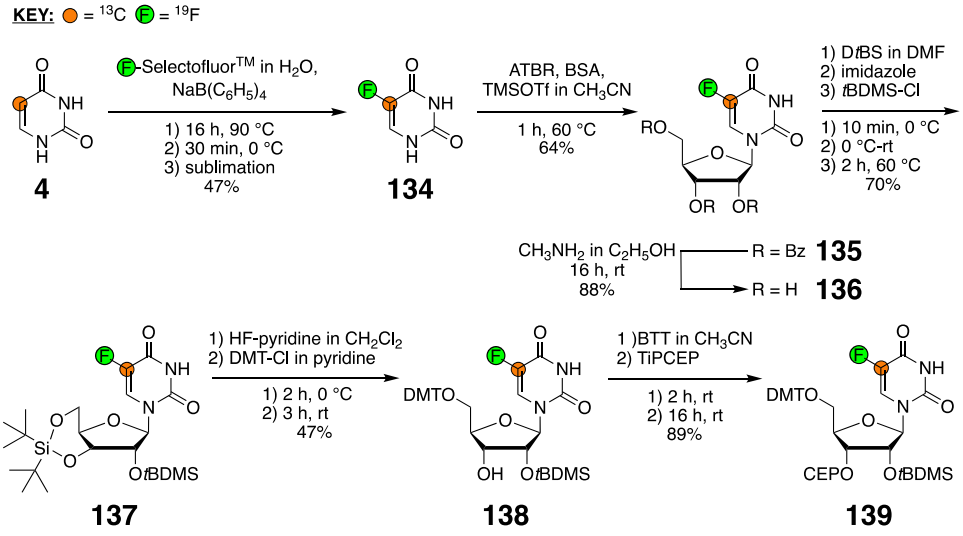

OH to afford **119**. After transient 2′,3′-*O*-deprotection of **119** to form **120**, the 3′- and 5′-OH were immediately protected along with 2′-*O*-*t*BDMS protection to yield **121** by adding di-*tert*-butylsilyl bis(trifluoromethanesulfonate) (D*t*BS) and *t*BDMS-Cl. Addition of pyridine and CH_3OH to **121** forms **122**, and subsequent treatment with nitrophenyl ethanol (NPE), *N*-dimethyl aminopyridine (DMAP), and *N*-ethyl-*N*′-(3-dimethyl aminopropyl) carbodiimide (EDC) construct the NPE-protected cmo^5 group to yield **123**. Reaction of **123** with hydrogen fluoride (HF) affords the 3′,5′-*O*-deprotected **124**, which can then be 5′-*O*-tritylatyed to yield **125**. Finally, phosphitylation of the 3′-OH of **125** with 2-cyanoethyl N,N,N′,N′-tetraisopropylphosphorodiamidite (TiPCEP) yields **126** (Scheme 19).[149] Taken together, [1,3-$^{15}N_2$]-cmo^{5}U 2′-*O*-*t*BDMS amidite **126** was synthesized with 15 steps in 1% total yield (Scheme 19).[149]

Another example from the Al-Hashimi and Kreutz groups showcases the synthesis of a ^{13}C-labeled m^{6}A amidite.[150] Their synthetic route begins with ethyl cyanoacetate **21** and ^{13}C-thiourea **22** and through intermediates **23**−**25** to assemble [2-^{13}C]-5,6-diamino-4-pyrimidinone **26**, as in Scheme 6.[104] In contrast to Scheme 6, however, H^{13}COOH was used with H_2SO4 to introduce a second ^{13}C label and form [2,8-$^{13}C_2$]-hypoxanthine **127**. Then the familiar Vorbrüggen reaction of **127** with ATBR yields the 2′,3′,5′-*O*-Bz-protected **128** followed by addition of sulfuryl chloride (SO_2Cl_2) to yield 6-chloropurine nucleoside **129**. Sequential addition of CH_3NH_2 in C_2H_5OH and then H_2O affords the m^{6}A nucleoside **130**. Again, the synthetic route ends with 2′-*O*-*t*BDMS protection,

https://doi.org/10.1021/acs.chemrev.1c00845
Chem. Rev. 2022, 122, 9357−9394

Scheme 22. Synthetic Route to [5-^{13}C, 5-^{19}F]-Cytidine 2′-*O*-*t*BDMS Amidite[57]

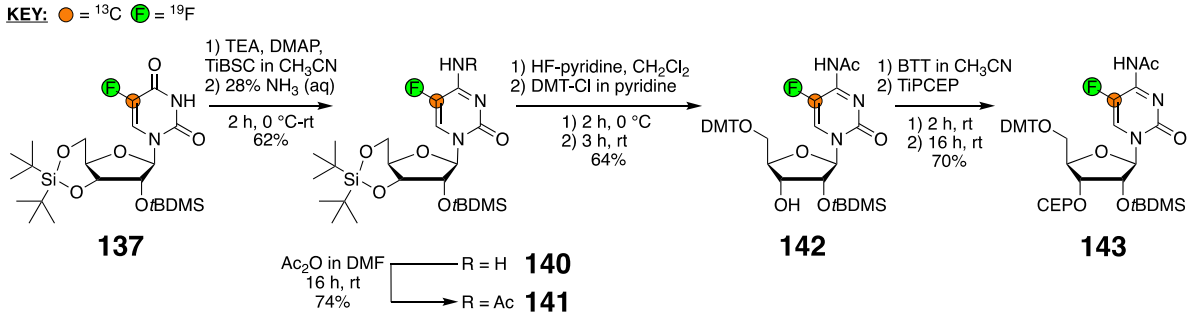

5′-*O*-tritylation, and 3′-*O*-phosphitylation to yield **131**, **132**, and **133**, respectively (Scheme 20).[150] In summary, [2,8-$^{13}C_2$]-N^6-methyladenosine 2′-*O*-*t*BDMS amidite **133** was synthesized in 11 steps with an overall yield of 4% (Scheme 20).[150]

Commercially, INNotope has ^{13}C-labeled N^1-methyladenine, m^{6}A, and N^3-methylcytidine 2′-*O*-*t*BDMS amidites available. Finally, [1,3-$^{15}N_2$]-pseudouridine (Ψ) amidites can be made from ^{15}N-labeled uracil with 11 steps in 6% total yield.[152]

Additionally, building on the work shown in Scheme 2,[18,57,82,85,86] Kreutz and co-workers showcased new methods to incorporate ^{19}F−^{13}C into the pyrimidine nucleobase of amidites.[18,57,86] Starting from [6-^{13}C]-uracil **4**, fluorination is achieved with Selectfluor to yield 5FU **134**, as in Scheme 2.[18,57,82,85,86] The remaining chemical steps are similar for other 2′-*O*-*t*BDMS amidite syntheses (Schemes 19[149] and 20[150]). That is, **134** is coupled to ATBR under Vorbrüggen conditions, 2′,3′,5′-*O*-deprotected, and then 3′,5′-*O*-protected and 2′-*O*-*t*BDMS protected to yield **135**, **136**, and **137**, respectively. Finally, **137** is 5′-*O*-tritylated, and 3′-*O*-phosphitylated to yield **138** and **139**, respectively (Scheme 21).[57] Taken together, [5-^{13}C, 5-^{19}F]-uridine 2′-*O*-*t*BDMS amidite **139** was synthesized with six-steps in 8% total yield (Scheme 21).[57] The corresponding cytidine derivative is obtained from **137** through intermediates **140**−**142** to afford the desired **143** (Scheme 22),[57] as in Scheme 16.[85] In summary, [5-^{13}C, 5-^{19}F]-N^4-Ac-cytidine 2′-*O*-*t*BDMS amidite **143** was synthesized in eight-steps with an overall yield of 4% (Scheme 22).[57] These labeling topologies not only capitalize on the beneficial spectroscopic properties of the ^{19}F nuclei (Section 2.4) but also open the door to NMR studies of large RNAs, as will be discussed in greater detail in Section 5.

3.3.3. Synergy between Phosphoramidites and Chemo-enzymatic Labeling. In principle, any nucleobase labeling scheme described in Section 3.1 can be coupled to any commercially available ^{13}C- or ^{2}H-labeled D-ribose (from Omicron Biochemicals or CIL) with the chemo-enzymatic method (Section 3.2) and built into an amidite with a variety of 2′-OH protecting groups (Section 3.3). Indeed, our group recently made [1′,8-$^{13}C_2$]-N^6-Bz-adenosine 2′-*O*-*t*BDMS[144] and [1′,6-$^{13}C_2$, 5-^{2}H]-uridine 2′-*O*-CEM[153] amidites via chemo-enzymatic synthesis, dephosphorylation with rSAP, and chemical synthesis. These amidites can then be used to make RNA via solid-phase synthesis. Given that the Kreutz and Micura groups have implemented a wide variety of atom-specific labeling schemes into the nucleobase of RNAs,[57,61,82,85,89,110,111,144,145] this hybrid approach is only needed if ribose labeling is desired in a position-specific manner. However, INNotope and Silantes have [1′,2,8-$^{13}C_3$]-N^6-Ac-adenosine, [1′,8-$^{13}C_2$]-adenosine, [1′,8-$^{13}C_2$]-N^2-Ac-guanosine, [1′,6-$^{13}C_2$, 5-^{2}H]-uridine, and [1′,6-$^{13}C_2$, 5-^{2}H]-N^4-Ac-cytidine 2′-*O*-*t*BDMS amidites available.

3.3.4. Phosphoramidite Labels: Summary and Outlook. As described in Sections 3.3.1 and 3.3.2, and shown in Schemes 15−22, again, a wide range of isotope-labeled amidites (Table 5) are becoming available to the scientific community. For all synthetic protocols, pyrimidine C6/C5 and purine C8 sites are most readily labeled. The production of these 2′-*O*-TOM amidites is streamlined[85] and proceeds quickly (∼1 week) and with adequate yields (14−18%) (Table 5). The introduction of ^{19}F labels and post-transcriptional modifications, on the other hand, dramatically increases the time of synthesis (i.e., up to 10 days) and reduces the overall reaction yields (i.e., as low as 1%) (Table 5). Nevertheless, the benefits afforded by the position-specific incorporation of these labels into RNA more than offsets these shortcomings. As with nucleobase labeling, researchers are typically motivated by the scientific question they are pursuing rather than the relative yields of each labeling reaction. Still, improvements in reaction yields and reduction in chemical steps would be advantageous for future work.

Table 5. Summary of All RNA Phosphoramidite Labels As Outlined in Schemes 15−22

RNA phosphoramidite label[a]	time (days)[b]	chemical steps[c]	yield (%)	ref
[8-^{13}C]-N^6-Bz-adenosine (TOM)	4.5	5 (4)	17	85
[2,8-$^{13}C_2$]-N^6-methyladenosine (*t*BDMS)	8	11 (5)	4	150
[8-^{13}C]-N^2-Ac-guanosine (TOM)	5	5 (4)	18	85
[6-^{13}C, 5-^{2}H]-N^4-Ac-cytidine (TOM)	8	8 (6)	34	85
[5-^{13}C, 5-^{19}F]-N^4-Ac-cytidine (*t*BDMS)	10	8 (6)	4	57
[6-^{13}C, 5-^{2}H]-uridine (TOM)	4	5 (3)	22	85
[5-^{13}C, 5-^{19}F]-uridine (*t*BDMS)	7.5	6 (4)	8	57
[1,3-$^{15}N_2$]-cmo^5-uridine (*t*BDMS)	8	15 (3)	1	149

[a]The 2′-OH protecting groups are listed in the parentheses. [b]Total reaction time was based on the time required for all chemical steps. In addition, 16 h were added for any explicit mention of overnight procedures and 24 h were added for any chromatographic purifications. [c]Reactions for amidites harboring post-transcriptional modifications begin with isotope-labeled precursors whereas reactions for unmodified amidites begin with isotope-labeled protected nucleobase. Also, the number in parentheses represents the number of chromatographic purification steps.

https://doi.org/10.1021/acs.chemrev.1c00845
Chem. Rev. 2022, 122, 9357−9394

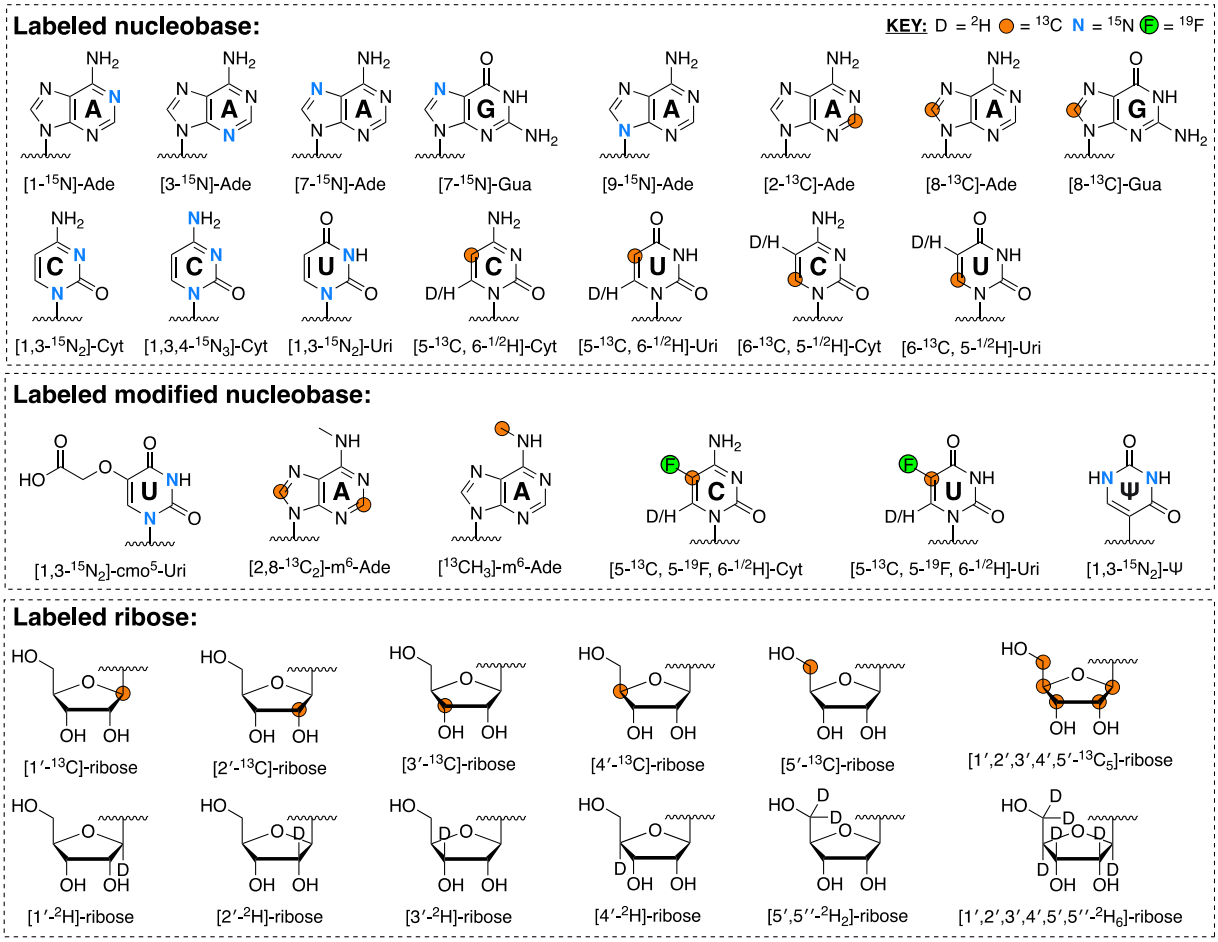

Figure 3. List of possible atom-specifically isotope-labeled nucleobase and ribose labeling patterns. These can be coupled to form rNTPs via chemo-enzymatic synthesis but also converted into amidites with further chemical synthesis. Nucleobase labeling patterns (unmodified and modified) are based on the synthetic schemes described in Sections 3.1 and 3.3. These need not be mutually exclusive, and some labeled sites can be incorporated simultaneously. Labeled ribose, on the other hand, is available from commercial sources (Omicron Biochemicals and CIL).

3.4. Current State of RNA Labeling: Where We Are and Where We Are Headed

Despite the synergy between the synthesis of nucleobases (Section 3.1), rNTPs (Section 3.2), and amidites (Section 3.3), and their contribution to RNA labeling for applications with solution NMR spectroscopy, a number of insurmountable limitations remain for RNAs prepared enzymatically (using, e.g., T7 RNA polymerase) and chemically (i.e., solid-phase synthesis). The former is incapable of position-specific labeling and the latter is size limited, even though both methods can install isolated $^{1}H-^{13}C$ spin pairs into RNA that remove the $^{13}C-^{13}C$ scalar and dipolar couplings that are normally present in uniformly labeled RNA, as will be detailed in Section 4.

Again, unlike DNA template-directed *in vitro* transcription, a tremendous advantage to the field is that amidite labeling and solid-phase synthesis can provide direct read-outs of the biophysical consequences of post-transcriptional modifications. This will be discussed in greater detail in Section 4.2.2.3. However, despite this strength, the "size problem" of solid-phase synthesis limits the production of RNAs to ∼60 nt, beyond which it is exceedingly difficult to prepare RNA in high yield and sufficient purity for NMR studies. Even though the 2′-*O*-CEM[91,146,147] protecting group initially held promise for synthesizing larger RNAs, it has not gained widespread use. Conversely, while much larger RNAs can be transcribed enzymatically, larger RNAs always carry with them more extensive signal overlap and broader linewidths. These complications make NMR analysis of RNAs > 60 nt extremely difficult, even when atom-specific labeling is used. However, introducing $^{13}C-^{19}F$ spin pairs into RNA,[18,57,86] leveraging the spectral properties of the ^{15}N nuclei,[53,154] or combining selective deuteration with ^{1}H NMR[17,53−55] all hold promise to lessen the burden imposed by overlap and broad lines. This will be discussed in detail in Section 5.

It is clear that elucidating the structure, interactions, and dynamics of large RNAs and their complexes (e.g., those implicated in viral transcription, splicing, nuclear export, translation, packaging, and particle assembly) requires developing breakthrough technologies and new experimental strategies to solve the structures of such large RNAs rapidly and accurately. While the advances in the synthesis of atom-specific isotope-labeled rNTPs and amidites are essential first steps in this direction, the ability to incorporate these labels position-specifically will be a game changer for RNA structural and chemical biology. Overnight, it would transform our ability to perform position-specific readouts *in vitro* and *in vivo*. Moreover, it would enable scientists to peer directly into the active site of RNA enzymes, visualize the binding pockets of RNA−drug complexes, and exquisitely map out the interfaces of RNA−protein, RNA−RNA, or RNA−DNA−RNA hybrids.

https://doi.org/10.1021/acs.chemrev.1c00845
Chem. Rev. 2022, 122, 9357−9394

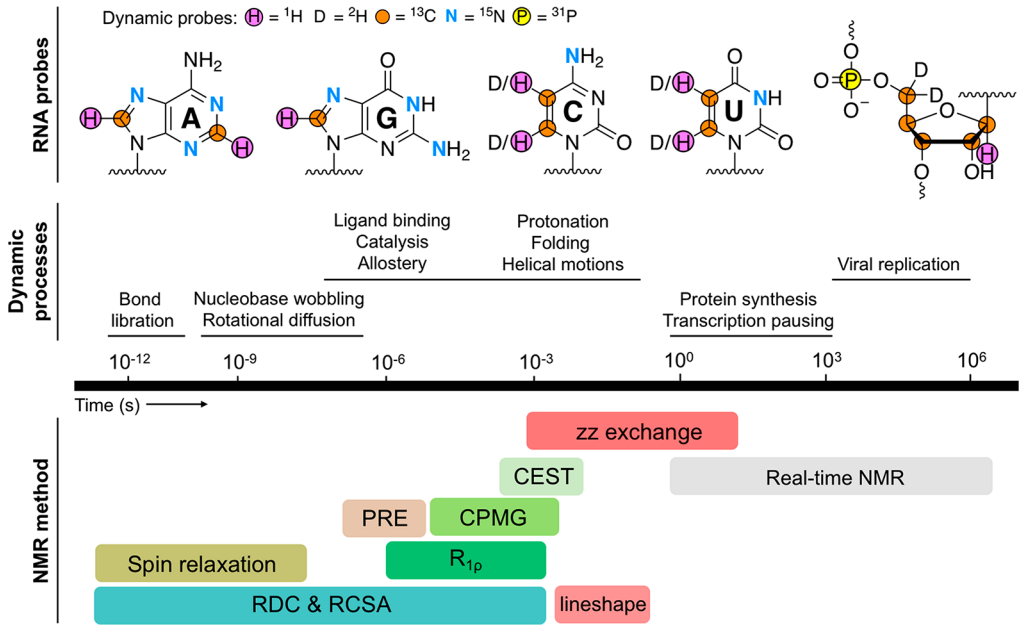

Figure 4. Dynamic processes in RNA and corresponding NMR methods and RNA nuclei that can be used to characterize such motions. The highlighted ^{15}N and ^{13}C sites have been used extensively in NMR spin relaxation and relaxation dispersion experiments,[148] whereas ^{31}P[170,171] and ^{2}H[172] sites are probed less frequently. Alternative time charts can be found elsewhere.[148,169,173,174]

At least that is the dream. While we await these technological advances, the availability of these isotope-labeled RNA building blocks with diverse labeling topologies (Figure 3) still bodes well to address structural dynamic features of RNAs with NMR spectroscopy as well as MS or small angle neutron/X-ray scattering. The remaining sections highlight how the labels described in Section 3 can be exploited to study RNA structure, interactions, and dynamics by NMR spectroscopy.

4. NMR PROBES OF MACROMOLECULAR DYNAMICS

Originating more than 45 years ago, early investigations of RNA dynamics were limited to the study of bacterial tRNAs using one-dimensional (1D) NMR methods.[155] More than a decade later, development of 1D and 2D heteronuclear polarization transfer schemes to measure heteronuclear relaxation rates[156−158] uniquely positioned solution NMR spectroscopy to probe protein[159−162] and RNA[163−167] dynamics. With multidimensional NMR spectroscopy, we can measure the dynamics of ribose, nucleobase, and phosphorus nuclei distributed along the entire RNA structure.[168−172] We can especially characterize motions that range from picosecond to seconds and visualize conformers that are transient and sparsely populated (Figure 4). For these low populated states, we can extract chemical shifts (structure), rates (kinetics), and populations (thermodynamics) under various physiological conditions of temperature, salt, pH, and cellular environment. Finally, we can examine how the cellular milieu modulates the structure, dynamics, and interactions of RNA in real time.

4.1. Probing Fast Motions with Uniform and Selective Labels

On the picosecond (ps)-to-nanosecond (ns) (ps-ns) time scales, spin relaxation provides information about the amplitude and time scale of motions powered by the bond vectors (e.g., ^{15}N−^{1}H, ^{13}C−^{1}H, ^{13}C−^{19}F, ^{1}H−^{1}H) reorienting relative to the external applied magnetic field (Figure 4).[169,175−177] Longitudinal relaxation describes the return to the equilibrium distribution of spins along the z-axis, with a characteristic exponential time constant T_1 (or rate constant $R_1 = 1/T_1$). Transverse relaxation, on the other hand, describes the decay of magnetization in the transverse xy-plane, with a characteristic decay time constant T_2 (or rate constant $R_2 = 1/T_2$). Larger R_2 values produce broader peaks and lower peak heights in an NMR experiment. The linewidth, defined as full-width at half-height (given in Hz), is $\Delta\nu_{1/2} = R_2/\pi$. The heteronuclear Overhauser effect (hNOE) measures the enhancement of the heteroatom magnetization that arises from saturating the proton magnetization, and is mediated by their dipolar interaction.

For an isolated pair of spin-1/2 nuclei S and I (here, S is ^{15}N, ^{13}C, ^{31}P, ^{19}F; and I is ^{1}H), R_1, R_2, and the hNOE of nucleus S are related to the rotational diffusion tensor of the molecule according to well-known relations:[178,179]

$$R_1 = 3(d^2 + c^2)J(\omega_S) + d^2[J(\omega_I - \omega_S) + 6J(\omega_I + \omega_S)] \quad (1)$$

$$R_2 = \frac{1}{2}(d^2 + c^2)[4J(0) + 3J(\omega_S)] + \frac{d^2}{2}[J(\omega_I - \omega_S) + 6J(\omega_I + \omega_S) + 6J(\omega_I)] + R_{ex} \quad (2)$$

$$hNOE = 1 + \left(\frac{\gamma_I}{\gamma_S}\right)\frac{d^2}{R_1}[6J(\omega_I + \omega_S) - J(\omega_I - \omega_S)] \quad (3)$$

$$d = \left(\frac{\mu_0 h \gamma_S \gamma_I}{16\pi^2 r_{SI}^3}\right) \text{ and } c = \omega_S \Delta\sigma_S/3 \quad (4,5)$$

where $\Delta\sigma_S = \sqrt{\sigma_x^2 + \sigma_x^2 - \sigma_x\sigma_y}$, $\sigma_x = \sigma_{33} - \sigma_{11}$, $\sigma_y = \sigma_{33} - \sigma_{22}$, σ_{11}, σ_{22}, and σ_{33} are the principal components of the chemical shielding anisotropy (CSA) tensor,[180,181] $J(\omega)$ is a spectral

https://doi.org/10.1021/acs.chemrev.1c00845
Chem. Rev. 2022, 122, 9357−9394

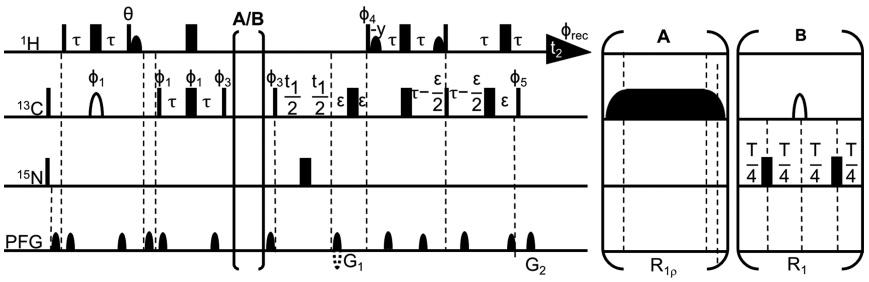

Figure 5. Pulse scheme for transverse relaxation optimized spectroscopy (TROSY)-detected experiments for measuring (A) rotating-frame ($R_{1\rho}$) (from which R_2 can be calculated[186,196]) and (B) ^{13}C R_1 rates in selectively labeled RNA, adapted from previous reports.[196] Quadrature detection and sensitivity-enhanced/gradient-selection is implemented using the Rance-Kay[197,198] echo/antiecho scheme with the polarity of G_1 inverted and phase Φ_4 and Φ_5 incremented 180° for each second FID of the quadrature pair.

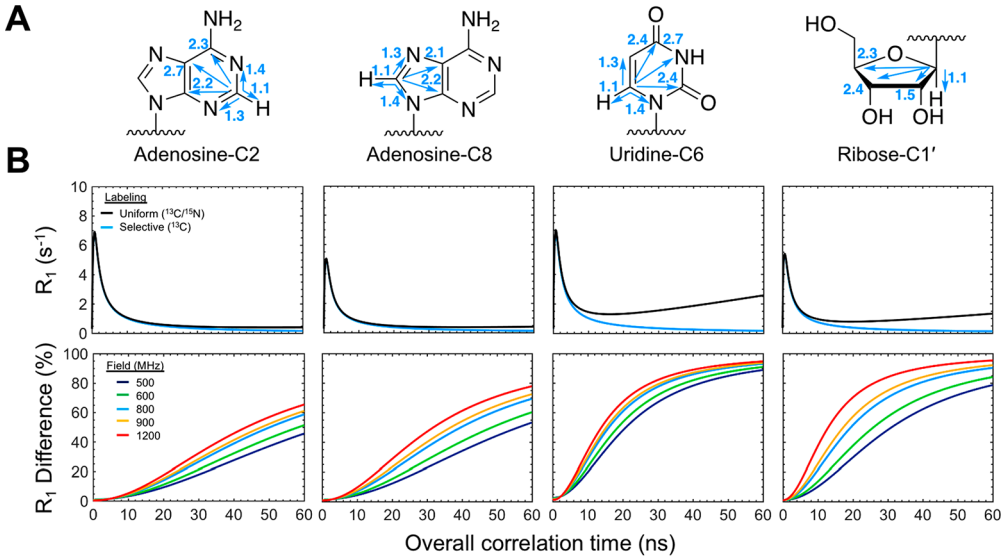

Figure 6. Dipolar couplings complicate dynamics measurements in uniformly labeled RNA. (A) Nucleobase and ribose structures shown to highlight dipolar coupling networks to nuclei of interest (i.e., Ade-C2 and Ade-C8, Uri-C6, and ribose C1′). Distances are shown in units of Å. (B) Simulated R_1 rates and R_1 difference (defined as above) for the nuclei highlighted in panel A. R_1 simulations were carried out for 800 MHz field and R_1 difference simulations were run at multiple magnetic fields. All simulations were carried out at various τ_C values, and additional details can be found in the original works.[188,189]

density function, which is assumed to be a Lorentzian (e.g., simplest form is $J(\omega) = \frac{\tau_C}{1+(\omega\tau_C)^2}$), γ_i is the gyromagnetic ratio of spin i, r_{SI} is the distance between spins I and S, h is Planck's constant, and R_{ex} is the exchange contribution to R_2 due to slow (i.e., microsecond-to-millisecond, μs-ms) motions. The raw data represented by the three relaxation parameters (R_1, R_2, and *hNOE*) reveal the nucleotide level variation of the dynamic motions encoded in the RNA primary sequence. Additional motional variables such as the overall correlation time (τ_C) and generalized order parameter (S) can be fit within a Model Free formalism[182,183] to describe fast (i.e., ps-ns) motions. Though, for reasons enumerated below, this becomes problematic for large uniformly labeled RNAs.[184]

The RNA motions reported by R_1, R_2, and hNOE are easily probed by ^{13}C[163−166,184−189] and ^{15}N[163,167,190] nuclei. ^{15}N sites are present in the four nucleobases at the following sites: adenosine (Ade)-H2-N1, Ade-H2-N3, Ade-H8-N7, and Ade-H8-N9, guanosine (Gua)-H1-N1, Gua-H8-N7, and Gua-H8-N9, uridine (Uri)-H3-N3, and Uri-H6-N1, and cytidine (Cyt)-H6-N1 (Figures 2 and 4). These are suitable reporters of hydrogen-bonding and non-hydrogen-bond dynamics that occur in base-paired and nonbase-paired regions. However, solvent exposed imino regions are usually broadened beyond detection. Nonprotonated nitrogen sites such as Ade-N1 and Ade-N3, purine (Pur)-N7 and Pur-N9, and pyrimidine (Pyr)-N1 remain underutilized. The limited availability of directly protonated imino nitrogen probes has made protonated carbons an attractive alternative for probing RNA relaxation. These sites are found in both the ribose (C1′−C5′) and nucleobase (Ade-C2, Pur-C8, Pyr-C5, and Pyr-C6) moieties (Figures 2 and 4).

Despite the greater number of detectable ^{13}C nuclei in RNA, complications arise for measurements and analysis of ^{13}C relaxation. First, the carbon sites are linked by intricate multibond couplings (i.e., to ^{15}N, ^{13}C, and ^{1}H nuclei) that are proximally positioned within 3 Å or less. Therefore, ^{13}C spins do not approximate an isolated two-spin system. In uniformly labeled samples, these extensive dipolar couplings complicate ^{13}C R_1 rate measurements and analysis[120,121,185,186,188,189,191−195] in biopolymers of large size (τ_C > 7 ns). Given this fact, our group has developed pulse schemes (based on the isolated $^{1}H-^{15}N$ backbone amide spin pair in proteins[196]) to leverage the isolated $^{1}H-^{13}C$ spin pairs afforded by our atom-specifically labeled RNA samples (Figure 5).

https://doi.org/10.1021/acs.chemrev.1c00845
Chem. Rev. 2022, 122, 9357−9394

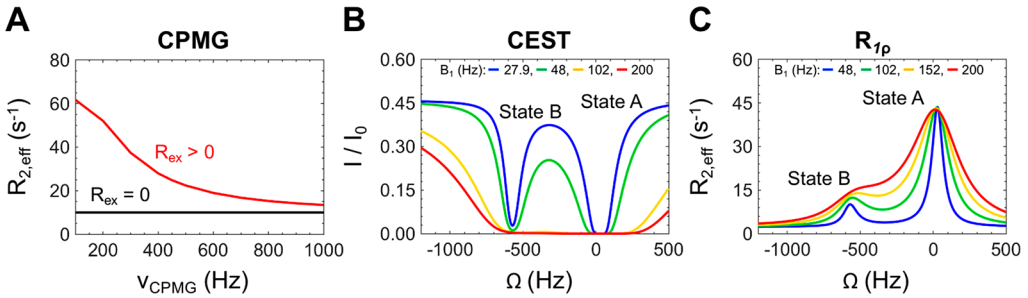

Figure 7. Simulated NMR RD experiments. (A) CPMG curves for two nuclei: one in exchange (in red, $R_{ex} > 0$) using the parameters $k_{ex} = 794\ s^{-1}$, $p_B = 8.7\%$, and $\Delta\omega = 228$ Hz (150 MHz ^{13}C-Larmor frequency) and one without (in black, $R_{ex} = 0$, or $\Delta\omega = 0$, or both), based on published data.[211] (B) CEST profile for a given nuclei showing evidence of two states A and B. Calculations assumed $k_{ex} = 121\ s^{-1}$, $p_B = 10.8\%$, $\gamma(^1H)B_0/2\pi = 600$ MHz, $\Delta\omega = -4$ ppm, $R_1^A = R_1^B$, $T = 0.3$ s, and the B_1 fields specified on the figure. (C) $R_{1\rho}$ profile for a given nuclei showing evidence of two states A and B. Calculations used the same parameters as in (B) but with different B_1 fields, which are again specified on the figure. As seen in the CEST and $R_{1\rho}$ profiles, at higher B_1 fields, linewidths broaden to the point where state B becomes increasingly difficult to detect. CEST and $R_{1\rho}$ profiles are based on published data.[212]

Theoretical simulations of R_1 rates for Pyr-C5 and Pyr-C6, ribose C1′, Ade-C2, and Pur-C8 in uniformly and selectively labeled RNAs suggest that the various $^1H-^{13}C$, $^{13}C-^{13}C$, and $^{13}C-^{15}N$ dipolar couplings (Figure 6A) present in uniformly labeled samples lead to overestimated R_1 rates (Figure 6B). Moreover, this discrepancy, measured by the R_1 difference (where R_1 difference = $[100 \times (R_{1,uni} - R_{1,sel})/R_{1,uni})]$), increases with higher molecular weights and magnetic field strengths (Figure 6B). Experimental measurements with our customized pulse sequence (for selectively labeled RNA) (Figure 5) and those of others[186] (for uniformly labeled RNA), corroborated our simulations, suggesting that these discrepancies in R_1 cannot be wholly ignored, even for fairly isolated Ade-C2 and Pur-C8 sites.[188,189] Taken together, the contribution of $^{13}C-^{13}C$ dipolar interactions needs to be explicitly taken into consideration in data analysis of uniformly labeled RNA. Spin relaxation measurements on uniformly labeled RNA from Al-Hashimi and co-workers[186] demonstrate that this is not an insurmountable hurdle. Nevertheless, the focus of our discussion on RNA dynamics will center on slower conformational exchange motions, which will be discussed in Section 4.2.

4.2. Probing Slow Motions with Uniform and Selective Labels: Relaxation Dispersion and Saturation Transfer Methods

Spin-1/2 nuclei with a positive gyromagnetic ratio either align parallel (α, high-populated, favorable energetic state) to the static NMR magnetic field (B_0) or antiparallel (β, low-populated, unfavorable state). The net bulk magnetization, oriented parallel to B_0, can be realigned with radiofrequency (RF) pulses along a direction perpendicular to B_0. The magnetization then precesses about B_0 at a resonant Larmor frequency (ω) characteristic of the nucleus. When Fourier transformed, this detectable oscillating time-domain signal yields a frequency-domain NMR spectrum with signals at characteristic frequencies for each nucleus. When referenced against a standard frequency (e.g., sodium-3-(trimethylsilyl)-1-propanesulfonate (DSS) for ^1H), we obtain a field-independent chemical shift that is directly proportional to the energy difference between the α and β states.

For RNA exchanging between two states A and B, the chemical shift difference ($\Delta\omega$) between the two states and the exchange rate constant [k_{ex}, sum of the forward (k_{AB}) and reverse (k_{BA}) rate constants] or the exchange lifetime ($\tau_{ex} = 1/k_{ex}$) determine if two distinct NMR peaks are observed and what signal intensity and linewidth are obtained for a given nucleus.[199,200] In the slow exchange regime, two distinct peaks are detected at the chemical shifts of the individual states, and the peak intensities are proportional to the populations of each state. In the fast exchange regime, k_{ex} is much larger than $\Delta\omega$, and therefore, a single peak is observed at the population-weighted average chemical shift. In the intermediate exchange regime, which, as its name implies, lies between the fast and slow time scales, $k_{ex} \approx \Delta\omega$.

Regardless of the exchange regime, if chemical exchange is present, R_2 increases by R_{ex}, which depends on k_{ex} and $\Delta\omega$ and can therefore be modulated by magnetic field strength.[199−203] Dynamics on the intermediate and slow time scales (i.e., μs-ms) can be characterized with relaxation dispersion (RD) using $R_{1\rho}$,[203,204] Carr−Purcell−Meiboom−Gill (CPMG),[205−207] or chemical exchange saturation transfer (CEST)[208] experiments (Figure 4). Moreover, even processes slower than seconds can be studied with real-time NMR (Figure 4).[209]

For two-site exchange, a general expression for the R_2 rate constant ($R_{CPMG}(\tau_{cp})$) for state A (where $p_A > p_B$), that encompasses all conformational exchange time scales, is given by the Carver-Richards equation:[199,210]

$$R_{CPMG}(\tau_{cp}) = \frac{1}{2}\left(R_2^A + R_2^B + k_{ex} - \frac{1}{2\tau_{cp}}\cos h^{-1} \times [D_+\cos h(\eta_+) - D_-\cos(\eta_-)]\right) \quad (6)$$

$$\eta_\pm = \sqrt{2}\,\tau_{cp}[\pm\psi + (\psi^2 + \xi^2)^{1/2}]^{1/2} \quad (7)$$

$$D_\pm = \frac{1}{2}\left[\pm 1 + \frac{\psi + 2\Delta\omega^2}{(\psi^2 + \xi^2)^{1/2}}\right] \quad (8)$$

$$\psi = (R_2^A - R_2^B - p_A k_{ex} + p_B k_{ex})^2 - \Delta\omega^2 + 4p_B p_A k_{ex}{}^2 \quad (9)$$

$$\xi = 2\Delta\omega(R_2^A - R_2^B - p_A k_{ex} + p_B k_{ex}) \quad (10)$$

where $R_2^{A/B}$ and $p_{A/B}$ are the R_2 rate and relative populations of the A/B state, respectively. A main disadvantage of the CPMG experiment is that only the magnitude (and not the sign) of

https://doi.org/10.1021/acs.chemrev.1c00845
Chem. Rev. 2022, 122, 9357−9394

$\Delta\omega$ is obtained. Still, this disadvantage of the CPMG experiment is offset by the relative ease of its implementation and data analysis. That is, conformational exchange is easily detected by a nonflat CPMG curve when plotting $R_{2,\mathrm{eff}}$ versus ν_{CPMG} (Figure 7A). Nonexchanging nuclei, on the other hand, have no dependence of $R_{2,\mathrm{eff}}$ on ν_{CPMG} and therefore appear as flat curves (Figure 7A).

$R_{1\rho}$ and CEST experiments provide more robust information regarding the chemical shifts of state B. For a two-site model, $\Delta\omega$, k_{ex}, and p_{B} can be extracted from CEST profiles using the Bloch-McConnell 7 × 7 matrix (including the equilibrium magnetization terms).[213−215] By combining all data sets, global k_{ex} and p_{B} values can be fit numerically for all the CEST profiles, plotted as I/I_0 versus spin-lock offset (in Hz) (Figure 7B). The 7 × 7 two-site Bloch-McConnell equation is derived from the relaxation matrix and the kinetic rate matrix for an exchanging two-site system:[208,212,214,215]

$$\frac{\mathrm{d}}{\mathrm{d}t}\begin{bmatrix} E/2 \\ A_x \\ A_y \\ A_z \\ B_x \\ B_y \\ B_z \end{bmatrix} = \begin{bmatrix} 0 & 0 & 0 & 0 & 0 & 0 & 0 \\ 0 & -R_2^{\mathrm{A}} - k_{\mathrm{AB}} & -\omega_{\mathrm{A}} & \omega_1 & k_{\mathrm{BA}} & 0 & 0 \\ 0 & \omega_{\mathrm{A}} & -R_2^{\mathrm{A}} - k_{\mathrm{AB}} & 0 & 0 & k_{\mathrm{BA}} & 0 \\ 2R_1^{\mathrm{A}}p_{\mathrm{A}} & -\omega_1 & 0 & -R_1^{\mathrm{A}} - k_{\mathrm{AB}} & 0 & 0 & k_{\mathrm{BA}} \\ 0 & k_{\mathrm{AB}} & 0 & 0 & -R_2^{\mathrm{B}} - k_{\mathrm{BA}} & -\omega_{\mathrm{B}} & \omega_1 \\ 0 & 0 & k_{\mathrm{AB}} & 0 & \omega_{\mathrm{B}} & -R_2^{\mathrm{B}} - k_{\mathrm{BA}} & 0 \\ 2R_1^{\mathrm{B}}p_{\mathrm{B}} & 0 & 0 & k_{\mathrm{AB}} & -\omega_1 & 0 & -R_1^{\mathrm{B}} - k_{\mathrm{BA}} \end{bmatrix} \begin{bmatrix} E/2 \\ A_x \\ A_y \\ A_z \\ B_x \\ B_y \\ B_z \end{bmatrix} \tag{11}$$

where $R_1^{\mathrm{A/B}}$, $\omega_{\mathrm{A/B}}$, and ω_1 are the R_1 rate of the A/B state, the offset of the B_1 spin-lock field from the peaks in the A/B state (in rad s^{-1}), and the B_1 field strength (in rad s^{-1}), respectively. The evolution of magnetization for the peak in state A during the CEST spinlock period is given by

$$M(t) = M(0) \times e^{(-L\times t)} \tag{12}$$

Similarly, under the $R_{1\rho}$ model for two-site exchange, the $R_{1\rho}$ value for state A magnetization is given by[216]

$$R_{1\rho} = \frac{-1}{T_{\mathrm{relax}}} \times \ln(M_0^T e^{RT_{\mathrm{relax}}} \times M_0) \tag{13}$$

and

$$R = \begin{bmatrix} -R_2^{\mathrm{A}} - k_{\mathrm{AB}} & -\omega_{\mathrm{A}} & 0 & k_{\mathrm{BA}} & 0 & 0 \\ \omega_{\mathrm{A}} & -R_2^{\mathrm{A}} - k_{\mathrm{AB}} & -\omega_1 & 0 & k_{\mathrm{BA}} & 0 \\ 0 & \omega_1 & -R_1^{\mathrm{A}} - k_{\mathrm{AB}} & 0 & 0 & k_{\mathrm{BA}} \\ k_{\mathrm{AB}} & 0 & 0 & -R_2^{\mathrm{B}} - k_{\mathrm{BA}} & -\omega_{\mathrm{B}} & 0 \\ 0 & k_{\mathrm{AB}} & 0 & \omega_{\mathrm{B}} & -R_2^{\mathrm{B}} - k_{\mathrm{BA}} & -\omega_1 \\ 0 & 0 & k_{\mathrm{AB}} & 0 & \omega_1 & -R_1^{\mathrm{B}} - k_{\mathrm{BA}} \end{bmatrix} \tag{14}$$

$$M_0 = \begin{bmatrix} p_A \sin\theta \\ 0 \\ p_A \cos\theta \\ 0 \\ 0 \\ 0 \end{bmatrix} \text{ and } \theta = \tan^{-1}\left(\frac{\omega_1}{\Omega}\right) \tag{15,16}$$

where $\Omega = \omega_{\mathrm{rf}} - \Omega_{\mathrm{obs}}$ is the difference between the resonance frequency of the observed nucleus (Ω_{obs}) and the spinlock transmitter frequency (ω_{rf}). For $R_{1\rho}$ experiments, conformational exchange can be detected by plotting $R_{2,\mathrm{eff}}$ versus $\Omega/2\pi$ (Figure 7C). The expression for CEST and $R_{1\rho}$ (eqs 11−16) provide insight into the parameters that are important for acquiring useful data. For example, higher B_1 fields decrease chemical shift resolution between states and also broadens linewidths (Figure 7B,C).

While almost all RD studies involve two-site systems, expressions for CPMG, $R_{1\rho}$, and CEST models for characterizing N-site exchange have been described by Arthur Palmer III and co-workers.[199] Indeed, work from Al-Hashimi and co-workers on Watson−Crick mismatches and base pair reshuffling in RNA feature $R_{1\rho}$ and CEST data that described three-site exchange.[217]

4.2.1. Slow Motions: Are Selective Labels Needed? As with spin relaxation, the scalar and dipolar couplings present in uniformly labeled samples can lead to complications in RD and CEST experiments. As we have discussed elsewhere,[75] numerous spectroscopic solutions have been proposed to circumvent the problems that arise from $^{13}C-^{13}C$ couplings that exist in uniformly labeled RNA. These advances include constant time evolution,[218−221] adiabatic band selective decoupling,[222−224] and selective cross-polarization with weak RF fields.[225−227] These solutions have benefited RD and CEST experiments to varying degrees in RNA. Specifically, $^{13}C-^{13}C$ scalar couplings (e.g., C1′−C2′ or C5−C6) complicate CPMG

https://doi.org/10.1021/acs.chemrev.1c00845
Chem. Rev. 2022, 122, 9357−9394

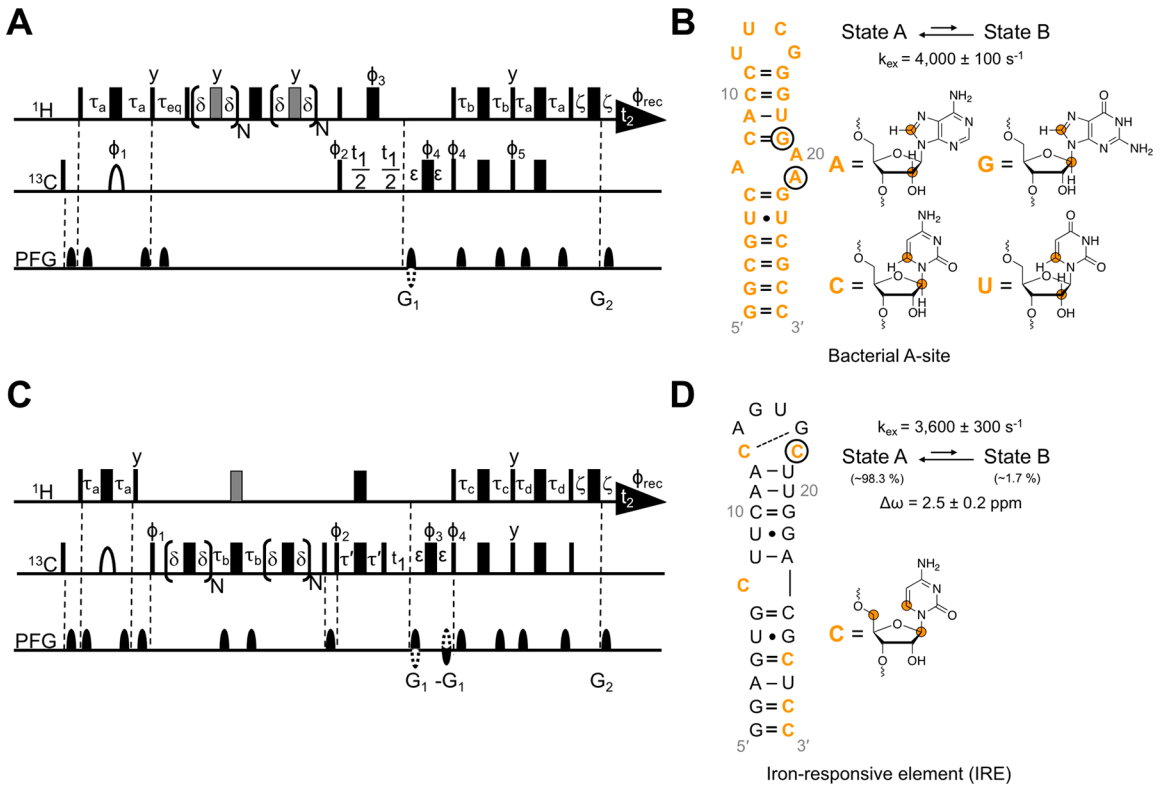

Figure 8. (A) Pulse scheme for SQ ^{1}H CPMG experiment for selectively labeled RNA,[228] adapted from previous reports.[254,255] (B) Secondary structure of the 27 nt bacterial A-site RNA with all nucleotides harboring isotope labels shown bolded in orange. Nucleotides that were found to be in exchange are circled. Exchange parameters were extracted from a global fit of the CPMG data (i.e., G19-C8 and A21-C8). (C) Pulse scheme for methylene CH_2 ^{1}H−^{13}C TROSY-detected CPMG experiment for selectively labeled RNA,[228] adapted from previous reports.[257] (D) Secondary structure of the 29 nt iron-responsive element (IRE) RNA with isotope labels and nucleotides in exchange presented as in panel B. Exchange parameters were extracted from a global fit of the CPMG data (i.e., C18−C5′, C18−C1′, and C18−C6) and likely refer to a structural rearrangement in the IRE triloop. Orange circles and D refer to ^{13}C and ^{2}H nuclei, respectively. Additional details can be found in the original work.[228]

experiments[228,229] to a much larger degree than both CEST and $R_{1\rho}$. However, these couplings still pose a problem to CEST[230,231] and $R_{1\rho}$[212] and oscillations are sometimes observed in the decay profiles of C1′ and C6 nuclei. Moreover, as with spin relaxation, these couplings must be explicitly taken into consideration in data analysis. The number of coupled homogeneous differential equations (n) is equal to $(2 \times 4^m) - 1$, where m is the number of weakly coupled nuclear spins in an m-spin system. Therefore, for 1-, 2-, and 3-spin systems, n = 7, 31, and 127, respectively.[214,215,231] This transforms the CEST matrix (eq 11) from 7 × 7 to 31 × 31 for ^{13}C−^{13}C scalar coupled spin pairs found in the nucleobase and ribose moieties. Atom-specific labeling (Section 3), on the other hand, circumvents this problem entirely, and dramatically simplifies NMR spectra, especially when incorporated position-specifically via solid-phase synthesis (Section 3.3). However, a drawback for selective labels is the obvious reduction of probe sites.

Nevertheless, using both selective and uniformly labeled RNA, CEST and $R_{1\rho}$ experiments have now been applied to the protonated nucleobase (Pyr-C5 and Pyr-C6, Pur-C8, and Ade-C2) and ribose (C1′-C5′) carbons, the nucleobase imino (Gua-N1 and Thy/Uri-N3) and amino (Gua-N2) nitrogen, nucleobase (Uri-H3, Gua-H1, Ade-H2, Pur-H8, Pyr-H5, and Pyr-H6) and ribose H1′ protons, as well as nonprotonated (Gua-N7, Ade-N1, and Pur-N7) and amino (Cyt-N4) nitrogen sites (Figure 4).[75,148,168,212,232−234] In practice, CPMG experiments are solely implemented on selectively labeled RNA, and mainly from our group[75,145,228] and the Kreutz group,[82,85,89,211,235] though not exclusively.[194] CEST and $R_{1\rho}$, on the other hand, have been used to great success with uniformly labeled RNA by the Al-Hashimi,[31,148,168,236−246] Petzold,[247,248] and Zhang[212,232,249−251] groups. Moreover, Petzold and co-workers have developed a SELective Optimized Proton Experiment (SELOPE) approach[252] that can be implemented with $R_{1\rho}$ and CEST[253] experiments using unlabeled samples. The rest of this section will highlight recent examples of RD experiments on labeled (selectively and uniformly) and unlabeled RNA.

4.2.2. Examples of Relaxation Dispersion Experiments in Selectively Labeled RNA. As highlighted above, implementation of RD experiments on selectively labeled RNA circumvents all complications from strong ^{13}C−^{13}C scalar couplings and permits straightforward data analysis. The following sections will be devoted to showcasing examples of CPMG, CEST, and $R_{1\rho}$ experiments performed on selectively labeled RNAs. Specifically, we will highlight recent work from our group[228,234] using isotope-labeled rNTPs and from Kreutz and Al-Hashimi and co-workers[151] using isotope-labeled amidites with post-transcriptional modifications.

4.2.2.1. CPMG in Atom-Specifically Labeled RNA. Until recently, CPMG experiments to measure the chemical shifts of nucleobase methine ^{1}H and ribose methylene C5′(H_2) in a low populated, transient state (i.e., state B) were not available.

https://doi.org/10.1021/acs.chemrev.1c00845
Chem. Rev. 2022, 122, 9357−9394

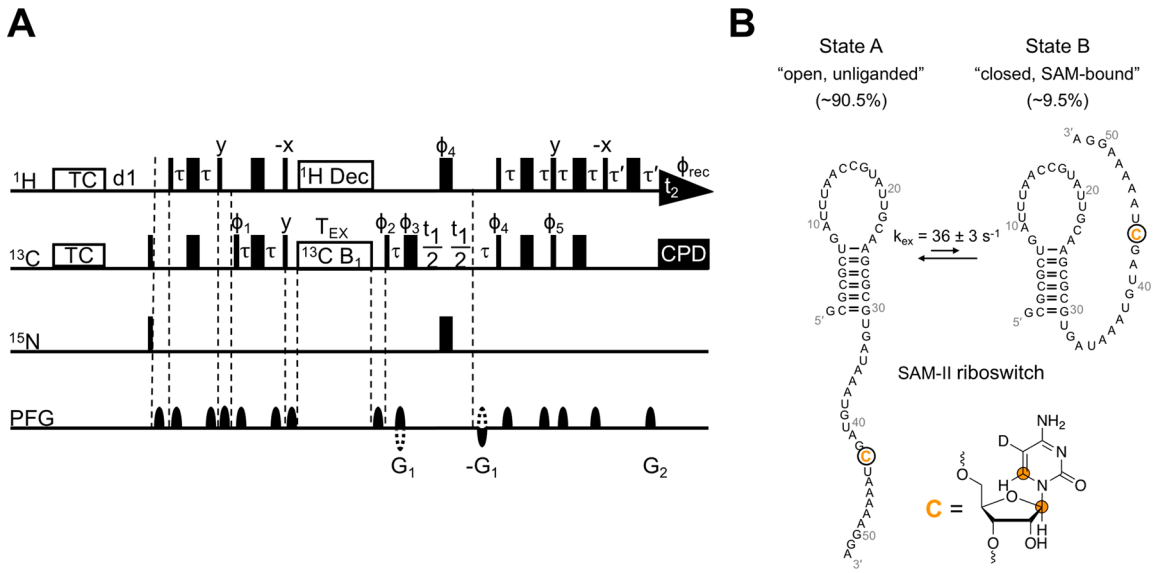

Figure 9. (A) Pulse scheme for ^{13}C and ^{1}H CEST experiments with temperature compensation (TC) and ^{1}H decoupling (^{1}H Dec) for selectively labeled RNA,[234] adapted from previous reports.[212,214] (B) Secondary structure of the 52 nt SAM-II riboswitch RNA. C43 position-specific labeling is shown bolded in orange and circled to indicate that it was the subject of CEST experiments. Exchange parameters were extracted from a global fit of the CEST data (i.e., C43−C1′ and C43−C6) and reveal a transition from an open to a closed conformation that resembles the SAM-bound form. Orange circles and D refer to ^{13}C and ^{2}H nuclei, respectively. Additional details can be found in the original work.[234]

This gap existed, in part, due to complications from ^{13}C−^{13}C scalar couplings. To fill this knowledge gap, our group adapted single-quantum (SQ) ^{1}H CPMG experiments previously designed for methyl groups in protein side-chains[254,255] to obtain CPMG data for the selectively labeled ([2′,8-$^{13}C_2$]-ATP, [1′,6-$^{13}C_2$]-CTP, [1′,8-$^{13}C_2$]-GTP, and [2′,6-$^{13}C_2$]-UTP) bacterial A-site RNA (Figures 8A,B).[228]

The SQ ^{1}H CPMG experiment was amenable to Pur-H8 sites, detecting exchange in G19 and A21. The extracted exchange rate (k_{ex} = 4000 ± 100 s^{-1}) from a global fit was consistent with that determined from a standard ^{1}H−^{13}C TROSY CPMG experiment (k_{ex} = 3000 ± 800 s^{-1}), demonstrating that these new experiments are feasible for RNA (Figure 8B).[228] Moreover, these data agree with $R_{1\rho}$ measurements on uniformly labeled RNA from Al-Hashimi and co-workers, which suggests that each measurement, using various methods and labeling techniques, is picking up fundamental motions within this RNA.[256] In addition, these SQ experiments could provide important data on ^{1}H chemical shifts, which are currently lacking, such as ribose H1′ and Pyr-H6. In the latter case, however, the presence of Pyr-H5 can cause dispersive CPMG patterns for the H6 site.[228] Fortunately, Pyr-H5 deuteration is easily achieved (Scheme 1),[85] and therefore, this experiment can be readily implemented to obtain data for Pyr-H6 sites.

Our group also designed a CH_2 ^{1}H−^{13}C TROSY-detected CPMG pulse sequence (Figure 8C)[228,257] to leverage the isolated ^{13}C spin at the ribose C5′ position (Figure 4) afforded by our chemo-enzymatic labeling (Sections 3.1 and 3.2).[74,75,129] This new CPMG experiment was implemented using the selectively labeled ([1′,5′,6-$^{13}C_3$, 5-^{2}H]-CTP) iron-responsive element (IRE) RNA and detected exchange in C18−C5′ (Figure 8D).[228] These data were then globally fit with additional CPMG data from other nuclei to obtain chemical shift ($\Delta\omega$ = 2.5 ± 0.2 ppm), population (p_B = 1.7 ± 0.2%), and exchange rate (k_{ex} = 3600 ± 300 s^{-1}) information that suggests a significant structural rearrangement in the IRE triloop (Figure 8D).[228]

4.2.2.2. CEST in Atom- and Position-Specifically Labeled RNA. In addition to using selective labels to benefit CPMG experiments, they can also be used to simplify CEST experiments. Specifically, our group combined enzymatic ligation, chemo-enzymatic labeling, and newly developed CEST experiments (Figure 9A) to study the conformational equilibria of the SAM-II riboswitch in the apo (ligand-free) state.[234] To understand the formation of the SAM metabolite-binding pocket, a SAM-II RNA was constructed via DNA splinted ligation with T4 DNA ligase (EC 6.5.1.1) of two RNA fragments: an unlabeled 31 nt acceptor fragment and a [1′,6-$^{13}C_2$, 5-^{2}H]-CTP labeled 21 nt donor fragment. This strategy enabled position-specific labeling, given that there was only one cytidine (C43) in the donor sequence and therefore permitted direct monitoring of the G22−C43 base pair interaction in the SAM binding pocket. Moreover, the isolated spin pair labeling topology enabled the design of a ^{1}H CEST experiment, and simplified setup and analysis of ^{1}H and ^{13}C CEST experiments without complications from ^{13}C−^{13}C couplings to Cyt-C1′ and Cyt-C6 sites.[230]

To leverage the labeling scheme, our group designed a new ^{13}C CEST experiment based on previous pulse schemes[212,214] and used it on the apo SAM-II riboswitch (Figure 9A). The CEST profiles of C43−C1′ and C43−C6 indicated two states of the free SAM-II riboswitch: one that matched the resonance of the ligand-free, highly populated conformation (i.e., state A) and another that matched the ligand-bound, transient conformation (i.e., state B) (Figure 9B).[234] We then used our new ^{1}H CEST experiment (Figure 9A) to indirectly obtain the C43−H1′ chemical shift of state A and B.[234] In agreement with the ^{13}C data, the ^{1}H chemical shift of state B matched the ligand-bound SAM-II (Figure 9B).[234] Taken together, these results suggest that the apo SAM-II exists in a dynamic equilibrium (k_{ex} = 36 ± 3 s^{-1}) between an open (highly populated, p_A = 90.5 ± 0.5%) and a partially closed (transient,

https://doi.org/10.1021/acs.chemrev.1c00845
Chem. Rev. 2022, 122, 9357−9394

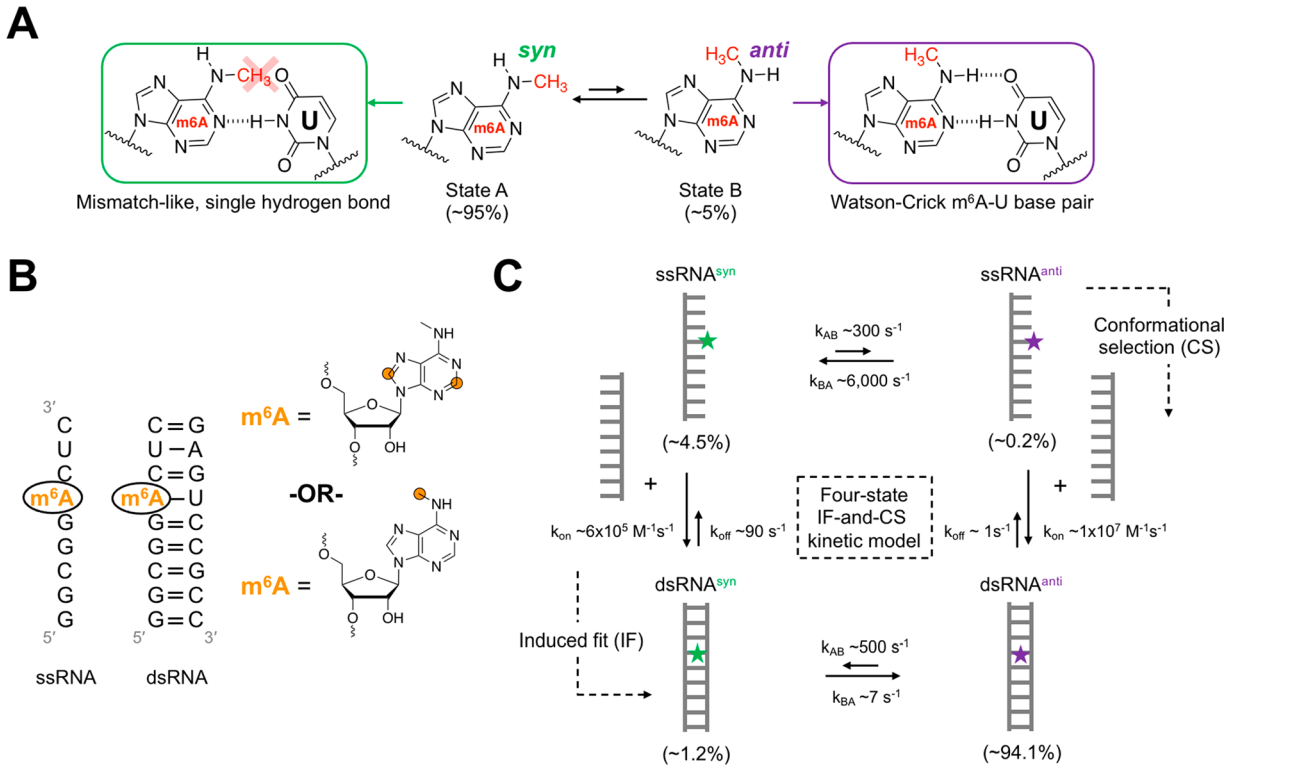

Figure 10. (A) Equilibrium between *syn*:*anti* conformations of the m^{6}A nucleobase and the types of base pairing that each conformation can adopt.[279−281] (B) Secondary structure of the 9 and 18 nt ssRNA and dsRNA that were position-specifically labeled with isotope-labeled m^{6}A, as shown bolded in orange and circled to indicate that it was the subject of RD and CEST experiments. RNA samples harboring m^{6}A were either made with [2,8-$^{13}C_2$]-m^{6}A (top) or [$^{13}CH_3$]-m^{6}A (bottom) labels to obtain ^{13}C RD and CEST data for CH_3 (methyl), C2, or C8 sites. (C) Schematic of the four-state CS-and-IF kinetic model with rate constants shown from RD and CEST data collected at 65 °C.[151] Orange circles refer to ^{13}C. Additional details can be found in the original work.[151]

p_B = 9.5 ± 0.5%) state (Figure 9B).[234] Moreover, these results underscore the emerging consensus that transient, low populated states likely enhance rapid ligand recognition and therefore play a potentially ubiquitous role in RNA recognition and signaling.

4.2.2.3. $R_{1\rho}$ and CEST in Atom- and Position-Specifically Labeled RNA Harboring Post-transcriptional Modifications. Perhaps the greatest benefit of selective labeling is the ability to monitor the structural dynamic consequences of epigenetic and post-transcriptional modifications. Using labels created by Kreutz and co-workers, the Al-Hashimi group has been at the forefront of exploring how these modifications alter the dynamic ensembles of nucleic acids.[149−151,233,258−261] One such example is m^{6}A, an abundant RNA post-transcriptional modification that modulates gene expression,[262−264] viral lifecycles,[265−271] and other biological phenomena.[272−275] Recent work from the Al-Hashimi group demonstrated that m^{6}A preferentially slows RNA duplex annealing with minimal effect on the rate of duplex melting.[150] The effect of m^{6}A on hybridization kinetics stands in contrast to the effect of mismatches. Mismatches also slow the rate of duplex annealing but dramatically increase the rate of duplex melting.[276−278] Of critical importance, the methylamino group of the m^{6}A nucleobase can form two rotational isomers that interconvert on the millisecond time scale[279,280] (Figure 10A). The preferred *syn* isomer (i.e., high-populated, state A) cannot form a canonical Watson−Crick base pair with uridine due to a steric clash between the uridine keto group and the methylamino[279−281] and is therefore mismatch-like (Figure 10A). Instead, when base-paired with uridine, the methylamino rotates into the *anti* isomer (i.e., transient, state B) to form a canonical Watson−Crick m^{6}A:U base pair (Figure 10A).

Kinetic mechanisms that involve binding and conformational change can occur via pathways wherein the conformational change occurs prior to (conformational selection, CS) or post (induced fit, IF) binding. Al-Hashimi and co-workers employed their recently developed RD-based and CEST experiments[31,148,168,237−246] to measure hybridization kinetics of single- and double-stranded RNA (ssRNA and dsRNA, respectively) harboring atom- and position-specifically labeled m^{6}A probes (i.e., [2,8-$^{13}C_2$]-m^{6}A or [$^{13}CH_3$]-m^{6}A) (Figure 10B) to determine how m^{6}A modulates hybridization.[151] In this way, they had direct readouts of the effects of the m^{6}A isomers on Watson-Crick or mismatch-like hybridizations. They showed that m^{6}A with the methylamino group in the *anti* conformation forms a Watson−Crick base pair with uridine that transiently isomerizes on the millisecond time scale to a singly hydrogen-bonded ($p_B \approx 1\%$) mismatch-like conformation, with the methylamino group in the *syn* conformation.[151] This rapid interconversion between Watson−Crick and mismatch forms, combined with different *syn*:*anti* preferences in ssRNA and dsRNA states, hints at how m^{6}A slows duplex annealing without affecting melting via two pathways in which isomerization occurs before (CS) or after (IF) duplex annealing (Figure 10C).[151]

4.2.3. Examples of Relaxation Dispersion Experiments without Selectively Labeled RNA. While RD experiments work well with selective labels, it is not a prerequisite, as long as care is taken to either minimize strong ^{13}C−^{13}C scalar couplings (i.e., probe nuclei where these are

https://doi.org/10.1021/acs.chemrev.1c00845
Chem. Rev. 2022, 122, 9357−9394

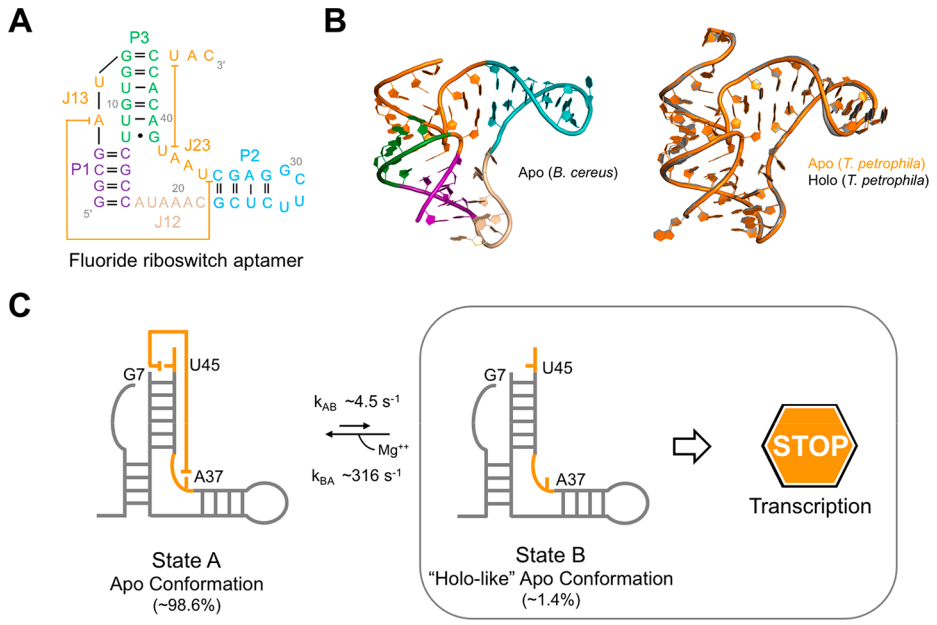

Figure 11. (A) Secondary structure of the 48 nt fluoride riboswitch aptamer RNA with domains labeled by color. (B) Solution NMR structure[250] of the apo aptamer (*B. cereus*) (PDB ID, 5KH8) (left) compared to crystal structures[282] of the apo (PDB ID, 4ENC) and holo (PDB ID, 3VRS) aptamers (*T. petrophila*). In solution, the aptamer adopts near-identical structures in the apo and holo forms, in agreement with crystallography.[250,282] (C) Schematic of the equilibrium between the highly populated apo state (i.e., State A) and the transient "holo-like" conformation of the apo state (i.e., State B). Exchange parameters were extracted from a global fit of the CEST data. The transient "holo-like" conformation of the apo state (i.e., State B) occludes the formation of a reverse Hoogsteen base pair in the highly populated conformation of the apo state (i.e., State A) to signal transcription termination. Additional details can be found in the original work.[250]

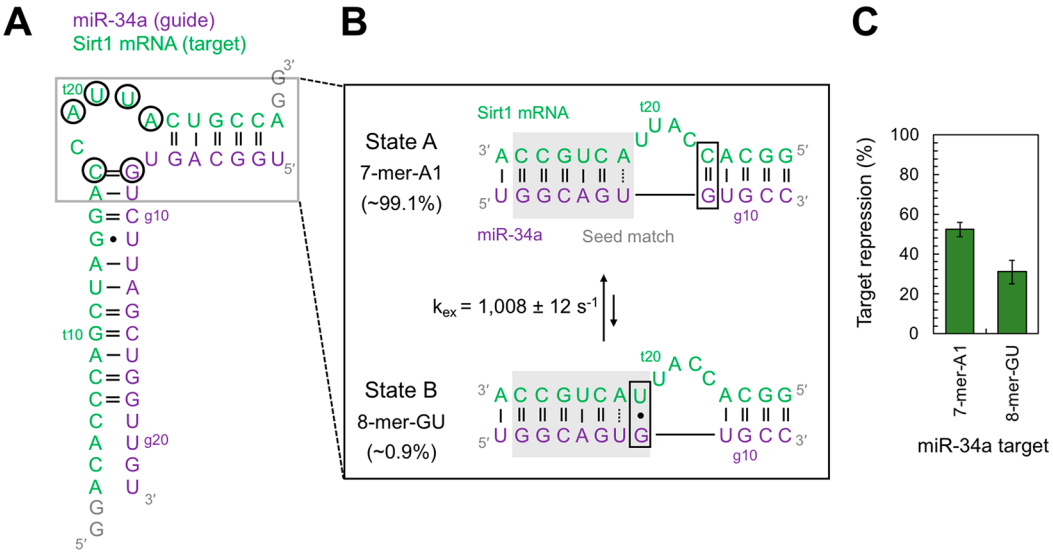

Figure 12. (A) Secondary structure of the mir-34a–mSirt1 duplex.[247] Nucleotides that were found to be in exchange are circled. (B) Schematic of the equilibrium between the highly populated 7-mer-A1 and transient 8-mer-GU mir-34a–mSirt1 duplex. Exchange parameters were extracted from a global fit of the $R_{1\rho}$ data (i.e., gG8-H1, gG8-N1, gG8-C8, tC17-C1′, tA19-C8, tU20-C1′, tU21-C6, and tA22-C8). The boxed nucleotides represent the critical switch from the gG8:tC17 to gG8:tU21 base pair. (C) Replotted functional data[247] showing the percentage of target repression for each miR-34a duplex. The transient 8-mer-GU reduces target mRNA levels ~2-fold compared to the highly populated 7-mer-A1. The 8-mer-GU duplex therefore represents a "catalytically competent RISC". Additional details can be found in the original work.[247]

minimized) or take them into consideration in data analysis. The following sections will be devoted to showcasing examples of CEST and $R_{1\rho}$ experiments performed without selectively labeled RNA. We will highlight recent work from the Zhang[250] and Petzold[247] groups using uniformly $^{13}C/^{15}N$-labeled rNTPs and also new experiments from the Petzold[252] and Al-Hashimi[253] groups that require no labels at all.

4.2.3.1. CEST and $R_{1\rho}$ Experiments in Uniformly Labeled RNA. RNA dynamics can regulate biological processes from transcription to translation. One such example is the *Bacillus cereus* fluoride riboswitch RNA (Figure 11A), which has been characterized extensively by Zhang and co-workers.[250] Here, they showed that the riboswitch aptamer adopts a near-identical solution structure[250] with (holo) and without (apo) the fluoride ligand, in agreement with X-ray crystal structures

https://doi.org/10.1021/acs.chemrev.1c00845
Chem. Rev. 2022, 122, 9357−9394

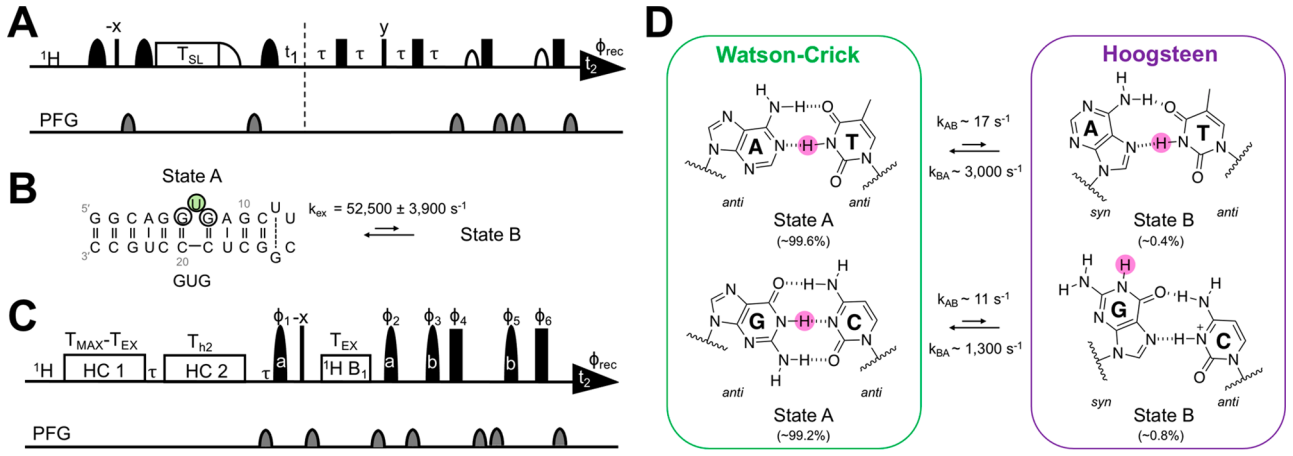

Figure 13. (A) Pulse scheme for ^{1}H $R_{1\rho}$ experiment on unlabeled RNA using a SELOPE readout.[252] (B) Secondary structure of the 25 nt GUG RNA. Nucleotides that were found to be in exchange are circled, and representative exchange parameters for U7−H6 (shaded green) are shown. (C) Pulse scheme for ^{1}H CEST experiment on unlabeled RNA again with a SELOPE readout.[253] (D) Equilibrium between Watson−Crick and Hoogsteen A:T and G:C base pairs is depicted. Exchange rates and populations are shown based on previous reports,[237] and reporter imino protons are shaded red. Additional details can be found in the original works.[252,253]

(Figure 11B).[282] Moreover, these states also undergo very similar dynamic motions across a wide range of time scales, as determined from ^{13}C spin relaxation rates and residual dipolar couplings (RDCs).[250] However, functional assays indicate that transcription activation is fluoride-dependent and kinetically driven.[282,283] What is more, mutational studies suggest that a prefolded "holo-like" apo state lowers the kinetic barrier for ligand binding, enabling efficient fluoride sensing to activate transcription below or near the toxicity threshold. Until recently, the mechanism by which this holo-like apo state achieves the "transcription−off" state remained unknown.[250]

To shed light on this mechanism, ^{13}C CEST experiments were implemented on uniformly ^{13}C/^{15}N-GTP- and uniformly ^{13}C/^{15}N -ATP/UTP labeled aptamer RNA. For the holo state, CEST profiles consistently showed a single, highly populated conformation (i.e., state A).[250] A subset of CEST profiles of the apo state, on the other hand, revealed the presence of conformational exchange to a transient state (i.e., state B).[250] The nucleotides that undergo chemical exchange were localized to the junction of P3, J13, J23, and the 3′-tail, suggesting a concerted transition (Figure 11A,B). A global fit of the CEST data determined the population (p_B = 1.4 ± 0.1%) and lifetime (τ_B = 3.2 ± 0.3 ms) of the holo-like conformation of the apo state. This fleeting process differentiates the apo and holo states. Rapid transition to the holo-like conformation of the apo state, which unlocks the highly conserved reverse Hoogsteen base pair located at the interface between the aptamer domain and the expression platform, promotes strand invasion and provides a path to transcription termination (Figure 11C).[250] Conversely, fluoride binding allosterically suppresses access to the holo-like conformation of the apo state, ensuring continued gene transcription.[250]

RNA can also regulate the initial steps of translational silencing. This process begins when a mature miRNA binds to the human Argonaute (Ago2) protein to form the RNA-induced silencing complex (RISC).[284] Here, translational silencing is predominantly controlled by base pair complementarity between the "seed" region of the miRNA and the target mRNA.[284−289] Interestingly, data from bioinformatics,[290] structural,[291] and mutational[292] studies all suggest that RNA dynamics within the central bulge of miRNA−mRNA duplex likely controls mRNA fate. To test this hypothesis, Petzold and co-workers used $R_{1\rho}$ experiments coupled with molecular dynamics simulations to investigate the structural dynamics of the interaction between miR-34a and its miRNA recognition element in the 3′-UTR of silent information regulator 1 mRNA (mSirt1) (Figure 12A).[247] Using these experiments, the authors detected chemical exchange in nucleotides surrounding the central bulge of the miR-34a−mSirt1 duplex (Figure 12A).[247] In this structural rearrangement, the gG8:tC17 base pair ('g' refers to the guide miRNA and 't' refers to the target mRNA) interconverts from a highly populated (i.e., state A) to a transient (i.e., state B) conformation. A global fit of the $R_{1\rho}$ data determined the exchange rate (k_{ex} = 1008 ± 12 s^{-1}) and population (p_B = 0.9 ± 0.2%) of the unfavorable state (Figure 12B),[247] and the chemical shift data[247] from ^{1}H ($\Delta\omega$ −2.20 ± 0.02 ppm) and ^{15}N ($\Delta\omega$ −3.8 ± 0.1 ppm) $R_{1\rho}$ experiments suggest formation of a gG8:tU21 wobble pair (Figure 12B),[247] a motif seen in other miRNAs.[293,294] Taken together, the miR-34a−mSirt1 binding site is in equilibrium between a highly populated 7-mer-A1 and a transient 8-mer-GU (Figure 12B).

Next, Petzold and co-workers sought to investigate the functional relevance of the 8-mer-GU unfavorable state using a functional assay and simulated complexes of human Ago with 7-mer-A1 and 8-mer-GU 34a−mSirt1 duplexes. Interestingly, the switch to the 8-mer-GU state causes coaxial stacking of the seed and supplementary helix fitting into Ago2, reminiscent of an active state in prokaryotic Ago.[295,296] Moreover, this state enhances repression of the target mRNA, revealing the importance of this dynamic miRNA−mRNA structure (Figure 12C).

4.2.3.2. CEST and $R_{1\rho}$ Experiments in Unlabeled RNA. After highlighting RD experiments in selectively and uniformly labeled RNA, we will conclude this section with a brief description of two pulse schemes that permit $R_{1\rho}$[252] and CEST[253] experiments in unlabeled RNA. In the first, Petzold and co-workers developed a SELOPE homonuclear NMR method by combining the selective excitation of specific groups of protons and reduction of spectral crowding using coherence transfer among scalar coupled protons. These coherence transfers take advantage of uniform homonuclear three bond

https://doi.org/10.1021/acs.chemrev.1c00845
Chem. Rev. 2022, 122, 9357−9394

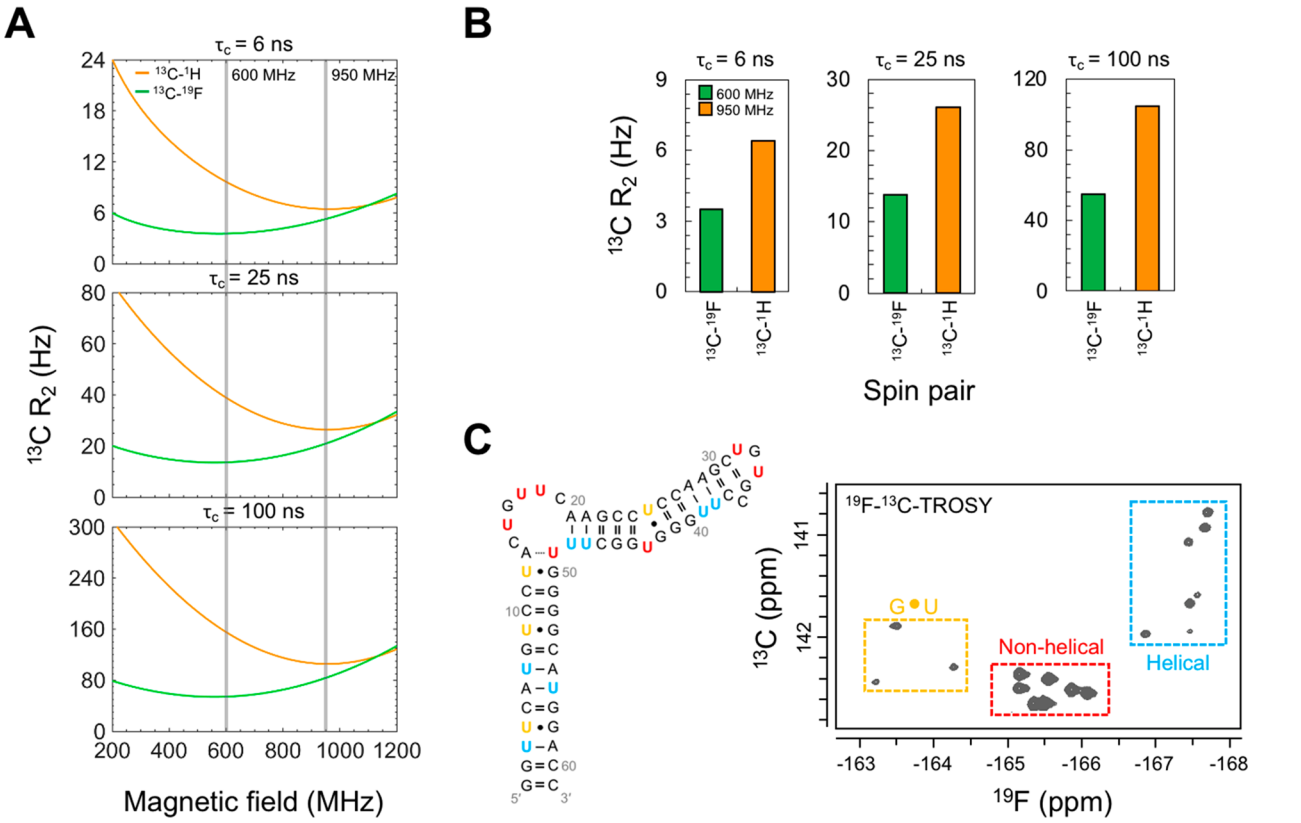

Figure 14. (A) Simulated ^{13}C R_2 rates (linewidths) at various magnetic fields in RNAs of various molecular weights (as measured by τ_C) to compare the relative TROSY effects of $^{13}C-^{1}H$ or $^{13}C-^{19}F$ spin pairs, which are shown on the left. (B) Same simulated rates as in A for each spin pair but only at the magnetic fields corresponding to the narrowest linewidths (smallest R_2) (600 and 950 MHz for $^{13}C-^{19}F$ or $^{13}C-^{1}H$, respectively, as shown by the gray lines in panel A).[18] (B) Representative $^{19}F-^{13}C$ TROSY spectrum to highlight the dispersion of resonances based on secondary structure (i.e., G:U wobble base pairs, nonhelical nucleotides, and helical A:U base pairs). Spectral regions are colored to match the respective uridines on the corresponding RNA. Additional details can be found in the original works.[18,57]

scalar coupling between H5 and H6 for pyrimidine bases ($^{3}J_{H5H6} \sim 8-10$ Hz) or between H1' and H2' for ribose in C2'-endo conformation ($^{3}J_{H1'H2'} \sim 8$Hz). Taken together, SELOPE permits well-resolved 1D and 2D spectra of unlabeled RNA. To demonstrate the utility of this method to probe RNA transient states, Petzold and co-workers adapted the SELOPE pulse scheme to include a spinlock (Figure 13A).[252] As proof-of-concept, this new ^{1}H $R_{1\rho}$ SELOPE experiment was used to detect chemical exchange in the central bulge region of the GUG RNA (Figure 13B).[252] Importantly, this method enables the use of lower spinlock strengths to measure slower exchange time scales.[252]

Building on this work, Al-Hashimi and co-workers introduced a high-power ^{1}H CEST SELOPE experiment to target imino protons (Figure 13C).[253] To showcase the utility of this method, Watson–Crick to Hoogsteen exchange of G:C and A:T base pairs in DNA were monitored (Figure 13D).[253] Importantly, Al-Hashimi and co-workers showed that short relaxation delays could be used to characterize fast exchange events that effectively minimize NOE effects that complicate ^{1}H RD experiments.[214,253,297−302] Moreover, their approach also takes advantage of high-power RF fields recently shown to extend the time scale sensitivity of CEST to include faster exchange processes that were traditionally only detectable by $R_{1\rho}$.[253,303] While both of these exciting new advancements hold promise, they are inherently limited to small RNAs. However, RNA biology is increasingly moving toward larger and larger RNAs. This important topic will be the focus of the next section.

5. EXPLORING LARGE MOLECULAR WEIGHT NUCLEIC ACIDS

Until now, most studies of RNA dynamics have focused on relatively small systems. However, RNA structural biology is increasingly moving toward larger RNAs, especially as cryo-EM advances in resolution and popularity.[304−306] Solution NMR spectroscopy, unlike X-ray crystallography and cryo-EM, is the only biophysical technique capable of probing nucleic acid conformational dynamics on a wide range of time scales in a physiologically relevant environment. Moreover, four technological advances have expanded the types of problems that NMR can tackle in studies of molecular nanomachines on the order of 1 MDa: (1) commercial availability of high-field magnets, up to 1.2 GHz ^{1}H Larmor frequency (28.2 T),[307] (2) specialized probes (e.g., cryo-probes) that minimize noise associated with the NMR signals,[308] (3) new isotope labeling technologies (described in Section 3), and (4) the design of new NMR experiments that are tailored to the isotope labeling used (described in Section 4). Our final section will describe how new labeling efforts can be leveraged to study large RNAs by NMR.

Taking inspiration from protein labeling,[309] our group installed ^{19}F directly next to a ^{13}C spin in UTP (Scheme 2)[18,86] and showed that, compared to the $^{13}C-^{1}H$ spin pair, $^{13}C-^{19}F$ had better sensitivity, ~6-times wider chemical shift

https://doi.org/10.1021/acs.chemrev.1c00845
Chem. Rev. 2022, 122, 9357−9394

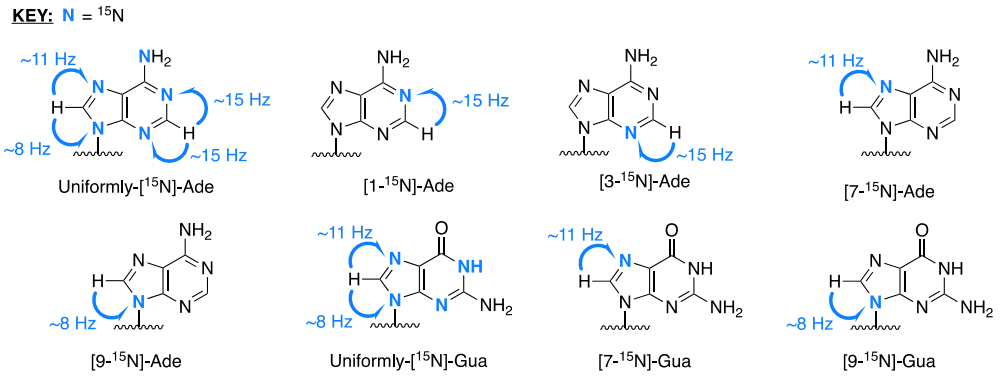

Figure 15. Examples of possible routes for coherence transfer between two-bond scalar couplings between Ade−H2-N1 and Ade−H2-N3 ($^2J_{H2N1} \approx 15$ Hz[29]), Pur−H8-N7 ($^2J_{H8N7} \approx 11$ Hz[29]) and Pur−H8-N9 ($^2J_{H8N9} \approx 8$ Hz[29]) in uniformly and selectively labeled RNA.

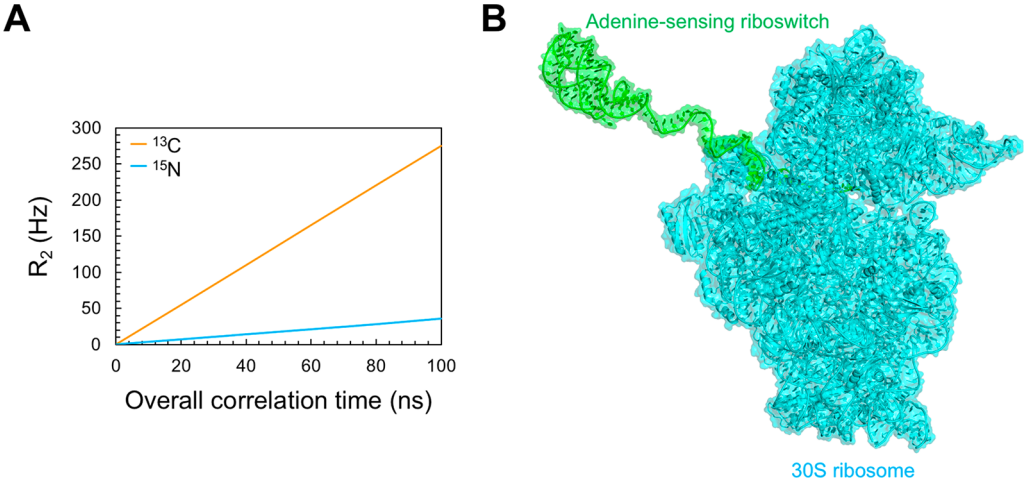

Figure 16. (A) Simulated TROSY-detected R_2 rates (linewidths) for ^{13}C and ^{15}N nuclei at 800 MHz. The ^{15}N nuclei has significantly narrower linewidths (smaller R_2) than that of ^{13}C. (B) Structural model of the >800 kDa complex of adenine-sensing riboswitch bound to the 30S ribosomal complex (structural model built from PDB IDs 1Y26 and 5MLN).[154] Additional details can be found in the original work.[154]

dispersion and ∼2-times more favorable relaxation properties in 2D TROSY experiments (Figure 14A,B).[18] Importantly, the high sensitivity of the ^{19}F nucleus enabled clear delineation of helical and nonhelical regions as well as G:U wobble and Watson−Crick base pairs (Figure 14C).[18,57] In parallel, the Kreutz group incorporated ^{13}C−^{19}F into both cytidine and uridine 2′-O-*t*BDMS amidites (Schemes 21 and 22) to show the same effect in RNAs made by solid-phase synthesis.[57] These findings suggest that structural insights are possible even in the absence of complete resonance assignment, which is a substantial bottleneck for large RNAs. Moreover, these labeling schemes can be readily adapted to exploit ^{19}F CEST and $R_{1\rho}$ experiments, which have been described for proteins up to 360 kDa.[310−315]

An alternative approach to heteronuclear correlation experiments that include nuclei with large CSAs such as ^{13}C and ^{19}F, which broaden the lines of nearby protons, was recently described by Bax and Summers and co-workers.[53] This approach capitalizes on the favorable relaxation properties of ^{15}N nuclei within RNA nucleobases. Here, they employed ^{1}H−^{15}N heteronuclear multiple quantum coherence (HMQC) experiments to measure ^{15}N $R_{1\rho}$ rates and RDCs in a large 232 nt (∼78 kDa) RNA by selectively transferring magnetization from Ade-H2 to Ade-N1/N3 via the two-bond scalar coupling ($^2J_{HN} \approx 15$ Hz[29]) (Figure 15). Extending this method in the same 232 nt RNA, Marchant and Tjandra and co-workers measured pseudocontact shifts using the two-bond scalar coupling of Ade-H8-N7 ($^2J_{H8N7} \approx 11$ Hz[29]) and Ade-H8-N9 ($^2J_{H8N9} \approx 8$ Hz) for coherence transfer.[316] Importantly, both experiments would benefit by atom-specific labeling. That is, selective ^{15}N labeling of Ade-N1 or Ade-N3 (described in Section 3.1.2.2) (Schemes 7 and 8) would reduce crowding considerably and direct magnetization transfer uniquely from Ade-H2 rather than splitting it between both sites, as in uniformly ^{15}N-labeled RNA (Figure 15). In the same way, selective ^{15}N labeling of Pur-N7 or Pur-N9 (described in Section 3.1.2.2) (Schemes 9−11) would again reduce crowding and direct coherence transfer uniquely from Pur-H8 (Figure 15). However, selective pulses can be deployed to affect the same decrowding and directed transfer. These labeling topologies could then be leveraged to probe two-bond ^{15}N CEST in large RNAs, as recently described by Zhang and co-workers.[232]

Our final example of harnessing the versatility of the ^{15}N nuclei is one that exploits the narrow linewidths in ^{1}H−^{15}N TROSY experiments compared to its ^{1}H−^{13}C counterpart (Figure 16A). Here, Fürtig and Schwalbe and co-workers investigated several reconstituted complexes between an adenine-sensing riboswitch and the 30S ribosome by NMR spectroscopy.[154] In particular, they implemented the ^{1}H−^{15}N BEST-TROSY pulse scheme[317,318] to obtain incredible spectra for a massive-sized complex (>800 kDa) (Figure 16B). Taken

https://doi.org/10.1021/acs.chemrev.1c00845
Chem. Rev. 2022, 122, 9357−9394

together, Fürtig and Schwalbe and co-workers succeed in illuminating the dynamic network that links the riboswitch RNA regulator, adenine ligand inducer, and ribosome protein S1 modulator during translation initiation.[154]

6. CONCLUSION

In humans, RNA transcripts exceed the number of proteins decoded by more than 50-fold, and yet the number of RNA structures remains below 1%, preventing a detailed understanding of RNA function (Figure 1). It is therefore essential to characterize RNA structural dynamics and interactions at atomic resolution to fill this critical knowledge gap. Over the past two decades, NMR spectroscopy has assumed a central role in RNA structure determination and probing dynamics on functionally relevant time scales in solution. In this review, we have summarized some of the many contributions of solution NMR studies to our knowledge of RNA structure, dynamics, and interactions, as facilitated by isotope labeling. We have presented a detailed overview of the prominent role stable isotopes continue to play in NMR analysis of nucleic acids (Section 2), how to synthesize these labels and introduce them into RNA (Section 3), and how these labels benefit NMR analysis. Of great interest, selective isotope labeling alleviates spectral crowding and removes dipolar and scalar couplings to simplify NMR dynamics measurements and data interpretation (Section 4). Moreover, recent advances in labeling open the door to study large RNA systems in a manner previously thought impossible (Section 5). As new orthogonal technologies are developed to better characterize the functional relevance of RNA, their structural dynamics will become increasingly important to better understand the cellular basis of RNA-based dysfunction that leads to various diseases. We anticipate that several imminent breakthrough technologies, some described herein, will enable NMR spectroscopy to continue to play a pivotal role in shining light on the structure, dynamics, and function of the important "dark matter of the genome", RNA *in vitro*, *in cellulo*, and *in vivo*.

AUTHOR INFORMATION

Corresponding Author

Theodore K. Dayie − *Department of Chemistry and Biochemistry, University of Maryland, College Park, Maryland 20742, United States;* orcid.org/0000-0002-7119-4362; Phone: 301-405-3165; Email: dayie@umd.edu

Authors

Lukasz T. Olenginski − *Department of Chemistry and Biochemistry, University of Maryland, College Park, Maryland 20742, United States*

Kehinde M. Taiwo − *Department of Chemistry and Biochemistry, University of Maryland, College Park, Maryland 20742, United States*

Complete contact information is available at: https://pubs.acs.org/10.1021/acs.chemrev.1c00845

Notes

The authors declare no competing financial interest.

Biographies

Theodore K. Dayie obtained his International Baccalaureate from the United World Colleges of the Atlantic (Llantwit Major, Wales), his Bachelor of Arts in Physics (Hamilton College, NY), and studied biophysics at Harvard University and obtained his PhD in 1996 with Gerhard Wagner. He was a Jane Coffin Childs postdoctoral fellow with Jamie Williamson at the Massachusetts Institute of Technology from 1996−1998, and then at The Scripps Research Institute (TSRI) from 1998−2000. After work at TSRI, he became an assistant researcher at the Lerner Research Institute of the Cleveland Clinic from 2000−2008. In 2008, he accepted an offer to become an associate professor at the University of Maryland, College Park. He is currently a full professor in the Department of Chemistry and Biochemistry with research focused on NMR spectroscopy of RNA molecules and their complexes. His group continues to make contributions to NMR studies of RNA structure, dynamics, and interactions.

Lukasz T. Olenginski graduated *Phi Beta Kappa* from Franklin and Marshall (F&M) College with degrees in Biochemistry and Molecular Biology and Applied Mathematics in 2015. At F&M, he worked under the dual mentorship of Christine Phillips-Piro and Scott Brewer to investigate the biophysical properties of unnatural amino acid-harboring proteins. After F&M, Lukasz spent the next two years working under Peggy Hsieh at the National Institutes of Health to expand his interests into the molecular and cellular fields by characterizing the mitotic roles of nuclear membrane proteins. Returning to the biophysical side, he joined the group of Theodore K. Dayie in 2018. Since then, he has dived head-first into the RNA-world, balancing his time between the development of new RNA labeling strategies and probing the conformational dynamics of viral RNAs.

Kehinde M. Taiwo earned a Biochemistry degree from Bowen University in Nigeria in 2011. She then went on to earn a Master's degree in Clinical Neuropsychiatry from the University of Birmingham in the United Kingdom in 2013 and another Master's degree in Biochemistry from California State University, Long Beach (CSULB) in 2017. While at CSULB, she received the Maria Erlinda Co Sarna Scholarship for prospects in research. In 2018, she joined the group of Theodore K. Dayie and has been involved in biophysical research using NMR and other techniques to probe the structures and conformational dynamics of RNAs to understand their functions as well as to develop RNA-based therapeutics. She is a member of the National Organization for the Professional Advancement of Black Chemists and Chemical Engineers (NOBCChE).

ACKNOWLEDGMENTS

T.K.D. acknowledges support from NIH (U54AI50470) and NSF (1808705 and DBI1040158). The authors would like to thank Hashim Al-Hashimi (Duke University), Jeffery Davis (University of Maryland, College Park), Christoph Kreutz (University of Innsbruk, Austria), and Lyle Isaacs (University of Maryland, College Park) for helpful discussions. The authors extend a special thanks to Christoph Kreutz for an ongoing collaboration.

ABBREVIATIONS

ABR = 1-*O*-acetyl-2,3,5-tri-*O*-benzoyl-α-D-ribofuranoside
Ac = acetyl
Ac_2O = acetic anhydride
Ade = adenine
Ago2 = Argonaute 2
AICA = 5-aminoimidazole-4-carboxamide
amidites = phosphoramidites
APRT = adenine phosphoribosyltransferase

https://doi.org/10.1021/acs.chemrev.1c00845
Chem. Rev. 2022, 122, 9357−9394

ATBR = 1′-*O*-acetyl-(2′,3′,5′-*O*-tribenzoyl)-β-D-ribofuranose
ATP = adenosine 5′-triphosphate
B_0 = reference magnetic field strength
B_1 = radio frequency field applied during RD or CEST
Bz = benzoyl
$(CH_3)_2C(OCH_3)_2$ = dimethoxypropane
C_2H_5OH = ethanol
C_2H_5ONa = sodium ethoxide
CH_3NH_2 = methylamine
CDI = 1,1′-carbonyldiimidazole
CEM = 2-cyanoethoxymethyl
CEP-Cl = 2-cyanoethyl *N*,*N*-diisopropylchlorophosphoramidite
CEST = chemical exchange saturation transfer
CIL = Cambridge Isotope Laboratories
CK = creatine kinase
cmo^5U = 5-oxyacetic acid
CPMG = Carr−Purcell−Meiboom−Gill
Cryo-EM = cryo-electron microscopy
CS = conformational selection
CTP = cytidine 5′-triphosphate
CTPS = CTP synthase
Cyt = cytosine
DEMA = diethoxymethyl acetate
DiPEA = *N*,*N*-diisopropylethylamine
DMAP = *N*-dimethyl aminopyridine
DMF = dimethylformamide
DMT = 4,4′-dimethoxytrityl
DMT-Cl = 4,4′-dimethoxytrityl chloride
dsRNA = double-stranded RNA
DSS = sodium-3-(trimethylsilyl)1-propanesulfonate
D*t*BS = di-*tert*-butylsilyl bis(trifluoromethanesulfonate)
EDC = *N*-ethyl-*N*′-(3-dimethyl aminopropyl) carbodiimide
GK = guanylate kinase
GND = phosphogluconate dehydrogenase
GTP = guanosine 5′-triphosphate
Gua = guanine
H_2SO_4 = sulfuric acid
$HC(OC_2H_5)_3$ = triethyl orthoformate
HCOOH = formic acid
$HCOONH_2$ = formamide
HF = hydrogen fluoride
HMQC = heteronuclear multiple quantum coherence
hNOE = heteronuclear Overhauser effect
HXK = hexokinase
iBu = isobutyryl
IF = induced fit
KCN = potassium cyanide
k_{AB} = forward reaction rate
k_{BA} = reverse reaction rate
k_{ex} = exchange rate
MK = myokinase
mRNA = messenger RNA
MS = mass spectrometry
ms = millisecond
mSirt1 = silent information regulator 1 mRNA
m^6A = N^6-methyladenine
Na_2CO_3 = sodium carbonate
$NaNO_2$ = sodium nitrite
$Na_2S_2O_4$ = sodium dithionite
NaOD = sodium deuteroxide
NaOH = sodium hydroxide
NDB = nucleic acid database
NH_3 = ammonia
NH_4Cl = ammonium chloride
$NH_4{}^{15}NO_2$ = ^{15}N-labeled ammonium nitrate
NH_4OH = ammonium hydroxide
NMPK = nucleoside-monophosphate kinase
NMR = nuclear magnetic resonance
N,*N*-DMA = *N*,*N*-dimethylaniline
NPE = nitrophenyl ethanol
ns = nanosecond
nt = nucleotide
OH = hydroxyl
p_A = population of state A
p_B = population of state B
PDB = protein data bank
$Pd/BaSO_4$ = palladium catalyst
PNPase = purine nucleoside phosphorylase
$POCl_3$ = phosphorus oxychloride
PRPPS = phosphoribosylpyrophosphate synthetase
ps = picosecond
pTSA = para toluene sulfonic acid
Pur = purine
PYKF = pyruvate kinase
Pyr = pyrimidine
RD = relaxation dispersion
RDC = residual dipolar coupling
R_{ex} = chemical exchange contribution to R_2
RF = radiofrequency
RISC = RNA-induced silencing complex
RK = ribokinase
rNTPs = ribonucleoside 5′-triphosphates
RPI1 = ribose-5-phosphate isomerase 1
rSAP = recombinant shrimp alkaline phosphatase
R_1 = longitudinal relaxation rate
$R_{1\rho}$ = rotating-frame transverse relaxation rate
R_2 = transverse relaxation rate
S = order parameter
SELOPE = selective optimized proton experiment
SO_2Cl_2 = sulfuryl chloride
SQ = single quantum
ssRNA = single-stranded RNA
*t*BDMS = 2′-O-*tert*-butyldimethylsilyl
TC = temperature compensation
TEA = triethylamine
TiBSC = 2,4,6-triisopropylbenzenesulfonyl chloride
TiPCEP = 2-cyanoethyl N,N,N′,N′-tetraisopropylphosphorodiamidite
TOM = 2′-O-[(triisopropylsilyl)oxy]methyl
TROSY = transverse relaxation optimized spectroscopy
T_1 = longitudinal relaxation time
T_2 = transverse relaxation time
UMPK = uridine monophosphate kinase
UPRT = uracil phosphoribosyltransferase
Ura = uracil
UTP = uridine 5′-triphosphate
XGPRT = xanthine-guanine phosphoribosyltransferase
ZWF = glucose-6-phosphate dehydrogenase
αR1P = α-D-ribofuranose 1-phosphate
$\Delta\omega$ = chemical shift difference
ω = Larmor frequency
τ_C = overall correlation time
τ_{ex} = exchange lifetime
μs = microsecond

https://doi.org/10.1021/acs.chemrev.1c00845
Chem. Rev. 2022, 122, 9357−9394

1D = one-dimensional
2D = two-dimensional
5FU = [5-^{13}C, 5-^{19}F, 6-^{2}H]-uracil

REFERENCES

(1) Crick, F. Central Dogma of Molecular Biology. *Nature* **1970**, *227*, 561−563.
(2) Cech, T. R.; Steitz, J. A. The Noncoding RNA Revolution-Trashing Old Rules to Forge New Ones. *Cell* **2014**, *157*, 77−94.
(3) Zhang, N. N.; Li, X. F.; Deng, Y. Q.; Zhao, H.; Huang, Y. J.; Yang, G.; Huang, W. J.; Gao, P.; Zhou, C.; Zhang, R. R.; et al. Thermostable mRNA Vaccine Against COVID-19. *Cell* **2020**, *182*, 1271−1283.
(4) Ho, W.; Gao, M.; Li, F.; Li, Z.; Zhang, X. Q.; Xu, X. Next-Generation Vaccines: Nanoparticle-Mediated DNA and mRNA Delivery. *Adv. Healthc. Mater.* **2021**, *10*, No. e2001812.
(5) Sandbrink, J. B.; Shattock, R. J. RNA Vaccines: A Suitable Platform for Tackling Emerging Pandemics? *Front. Immunol.* **2020**, *11*, 608460.
(6) Turner, J. S.; O'Halloran, J. A.; Kalaidina, E.; Kim, W.; Schmitz, A. J.; Zhou, J. Q.; Lei, T.; Thapa, M.; Chen, R. E.; Case, J. B.; et al. SARS-CoV-2 mRNA Vaccines Induce Persistent Human Germinal Centre Responses. *Nature* **2021**, *596*, 109−113.
(7) Corbett, K. S.; Edwards, D. K.; Leist, S. R.; Abiona, O. M.; Boyoglu-Barnum, S.; Gillespie, R. A.; Himansu, S.; Schäfer, A.; Ziwawo, C. T.; DiPiazza, A. T.; et al. SARS-CoV-2 mRNA Vaccine Design Enabled by Prototype Pathogen Preparedness. *Nature* **2020**, *586*, 567−571.
(8) Jackson, L. A.; Anderson, E. J.; Rouphael, N. G.; Roberts, P. C.; Makhene, M.; Coler, R. N.; McCullough, M. P.; Chappell, J. D.; Denison, M. R.; Stevens, L. J.; et al. An mRNA Vaccine against SARS-CoV-2 — Preliminary Report. *N. Engl. J. Med.* **2020**, *383*, 1920−1931.
(9) Mulligan, M. J.; Lyke, K. E.; Kitchin, N.; Absalon, J.; Gurtman, A.; Lockhart, S.; Neuzil, K.; Raabe, V.; Bailey, R.; Swanson, K. A.; et al. Phase I/II Study of COVID-19 RNA Vaccine BNT162b1 in Adults. *Nature* **2020**, *586*, 589−593.
(10) Ban, N.; Nissen, P.; Hansen, J.; Moore, P. B.; Steitz, T. A. The Complete Atomic Structure of the Large Ribosomal Subunit at 2.4 Å Resolution. *Science* **2000**, *289*, 905−920.
(11) Jobe, A.; Liu, Z.; Gutierrez-Vargas, C.; Frank, J. New Insights into Ribosome Structure and Function. *Cold Spring Harb. Perspect. Biol.* **2019**, *11*, No. a032615.
(12) Lawson, M. R.; Lessen, L. N.; Wang, J.; Prabhakar, A.; Corsepius, N. C.; Green, R.; Puglisi, J. D. Mechanisms That Ensure Speed and Fidelity in Eukaryotic Translation Termination. *Science* **2021**, *373*, 876−882.
(13) Hang, J.; Wan, R.; Yan, C.; Shi, Y. Structural Basis of Pre-mRNA Splicing. *Science* **2015**, *349*, 1191−1198.
(14) Wilkinson, M. E.; Charenton, C.; Nagai, K. RNA Splicing by the Spliceosome. *Annu. Rev. Biochem.* **2020**, *89*, 359−388.
(15) Wan, R.; Bai, R.; Zhan, X.; Shi, Y. How Is Precursor Messenger RNA Spliced by the Spliceosome? *Annu. Rev. Biochem.* **2020**, *89*, 333−358.
(16) Alexander, R. P.; Fang, G.; Rozowsky, J.; Snyder, M.; Gerstein, M. B. Annotating Non-Coding Regions of the Genome. *Nat. Rev. Genet.* **2010**, *11*, 559−571.
(17) Zhang, K.; Keane, S. C.; Su, Z.; Irobalieva, R. N.; Chen, M.; Van, V.; Sciandra, C. A.; Marchant, J.; Heng, X.; Schmid, M. F.; et al. Structure of the 30 KDa HIV-1 RNA Dimerization Signal by a Hybrid Cryo-EM, NMR and Molecular Dynamics Approach. *Structure* **2018**, *26*, 490−498.
(18) Becette, O. B.; Zong, G.; Chen, B.; Taiwo, K. M.; Case, D. A.; Dayie, T. K. Solution NMR Readily Reveals Distinct Structural Folds and Interactions in Doubly ^{13}C- and ^{19}F-Labeled RNAs. *Sci. Adv.* **2020**, *6*, No. eabc6572.
(19) Abulwerdi, F. A.; Xu, W.; Ageeli, A. A.; Yonkunas, M. J.; Arun, G.; Nam, H.; Schneekloth, J. S.; Dayie, T. K.; Spector, D.; Baird, N.; Le Grice, S. F. J. Selective Small-Molecule Targeting of a Triple Helix Encoded by the Long Noncoding RNA, MALAT1. *ACS Chem. Biol.* **2019**, *14*, 223−235.
(20) Lind, K. E.; Du, Z.; Fujinaga, K.; Peterlin, B. M.; James, T. L. Structure-Based Computational Database Screening, *In Vitro* Assay, and NMR Assessment of Compounds That Target TAR RNA. *Chem. Biol.* **2002**, *9*, 185−193.
(21) Johnson, E. C.; Feher, V. A.; Peng, J. W.; Moore, J. M.; Williamson, J. R. Application of NMR SHAPES Screening to an RNA Target. *J. Am. Chem. Soc.* **2003**, *125*, 15724−15725.
(22) Thompson, R. D.; Baisden, J. T.; Zhang, Q. NMR Characterization of RNA Small Molecule Interactions. *Methods* **2019**, *167*, 66−77.
(23) Binas, O.; Jesus, V. de; Landgraf, T.; Völklein, A. E.; Martins, J.; Hymon, D.; Bains, J. K.; Berg, H.; Biedenbänder, T.; Fürtig, B.; et al. ^{19}F NMR-Based Fragment Screening for 14 Different Biologically Active RNAs and 10 DNA and Protein Counter-Screens. *ChemBioChem.* **2021**, *22*, 423−433.
(24) LeBlanc, R. M.; Kasprzak, W. K.; Longhini, A. P.; Olenginski, L. T.; Abulwerdi, F.; Ginocchio, S.; Shields, B.; Nyman, J.; Svirydava, M.; Del Vecchio, C.; et al. Structural Insights of the Conserved "Priming Loop" of Hepatitis B Virus Pre-Genomic RNA. *J. Biomol. Struct. Dyn.* **2021**, 1−13.
(25) Wacker, A.; Weigand, J. E.; Akabayov, S. R.; Altincekic, N.; Bains, J. K.; Banijamali, E.; Binas, O.; Castillo-Martinez, J.; Cetiner, E.; Ceylan, B.; et al. Secondary Structure Determination of Conserved SARS-CoV-2 RNA Elements by NMR Spectroscopy. *Nucleic Acids Res.* **2020**, *48*, 12415−12435.
(26) Wilkinson, D. J. Historical and Contemporary Stable Isotope Tracer Approaches to Studying Mammalian Protein Metabolism. *Mass Spectrom. Rev.* **2018**, *37*, 57−80.
(27) Bernstein, M. A.; King, K. F.; Zhou, X. J. *Handbook of MRI Pulse Sequences*; Elsevier Inc., 2004.
(28) Harris, R. K.; Becker, E. D.; Cabral de Menezes, S. M.; Goodfellow, R.; Granger, P. NMR Nomenclature: Nuclear Spin Properties and Conventions for Chemical Shifts. IUPAC Recommendations 2001. International Union of Pure and Applied Chemistry. Physical Chemistry Division. Commission on Molecular Structure and Spectroscopy. *Magn. Reson. Chem.* **2002**, *40*, 489−505.
(29) Wijmenga, S. S.; van Buuren, B. N. M. The Use of NMR Methods for Conformational Studies of Nucleic Acids. *Prog. Nucl. Magn. Reson. Spectrosc.* **1998**, *32*, 287−387.
(30) Wang, Y.; Han, G.; Jiang, X.; Yuwen, T.; Xue, Y. Chemical Shift Prediction of RNA Imino Groups: Application toward Characterizing RNA Excited States. *Nat. Commun.* **2021**, *12*, 1595.
(31) Xue, Y.; Kellogg, D.; Kimsey, I. J.; Sathyamoorthy, B.; Stein, Z. W.; McBrairty, M.; Al-Hashimi, H. M. Characterizing RNA Excited States Using NMR Relaxation Dispersion. *Methods Enzymol.* **2015**, *558*, 39−73.
(32) Schnieders, R.; Keyhani, S.; Schwalbe, H.; Fürtig, B. More than Proton Detection—New Avenues for NMR Spectroscopy of RNA. *Chem.-Eur. J.* **2020**, *26*, 102−113.
(33) Schmidt, P. G.; Sierzputowska-Gracz, H.; Agris, P. F. Internal Motions in Yeast Phenylalanine Transfer RNA from ^{13}C NMR Relaxation Rates of Modified Base Methyl Groups: A Model-Free Approach. *Biochemistry* **1987**, *26*, 8529−8534.
(34) Oslen, J. I.; Schweizer, M. P.; Walkiw, I. J.; Hamill, W. D.; Horton, W. J.; Grant, D. M. Carbon-13 NMR Relaxation Studies of Pre-Melt Structural Dynamics in [4-^{13}C-Uracil] Labeled *E. Coli* Transfer RNA$_1^{Val}$*. *Nucleic Acids Res.* **1982**, *10*, 4449−4464.
(35) Shigeyuki, Y.; Usuki, K. M.; Ziro, Y.; Susumu, N.; Tatsuo, M. Tertiary Structures of Escherichia Coli tRNA as Studied by NMR Spectroscopy with ^{13}C-Labeling Method. *FEBS Lett.* **1980**, *119*, 77−80.
(36) Davis, D. R.; Yamaizumi, Z.; Nishimura, S.; Poulter, C. D. ^{15}N-labeled 5S RNA. Identification of uridine base pairs in *Escherichia coli* 5S RNA by ^{1}H-^{15}N multiple quantum NMR. *Biochemistry* **1989**, *28*, 4105−4108.
(37) Griffey, R. H.; Davis, D.; Yamaizumi, Z.; et al. ^{15}N-Labeled *Escherichia Coli* tRNA$_f^{Met}$, tRNA^{Glu}, tRNA^{Tyr}, and tRNA^{Phe}. Double

https://doi.org/10.1021/acs.chemrev.1c00845
Chem. Rev. 2022, 122, 9357−9394

Resonance and Two-Dimensional NMR of N1-Labeled Pseudouridine. *J. Biol. Chem.* **1985**, *260*, 9734−9741.
(38) Roy, S.; Papastavros, M. Z.; Redfield, A. G.; Sanchez, V. Nitrogen-15-Labeled Yeast $tRNA^{Phe}$: Double and Two-Dimensional Heteronuclear NMR of Guanosine and Uracil Ring NH Groups. *Biochemistry* **1984**, *23*, 4395−4400.
(39) Gewirth, D. T.; Abo, S. R.; Leontis, N. B.; Moore, P. B. Secondary Structure of 5S RNA: NMR Experiments on RNA Molecules Partially Labeled with Nitrogen-15. *Biochemistry* **1987**, *26*, 5213−5220.
(40) Torchia, D. A.; Sparks, S. W.; Bax, A. Staphylococcal Nuclease: Sequential Assignments and Solution Structure. *Biochemistry* **1989**, *28*, 5509−5524.
(41) LeMaster, D. M.; Richards, F. M. NMR Sequential Assignment of *Escherichia Coli* Thioredoxin Utilizing Random Fractional Deuteriation. *Biochemistry* **1988**, *27*, 142−150.
(42) Kime, M. J.; Moore, P. B. Escherichia Coli Ribosomal 5S RNA-Protein L25 Nucleoprotein Complex: Effects of RNA Binding on the Protein Structure and the Nature of the Interaction. *Biochemistry* **1984**, *23*, 1688−1695.
(43) Santoro, J.; King, G. C. A Constant-Time 2D Overbodenhausen Experiment for Inverse Correlation of Isotopically Enriched Species. *J. Magn. Reson.* **1992**, *97*, 202−207.
(44) Batey, R. T.; Inada, M.; Kujawinski, E.; Puglisi, J. D.; Williamson, J. R. Preparation of Isotopically Labeled Ribonucleotides for Multidimensional NMR Spectroscopy of RNA. *Nucleic Acids Res.* **1992**, *20*, 4515−4523.
(45) Nikonowicz, E. P.; Sirr, A.; Legault, P.; Jucker, F. M.; Baer, L. M.; Pardi, A. Preparation of ^{13}C and ^{15}N Labelled RNAs for Heteronuclear Multi-Dimensional NMR Studies. *Nucleic Acids Res.* **1992**, *20*, 4507−4513.
(46) Nikonowicz, E. P.; Pardi, A. Three-Dimensional Heteronuclear NMR Studies of RNA. *Nature* **1992**, *355*, 184−186.
(47) Nikonowicz, E. P.; Michnicka, M.; Kalurachchi, K.; Dejong, E. Preparation and Characterization of a Uniformly $^{2}H/^{15}N$-Labeled RNA Oligonucleotide for NMR Studies. *Nucleic Acids Res.* **1997**, *25*, 1390−1396.
(48) Földesi, A.; Trifonova, A.; Kundu, M. K.; Chattopadhyaya, J. The Synthesis of Deuterionucleosides. *Nucleosides, Nucleotides and Nucleic Acids* **2000**, *19*, 1615−1656.
(49) Sattler, M.; Fesik, S. W. Use of Deuterium Labeling in NMR: Overcoming a Sizeable Problem. *Structure* **1996**, *4*, 1245−1249.
(50) Kang, M.; Eichhorn, C. D.; Feigon, J. Structural Determinants for Ligand Capture by a Class II PreQ1 Riboswitch. *Proc. Natl. Acad. Sci. U. S. A.* **2014**, *111*, E663−E671.
(51) Boyd, P. S.; Brown, J. B.; Brown, J. D.; Catazaro, J.; Chaudry, I.; Ding, P.; Dong, X.; Marchant, J.; O'Hern, C. T.; Singh, K.; Swanson, C.; Summers, M. F.; Yasin, S. NMR Studies of Retroviral Genome Packaging. *Viruses* **2020**, *12*, 1115.
(52) Kotar, A.; Foley, H. N.; Baughman, K. M.; Keane, S. C. Advanced Approaches for Elucidating Structures of Large RNAs Using NMR Spectroscopy and Complementary Methods. *Methods* **2020**, *183*, 93−107.
(53) Marchant, J.; Bax, A.; Summers, M. F. Accurate Measurement of Residual Dipolar Couplings in Large RNAs by Variable Flip Angle NMR. *J. Am. Chem. Soc.* **2018**, *140*, 6978−6983.
(54) Keane, S. C.; Heng, X.; Lu, K.; Kharytonchyk, S.; Ramakrishnan, V.; Carter, G.; Barton, S.; Hosic, A.; Florwick, A.; Santos, J.; et al. Structure of the HIV-1 RNA Packaging Signal. *Science* **2015**, *348*, 917−921.
(55) D'Souza, V.; Dey, A.; Habib, D.; Summers, M. F. NMR Structure of the 101-Nucleotide Core Encapsidation Signal of the Moloney Murine Leukemia Virus. *J. Mol. Biol.* **2004**, *337*, 427−442.
(56) Rastinejad, F.; Evilia, C.; Lu, P. Studies of Nucleic Acids and Their Protein Interactions by ^{19}F NMR. *Methods Enzymol.* **1995**, *261*, 560−575.
(57) Nußbaumer, F.; Plangger, R.; Roeck, M.; Kreutz, C. Aromatic ^{19}F-^{13}C TROSY—[^{19}F, ^{13}C]-Pyrimidine Labeling for NMR Spectroscopy of RNA. *Angew. Chem., Int. Ed.* **2020**, *59*, 17062−17069.
(58) Scott, L. G.; Hennig, M. ^{19}F-Site-Specific-Labeled Nucleotides for Nucleic Acid Structural Analysis by NMR. *Methods Enzymol.* **2016**, *566*, 59−87.
(59) Huang, W.; Varani, G.; Drobny, G. P. $^{13}C/^{15}N$-^{19}F Intermolecular REDOR NMR Study of the Interaction of TAR RNA with Tat Peptides. *J. Am. Chem. Soc.* **2010**, *132*, 17643−17645.
(60) Kreutz, C.; Kählig, H.; Konrat, R.; Micura, R. A General Approach for the Identification of Site-Specific RNA Binders by ^{19}F NMR Spectroscopy: Proof of Concept. *Angew. Chem., Int. Ed.* **2006**, *45*, 3450−3453.
(61) Becette, O.; Olenginski, L. T.; Dayie, T. K. Solid-Phase Chemical Synthesis of Stable Isotope-Labeled RNA to Aid Structure and Dynamics Studies by NMR Spectroscopy. *Molecules* **2019**, *24*, 3476.
(62) Asadi-Atoi, P.; Barraud, P.; Tisne, C.; Kellner, S. Benefits of Stable Isotope Labeling in RNA Analysis. *Biol. Chem.* **2019**, *400*, 847−865.
(63) Dayie, K. T. Key Labeling Technologies to Tackle Sizeable Problems in RNA Structural Biology. *Int. J. Mol. Sci.* **2008**, *9*, 1214−1240.
(64) Lu, K.; Miyazaki, Y.; Summers, M. F. Isotope Labeling Strategies for NMR Studies of RNA. *J. Biomol. NMR* **2010**, *46*, 113−125.
(65) Scott, L. G.; Tolbert, T. J.; Williamson, J. R. Preparation of Specifically ^{2}H- and ^{13}C-Labeled Ribonucleotides. *Methods Enzymol.* **2000**, *317*, 18−38.
(66) Olenginski, L. T.; Taiwo, K. M.; LeBlanc, R. M.; Dayie, T. K. Isotope-Labeled RNA Building Blocks for NMR Structure and Dynamics Studies. *Molecules* **2021**, *26*, 5581.
(67) Marchanka, A.; Kreutz, C.; Carlomagno, T. Isotope Labeling for Studying RNA by Solid-State NMR Spectroscopy. *J. Biomol. NMR* **2018**, *71*, 151−164.
(68) Helmling, C.; Keyhani, S.; Sochor, F.; Fürtig, B.; Hengesbach, M.; Schwalbe, H. Rapid NMR Screening of RNA Secondary Structure and Binding. *J. Biomol. NMR* **2015**, *63*, 67−76.
(69) Milligan, J. F.; Uhlenbeck, O. C. Synthesis of Small RNAs Using T7 RNA Polymerase. *Methods Enzymol.* **1989**, *180*, 51−62.
(70) Milligan, J. F.; Groebe, D. R.; Witherell, G. W.; Uhlenbeck, O. C. Oligoribonucleotide Synthesis Using T7 RNA Polymerase and Synthetic DNA Templates. *Nucleic Acids Res.* **1987**, *15*, 8783−8798.
(71) SantaLucia, J., Jr; Shen, L. X.; Cai, Z.; Lewis, H.; Tinoco, I., Jr Synthesis and NMR of RNA with Selective Isotopic Enrichment in the Bases. *Nucleic Acids Res.* **1995**, *23*, 4913−4921.
(72) Schultheisz, H. L.; Szymczyna, B. R.; Scott, L. G.; Williamson, J. R. Enzymatic De Novo Pyrimidine Nucleotide Synthesis. *J. Am. Chem. Soc.* **2011**, *133*, 297−304.
(73) Schultheisz, H. L.; Szymczyna, B. R.; Scott, L. G.; Williamson, J. R. Pathway Engineered Enzymatic De Novo Purine Nucleotide Synthesis. *ACS Chem. Biol.* **2008**, *3*, 499−511.
(74) Alvarado, L. J.; LeBlanc, R. M.; Longhini, A. P.; Keane, S. C.; Jain, N.; Yildiz, Z. F.; Tolbert, B. S.; D'Souza, V. M.; Summers, M. F.; Kreutz, C.; et al. Regio-Selective Chemical-Enzymatic Synthesis of Pyrimidine Nucleotides Facilitates RNA Structure and Dynamics Studies. *Chembiochem* **2014**, *15*, 1573−1577.
(75) Longhini, A. P.; LeBlanc, R. M.; Becette, O.; Salguero, C.; Wunderlich, C. H.; Johnson, B. A.; D'Souza, V. M.; Kreutz, C.; Dayie, T. K. Chemo-Enzymatic Synthesis of Site-Specific Isotopically Labeled Nucleotides for Use in NMR Resonance Assignment, Dynamics and Structural Characterizations. *Nucleic Acids Res.* **2016**, *44*, No. e52.
(76) Kao, C.; Zheng, M.; Rüdisser, S. A Simple and Efficient Method to Reduce Nontemplated Nucleotide Addition at the 3′ Terminus of RNAs Transcribed by T7 RNA Polymerase. *RNA* **1999**, *5*, 1268−1272.
(77) Reese, C. B. The Chemical Synthesis of Oligo- and Poly-Ribonucleotides. *Nucleic Acids and Molecular Biology* **1989**, *3*, 164−181.
(78) Ogilvie, K. K.; Sadana, K. L.; Thompson, E. A.; Quilliam, M. A.; Westmore, J. B. The Use of Silyl Groups in Protecting the Hydroxyl

https://doi.org/10.1021/acs.chemrev.1c00845
Chem. Rev. 2022, 122, 9357−9394

Functions of Ribonucleosides. *Tetrahedron Lett.* **1974**, *15*, 2861−2863.
(79) Ogilvie, K. K.; Theriault, N.; Sadana, K. L. Synthesis of Oligoribonucleotides. *J. Am. Chem. Soc.* **1977**, *99*, 7741−7743.
(80) Beaucage, S. L.; Caruthers, M. H. Deoxynucleoside Phosphoramidites—A New Class of Key Intermediates for Deoxypolynucleotide Synthesis. *Tetrahedron Lett.* **1981**, *22*, 1859−1862.
(81) Roberts, J. L.; Poulter, C. D. 2′,3′,5′-Tri-*O*-Benzoyl[4-^{13}C]-Uridine. An Efficient, Regiospecific Synthesis of the Pyrimidine Ring. *J. Org. Chem.* **1978**, *43*, 1547−1550.
(82) Wunderlich, C. H.; Spitzer, R.; Santner, T.; Fauster, K.; Tollinger, M.; Kreutz, C. Synthesis of (6-^{13}C)Pyrimidine Nucleotides as Spin-Labels for RNA Dynamics. *J. Am. Chem. Soc.* **2012**, *134*, 7558−7569.
(83) Niu, C. H. Synthesis of [4-$^{15}NH_2$]- and [1,3-$^{15}N_2$]Cytidine Derivatives for Use in NMR-Monitored Binding Tests. *Anal. Biochem.* **1984**, *139*, 404−407.
(84) Davidson, D.; Baudisch, O. The Preparation of Uracil From Urea. *J. Am. Chem. Soc.* **1926**, *48*, 2379−2383.
(85) Juen, M. A.; Wunderlich, C. H.; Nußbaumer, F.; Tollinger, M.; Kontaxis, G.; Konrat, R.; Hansen, D. F.; Kreutz, C. Excited States of Nucleic Acids Probed by Proton Relaxation Dispersion NMR Spectroscopy. *Angew. Chem., Int. Ed.* **2016**, *55*, 12008−12012.
(86) Taiwo, K. M.; Becette, O. B.; Zong, G.; Chen, B.; Zavalij, P. Y.; Dayie, T. K. Chemo-Enzymatic Synthesis of ^{13}C- and ^{19}F-Labeled Uridine-5′-Triphosphate for RNA NMR Probing. *Monatsh. Chem.* **2021**, *152*, 441−447.
(87) Cushley, R. J.; Lipsky, S. R.; Fox, J. J. Reactions of 5-Fluorouracil Derivatives with Sodium Deuteroxide. *Tetrahedron Lett.* **1968**, *9*, 5393−5396.
(88) Hennig, M.; Munzarová, M. L.; Bermel, W.; Scott, L. G.; Sklenár, V.; Williamson, J. R. Measurement of Long Range ^{1}H-^{19}F Scalar Coupling Constants and Their Glycosidic Torsion Dependence in 5-Fluoropyrimidine-Substituted RNA. *J. Am. Chem. Soc.* **2006**, *128*, 5851−5858.
(89) Nußbaumer, F.; Juen, M. A.; Gasser, C.; Kremser, J.; Müller, T.; Tollinger, M.; Kreutz, C. Synthesis and Incorporation of ^{13}C-Labeled DNA Building Blocks to Probe Structural Dynamics of DNA by NMR. *Nucleic Acids Res.* **2017**, *45*, 9178−9192.
(90) Williamson, J. R.; Boxer, S. G. Synthesis of a Thymidine Phospboramidite Labelled with ^{13}C at C6: Relaxation Studies of the Loop Region in a ^{13}C Labelled DNA Hairpin. *Nucleic Acids Res.* **1988**, *16*, 1529−1540.
(91) Kremser, J.; Strebitzer, E.; Plangger, R.; Juen, M. A.; Nußbaumer, F.; Glasner, H.; Breuker, K.; Kreutz, C. Chemical Synthesis and NMR Spectroscopy of Long Stable Isotope Labelled RNA. *Chem. Commun.* **2017**, *53*, 12938−12941.
(92) Legault, P.; Pardi, A. In Situ Probing of Adenine Protonation in RNA by ^{13}C NMR. *J. Am. Chem. Soc.* **1994**, *116*, 8390−8391.
(93) Wolter, A. C.; Weickhmann, A. K.; Nasiri, A. H.; Hantke, K.; Ohlenschläger, O.; Wunderlich, C. H.; Kreutz, C.; Duchardt-Ferner, E.; Wöhnert, J. A Stably Protonated Adenine Nucleotide with a Highly Shifted pK_a Value Stabilizes the Tertiary Structure of a GTP-Binding RNA Aptamer. *Angew. Chem., Int. Ed.* **2017**, *56*, 401−404.
(94) Legault, P.; Pardi, A. Unusual Dynamics and pK_a Shift at the Active Site of a Lead-Dependent Ribozyme. *J. Am. Chem. Soc.* **1997**, *119*, 6621−6628.
(95) Thaplyal, P.; Bevilacqua, P. C. Experimental Approaches for Measuring pKa's in RNA and DNA. *Methods Enzymol.* **2014**, *549*, 189−219.
(96) Tang, C. L.; Alexov, E.; Pyle, A. M.; Honig, B. Calculation of pKas in RNA: On the Structural Origins and Functional Roles of Protonated Nucleotides. *J. Mol. Biol.* **2007**, *366*, 1475−1496.
(97) Veenis, A. J.; Li, P.; Soudackov, A. V.; Hammes-Schiffer, S.; Bevilacqua, P. C. Investigation of the pKa of the Nucleophilic O2′ of the Hairpin Ribozyme. *J. Phys. Chem. B* **2021**, *125*, 11869−11883.
(98) Abad, J. L.; Gaffney, B. L.; Jones, R. A. ^{15}N-Multilabeled Adenine and Guanine Nucleosides. Syntheses of [1,3,NH_2-$^{15}N_3$]- and [2-^{13}C-1,3,NH_2-$^{15}N_3$]-Labeled Adenosine, Guanosine, 2′-Deoxyadenosine, and 2′-Deoxyguanosine. *J. Org. Chem.* **1999**, *64*, 6575−6582.
(99) Ouwerkerk, N.; Van Boom, J.; Lugtenburg, J.; Raap, J. Synthesis of [1′,2′,5′,2-^{13}C $_4$]-2′-Deoxy-D-Adenosine by a Chemoenzymatic Strategy to Enable Labelling of Any of the 2^{15} Carbon-13 and Nitrogen-15 Isotopomers. *Eur. J. Org. Chem.* **2002**, *2002*, 2356−2362.
(100) Battaglia, U.; Long, J. E.; Searle, M. S.; Moody, C. J. 7-Deazapurine Biosynthesis: NMR Study of Toyocamycin Biosynthesis in Streptomyces Rimosus Using 2-^{13}C-7-^{15}N-Adenine. *Org. Biomol. Chem.* **2011**, *9*, 2227−2232.
(101) Sethi, S.; Gupta, S. P.; Jenkins, E. E.; Whitehead, C. W.; Townsend, L. B.; McCloskey, J. A. Mass Spectrometry of Nucleic Acid Constituents. Electron Ionization Spectra of Selectively Labeled Adenines. *J. Am. Chem. Soc.* **1982**, *104*, 3349−3353.
(102) Pagano, A. R.; Lajewski, W. M.; Jones, R. A. Syntheses of [6,7-^{15}N]-Adenosine, [6,7-^{15}N]-2′-Deoxyadenosine, and [7-^{15}N]-Hypoxanthine. *J. Am. Chem. Soc.* **1995**, *117*, 11669−11672.
(103) Bendich, A.; Russell, P. J., Jr; Fox, J. J. The Synthesis and Properties of 6-Chloropurine and Purine. *J. Am. Chem. Soc.* **1954**, *76*, 6073−6077.
(104) Olenginski, L. T.; Dayie, T. K. Chemo-Enzymatic Synthesis of [2-^{13}C, 7-^{15}N]-ATP for Facile NMR Analysis of RNA. *Monatsh. Chem.* **2020**, *151*, 1467−1473.
(105) Barrio, M. D. C. G.; Scopes, D. I. C.; Holtwick, J. B.; Leonard, N. J. Syntheses of All Singly Labeled [^{15}N]Adenines: Mass Spectral Fragmentation of Adenine. *Proc. Natl. Acad. Sci. U. S. A.* **1981**, *78*, 3986−3988.
(106) Lolli, M. L.; Medana, C.; Romagnano, S.; Castoldi, F.; Pozzoli, S.; Vago, F.; Fanelli, R.; Airoldi, L. Synthesis of Labelled [$^{15}N_3$]-6-Bromopurine, a Useful Precursor of ^{15}N-Labelled O^6-Alkylguanines, to be Used as Internal Standards for Quantitative GC-MS Analyses. *J. Label. Compd. and Radiopharm.* **1998**, *41*, 243−252.
(107) Zhao, H.; Pagano, A. R.; Wang, W.; Shallop, A.; Gaffney, B. L.; Jones, R. A. Use of a ^{13}C Atom To Differentiate Two ^{15}N-Labeled Nucleosides. Syntheses of [$^{15}NH_2$]-Adenosine, [1,NH_2-$^{15}N_2$]- and [2-^{13}C-1,NH_2-$^{15}N_2$]-Guanosine, and [1,7,NH_2-$^{15}N_3$]- and [2-^{13}C-1,7,NH_2-$^{15}N_3$]-2′-Deoxyguanosine. *J. Org. Chem.* **1997**, *62*, 7832−7835.
(108) Jain, M. L.; Tsao, Y. P.; Ho, N. L.; Cheng, J. W. A Facile Synthesis of [N1,NH_2-$^{15}N_2$]-, [N3,NH_2-$^{15}N_2$]-, and [N1,N3,NH_2-$^{15}N_3$]-Labeled Adenine. *J. Org. Chem.* **2001**, *66*, 6472−6475.
(109) Wachowius, F.; Höbartner, C. Chemical RNA Modifications for Studies of RNA Structure and Dynamics. *ChemBioChem.* **2010**, *11*, 469−480.
(110) Neuner, S.; Santner, T.; Kreutz, C.; Micura, R. The "Speedy" Synthesis of Atom-Specific ^{15}N Imino/Amido-Labeled RNA. *Chem.-Eur. J.* **2015**, *21*, 11634−11643.
(111) Neuner, S.; Kreutz, C.; Micura, R. The Synthesis of ^{15}N(7)-Hoogsteen Face-Labeled Adenosine Phosphoramidite for Solid-Phase RNA Synthesis. *Monatsh. Chem.* **2017**, *148*, 149−155.
(112) Santner, T.; Rieder, U.; Kreutz, C.; Micura, R. Pseudoknot Preorganization of the PreQ1 Class I Riboswitch. *J. Am. Chem. Soc.* **2012**, *134*, 11928−11931.
(113) Zhang, X.; Gaffney, B. L.; Jones, R. A. ^{15}N NMR of a Specifically Labeled RNA Fragment Containing Intrahelical GU Wobble Pairs. *J. Am. Chem. Soc.* **1997**, *119*, 6432−6433.
(114) Weissman, B. P.; Li, N. S.; York, D.; Harris, M.; Piccirilli, J. A. Heavy Atom Labeled Nucleotides for Measurement of Kinetic Isotope Effects. *Biochim. Biophys. Acta - Proteins Proteomics* **2015**, *1854*, 1737−1745.
(115) Lunn, F. A.; MacDonnell, J. E.; Bearne, S. L. Structural Requirements for the Activation of *Escherichia Coli* CTP Synthase by the Allosteric Effector GTP Are Stringent, but Requirements for Inhibition Are Lax. *J. Biol. Chem.* **2008**, *283*, 2010−2020.
(116) Taiwo, K. M.; Olenginski, L. T.; Nußbaumer, F.; Nam, H.; Hilber, S.; Kreutz, C.; Dayie, T. K. Synthesis of [7-^{15}N]-GTPs for RNA structure and dynamics by NMR spectroscopy. *Monatsh. Chem.* **2022**, DOI: 10.1007/s00706-022-02892-1.

(117) Masjost, B.; Ballmer, P.; Borroni, E.; Zürcher, G.; Winkler, F. K.; Jakon-Roetne, R.; Diederich, F. Structure-Based Design, Synthesis, and in vitro Evaluation of Bisubstrate Inhibitors for Catechol O-Methyltransferase (COMT). *Chem.-Eur. J.* **2000**, *6*, 971−982.
(118) Orji, C. C.; Kelly, J.; Ashburn, D. A.; Silks, L. A. First Synthesis of β-2′-Deoxy[9-^{15}N]Adenosine. *J. Chem. Soc. Perkin Trans. 1* **1996**, *7*, 595−597.
(119) Hoffman, D. W.; Holland, J. A. Preparation of Carbon-13 Labeled Ribonucleotides Using Acetate as an Isotope Source. *Nucleic Acids Res.* **1995**, *23*, 3361−3362.
(120) Thakur, C. S.; Dayie, T. K. Asymmetry of ^{13}C Labeled 3-Pyruvate Affords Improved Site Specific Labeling of RNA for NMR Spectroscopy. *J. Biomol. NMR* **2012**, *52*, 65−77.
(121) Thakur, C. S.; Luo, Y.; Chen, B.; Eldho, N. V.; Dayie, T. K. Biomass Production of Site Selective ^{13}C/^{15}N Nucleotides Using Wild Type and a Transketolase E. Coli Mutant for Labeling RNA for High Resolution NMR. *J. Biomol. NMR* **2012**, *52*, 103−114.
(122) Parkin, D. W.; Leung, H. B.; Schramm, V. L. Synthesis of Nucleotides with Specific Radiolabels in Ribose. Primary ^{14}C and Secondary ^{3}H Kinetic Isotope Effects on Acid-Catalyzed Glycosidic Bond Hydrolysis of AMP, DAMP, and Inosine. *J. Biol. Chem.* **1984**, *259*, 9411−9417.
(123) Gilles, A. M.; Cristea, I.; Palibroda, N.; Hilden, I.; Jensen, K. F.; Sarfati, R. S.; Namane, A.; Ughetto-Monfrin, J.; Bârzu, O. Chemienzymatic Synthesis of Uridine Nucleotides Labeled with [^{15}N] and [^{13}C]. *Anal. Biochem.* **1995**, *232*, 197−203.
(124) Rising, K. A.; Schramm, V. L. Enzymic Synthesis of NAD+ with the Specific Incorporation of Atomic Labels. *J. Am. Chem. Soc.* **1994**, *116*, 6531−6536.
(125) Parkin, D. W.; Schramm, V. L. Catalytic and Allosteric Mechanism of AMP Nucleosidase from Primary, β-Secondary, and Multiple Heavy Atom Kinetic Isotope Effects. *Biochemistry* **1987**, *26*, 913−920.
(126) Hennig, M.; Scott, L. G.; Sperling, E.; Bermel, W.; Williamson, J. R. Synthesis of 5-Fluoropyrimidine Nucleotides as Sensitive NMR Probes of RNA Structure. *J. Am. Chem. Soc.* **2007**, *129*, 14911−14921.
(127) Scott, L. G.; Geierstanger, B. H.; Williamson, J. R.; Hennig, M. Enzymatic Synthesis and ^{19}F NMR Studies of 2-Fluoroadenine-Substituted RNA. *J. Am. Chem. Soc.* **2004**, *126*, 11776−11777.
(128) Zhang, W.; Zhao, S.; Serianni, A. S. Labeling Monosaccharides With Stable Isotopes. *Methods Enzymol.* **2015**, *565*, 423−458.
(129) Arthur, P. K.; Alvarado, L. J.; Dayie, T. K. Expression, Purification and Analysis of the Activity of Enzymes from the Pentose Phosphate Pathway. *Protein Expr. Purif.* **2011**, *76*, 229−237.
(130) Zhang, W.; Turney, T.; Surjancev, I.; Serianni, A. S. Enzymatic Synthesis of Ribo- and 2′-Deoxyribonucleosides from Glycofuranosyl Phosphates: An Approach to Facilitate Isotopic Labeling. *Carbohydr. Res.* **2017**, *449*, 125−133.
(131) Hirschbein, B. L.; Mazenod, F. P.; Whitesides, G. M. Synthesis of Phosphoenolypyruvate and Its Use in ATP Cofactor Regeneration. *J. Org. Chem.* **1982**, *47*, 3765−3766.
(132) Simon, E. S.; Grabowski, S.; Whitesides, G. M. Convenient Syntheses of Cytidine 5′-Triphosphate, Guanosine 5′-Triphosphate, and Uridine 5′-Triphosphate and Their Use in the Preparation of UDP-Glucose, UDP-Glucuronic Acid, and GDP-Mannose. *J. Org. Chem.* **1990**, *55*, 1834−1841.
(133) Gross, A.; Abril, O.; Lewis, J. M.; Geresh, S.; Whitesides, G. M. Practical Synthesis of 5-Phospho-D-Ribosyl α-1-Pyrophosphate (PRPP): Enzymatic Routes from Ribose 5-Phosphate or Ribose. *J. Am. Chem. Soc.* **1983**, *105*, 7428−7435.
(134) Duker, J. M.; Serianni, A. S. (^{13}C)-Substituted Sucrose: ^{13}C-^{1}H and ^{13}C-^{13}C Spin Coupling Constants to Assess Furanose Ring and Glycosidic Bond Conformations in Aqueous Solution. *Carbohydr. Res.* **1993**, *249*, 281−303.
(135) Cook, G. P.; Greenberg, M. M. A General Synthesis of C2′-Deuterated Ribonucleosides. *J. Org. Chem.* **1994**, *59*, 4704−4706.
(136) Toyama, A.; Takino, Y.; Takeuchi, H.; Harada, I. Ultraviolet Resonance Raman Spectra of Ribosyl C(1′)-Deuterated Purine Nucleosides: Evidence of Vibrational Coupling between Purine and Ribose Rings. *J. Am. Chem. Soc.* **1993**, *115*, 11092−11098.
(137) Földesi, A.; Nilson, F. P. R.; Glemarec, C.; Gioeli, C.; Chattopadhyaya, J. Synthesis of 1′,2′,3′,4′,5′,5″-^{2}H$_6$-β-D-Ribonucleosides and 1′,2′,2″,3′,4′,5′,5″-^{2}H$_7$-β-D-2′-Deoxyribonucleosides for Selective Suppression of Proton Resonances in Partially-Deuterated Oligo-DNA, Oligo-RNA and in 2,5A Core (^{1}H-NMR Window). *Tetrahedron* **1992**, *48*, 9033−9072.
(138) Vorbrüggen, H.; Höfle, G. Nucleoside Syntheses, XXIII[1] On the Mechanism of Nucleoside Synthesis. *Chem. Ber.* **1981**, *114*, 1256−1268.
(139) Liu, Y.; Holmstrom, E.; Zhang, J.; Yu, P.; Wang, J.; Dyba, M. A.; Chen, D.; Ying, J.; Lockett, S.; Nesbitt, D. J.; et al. Synthesis and Applications of RNAs with Position-Selective Labelling and Mosaic Composition. *Nature* **2015**, *522*, 368−372.
(140) Liu, Y.; Holmstrom, E.; Yu, P.; Tan, K.; Zuo, X.; Nesbitt, D. J.; Sousa, R.; Stagno, J. R.; Wang, Y. X. Incorporation of Isotopic, Fluorescent, and Heavy-Atom-Modified Nucleotides into RNAs by Position-Selective Labeling of RNA. *Nat. Protoc.* **2018**, *13*, 987−1005.
(141) Liu, Y.; Yu, P.; Dyba, M.; Sousa, R.; Stagno, J. R.; Wang, Y. X. Applications of PLOR in Labeling Large RNAs at Specific Sites. *Methods* **2016**, *103*, 4−10.
(142) Keyhani, S.; Goldau, T.; Blümler, A.; Heckel, A.; Schwalbe, H. Chemo-Enzymatic Synthesis of Position-Specifically Modified RNA for Biophysical Studies Including Light Control and NMR Spectroscopy. *Angew. Chem., Int. Ed.* **2018**, *130*, 12193−12197.
(143) Blümler, A.; Schwalbe, H.; Heckel, A. Solid-Phase-Supported Chemoenzymatic Synthesis of a Light-Activatable tRNA Derivative. *Angew. Chem., Int. Ed.* **2022**, *61*, No. e202111613.
(144) Wunderlich, C. H.; Juen, M. A.; LeBlanc, R. M.; Longhini, A. P.; Dayie, T. K.; Kreutz, C. Stable Isotope-Labeled RNA Phosphoramidites to Facilitate Dynamics by NMR. *Methods Enzymol.* **2015**, *565*, 461−494.
(145) Chen, B.; Longhini, A. P.; Nußbaumer, F.; Kreutz, C.; Dinman, J. D.; Dayie, T. K. CCR5 RNA Pseudoknots: Residue and Site-Specific Labeling Correlate Internal Motions with MicroRNA Binding. *Chem.-Eur. J.* **2018**, *24*, 5462−5468.
(146) Shiba, Y.; Masuda, H.; Watanabe, N.; Ego, T.; Takagaki, K.; Ishiyama, K.; Ohgi, T.; Yano, J. Chemical Synthesis of a Very Long Oligoribonucleotide with 2-Cyanoethoxymethyl (CEM) as the 2′-*O*-Protecting Group: Structural Identification and Biological Activity of a Synthetic 110mer Precursor-MicroRNA Candidate. *Nucleic Acids Res.* **2007**, *35*, 3287−3296.
(147) Ohgi, T.; Kitagawa, H.; Yano, J. Chemical Synthesis of Oligoribonucleotides with 2′-*O*-(2-Cyanoethoxymethyl)-Protected Phosphoramidites. *Curr. Protoc. Nucleic Acid Chem.* **2008**, *34*, 2.15.1−2.15.19.
(148) Liu, B.; Shi, H.; Al-Hashimi, H. M. Developments in Solution-State NMR Yield Broader and Deeper Views of the Dynamic Ensembles of Nucleic Acids. *Curr. Opin. Struct. Biol.* **2021**, *70*, 16−25.
(149) Strebitzer, E.; Rangadurai, A.; Plangger, R.; Kremser, J.; Juen, M. A.; Tollinger, M.; Al-Hashimi, H. M.; Kreutz, C. 5-Oxyacetic Acid Modification Destabilizes Double Helical Stem Structures and Favors Anionic Watson-Crick like Cmo^{5}U-G Base Pairs. *Chem.-Eur. J.* **2018**, *24*, 18903−18906.
(150) Shi, H.; Liu, B.; Nussbaumer, F.; Rangadurai, A.; Kreutz, C.; Al-Hashimi, H. M. NMR Chemical Exchange Measurements Reveal That N^{6}-Methyladenosine Slows RNA Annealing. *J. Am. Chem. Soc.* **2019**, *141*, 19988−19993.
(151) Liu, B.; Shi, H.; Rangadurai, A.; Nussbaumer, F.; Chu, C. C.; Erharter, K. A.; Case, D. A.; Kreutz, C.; Al-Hashimi, H. M. A Quantitative Model Predicts How m^{6}A Reshapes the Kinetic Landscape of Nucleic Acid Hybridization and Conformational Transitions. *Nat. Commun.* **2021**, *12*, 5201.
(152) Desaulniers, J. P.; Chang, Y. C.; Aduri, R.; Abeysirigunawardena, S. C.; SantaLucia, J.; Chow, C. S. Pseudouridines in RRNA Helix 69 Play a Role in Loop Stacking Interactions. *Org. Biomol. Chem.* **2008**, *6*, 3892−3895.

https://doi.org/10.1021/acs.chemrev.1c00845
Chem. Rev. 2022, 122, 9357−9394

(153) Olenginski, L. T.; Becette, O. B.; Beaucage, S. L.; Dayie, T. K. Synthesis of Atom-Specific Nucleobase and Ribose Labeled Uridine Phosphoramidite for NMR Analysis of Large RNAs. *Monatsh. Chem.* **2021**, *152*, 1361−1367.
(154) de Jesus, V.; Qureshi, N. S.; Warhaut, S.; Bains, J. K.; Dietz, M. S.; Heilemann, M.; Schwalbe, H.; Fürtig, B. Switching at the Ribosome: Riboswitches Need rProteins as Modulators to Regulate Translation. *Nat. Commun.* **2021**, *12*, 4723.
(155) Komoroski, R. A.; Allerhand, A. Observation of Resonances from Some Minor Bases in the Natural-Abundance Carbon-13 Nuclear Magnetic Resonance Spectrum of Unfractionated Yeast Transfer Ribonucleic Acid. Evidence for Fast Internal Motion of the Dihydrouracil Rings. *Biochemistry* **1974**, *13*, 369−372.
(156) Nirmala, N. R.; Wagner, G. Measurement of ^{13}C Relaxation Times in Proteins by Two-Dimensional Heteronuclear ^{1}H-^{13}C Correlation Spectroscopy. *J. Am. Chem. Soc.* **1988**, *110*, 7557−7558.
(157) Sklenář, V. Í.; Torchia, D.; Bax, A. Measurement of Carbon-13 Longitudinal Relaxation Using ^{1}H Detection. *J. Magn. Reson.* **1987**, *73*, 375−379.
(158) Kay, L. E.; Jue, T. L.; Bangerter, B.; Demou, P. C. Sensitivity Enhancement of ^{13}C T1Measurements via Polarization Transfer. *J. Magn. Reson.* **1987**, *73*, 558−564.
(159) Farrow, N. A.; Muhandiram, R.; Singer, A. U.; Pascal, S. M.; Kay, C. M.; Gish, G.; Shoelson, S. E.; Pawson, T.; Forman-Kay, J. D.; Kay, L. E. Backbone Dynamics of a Free and a Phosphopeptide-Complexed Src Homology 2 Domain Studied by ^{15}N NMR Relaxation. *Biochemistry* **1994**, *33*, 5984−6003.
(160) Dayie, K. T.; Wagner, G. Relaxation-Rate Measurements for ^{15}N-^{1}H Groups with Pulsed-Field Gradients and Preservation of Coherence Pathways. *J. Magn. Reson.* **1994**, *111*, 121−126.
(161) Peng, J. W.; Wagner, G. Mapping of Spectral Density Functions Using Heteronuclear NMR Relaxation Measurements. *J. Magn. Reson.* **1992**, *98*, 308−332.
(162) Kay, L. E.; Torchia, D. A.; Bax, A. Backbone Dynamics of Proteins as Studied by ^{15}N Inverse Detected Heteronuclear NMR Spectroscopy: Application to Staphylococcal Nuclease. *Biochemistry* **1989**, *28*, 8972−8979.
(163) Dayie, K. T.; Brodsky, A. S.; Williamson, J. R. Base Flexibility in HIV-2 TAR RNA Mapped by Solution ^{15}N, ^{13}C NMR Relaxation. *J. Mol. Biol.* **2002**, *317*, 263−278.
(164) Hoogstraten, C. G.; Wank, J. R.; Pardi, A. Active Site Dynamics in the Lead-Dependent Ribozyme. *Biochemistry* **2000**, *39*, 9951−9958.
(165) Boisbouvier, J.; Brutscher, B.; Simorre, J.-P.; Marion, D. ^{13}C Spin Relaxation Measurements in RNA: Sensitivity and Resolution Improvement Using Spin-State Selective Correlation Experiments. *J. Biomol. NMR* **1999**, *14*, 241−252.
(166) Hall, K. B.; Tang, C. ^{13}C Relaxation and Dynamics of the Purine Bases in the Iron Element RNA Hairpin. *Biochemistry* **1998**, *37*, 9323−9332.
(167) Akke, M.; Fiala, R.; Jiang, F.; Patel, D.; Palmer III, A. G. Base Dynamics in a UUCG Tetraloop RNA Hairpin Characterized by ^{15}N Spin Relaxation: Correlations with Structure and Stability. *RNA* **1997**, *3*, 702−709.
(168) Rangadurai, A.; Szymaski, E. S.; Kimsey, I. J.; Shi, H.; Al-Hashimi, H. M. Characterizing Micro-to-Millisecond Chemical Exchange in Nucleic Acids Using Off-Resonance $R_{1\rho}$ Relaxation Dispersion. *Prog. Nucl. Magn. Reson. Spectrosc.* **2019**, *112*−*113*, 55−102.
(169) Marušič, M.; Schlagnitweit, J.; Petzold, K. RNA Dynamics by NMR Spectroscopy. *ChemBioChem.* **2019**, *20*, 2685−2710.
(170) Nozinovic, S.; Richter, C.; Rinnenthal, J.; Fürtig, B.; Duchardt-Ferner, E.; Weigand, J. E.; Schwalbe, H. Quantitative 2D and 3D Γ-HCP Experiments for the Determination of the Angles α and ζ in the Phosphodiester Backbone of Oligonucleotides. *J. Am. Chem. Soc.* **2010**, *132*, 10318−10329.
(171) Rinnenthal, J.; Richter, C.; Nozinovic, S.; Fürtig, B.; Lopez, J. J.; Glaubitz, C.; Schwalbe, H. RNA Phosphodiester Backbone Dynamics of a Perdeuterated CUUCGg Tetraloop RNA from Phosphorus-31 NMR Relaxation Analysis. *J. Biomol. NMR* **2009**, *45*, 143−155.
(172) Vallurupalli, P.; Kay, L. E. A Suite of ^{2}H NMR Spin Relaxation Experiments for the Measurement of RNA Dynamics. *J. Am. Chem. Soc.* **2005**, *127*, 6893−6901.
(173) Bothe, J. R.; Nikolova, E. N.; Eichhorn, C. D.; Chugh, J.; Hansen, A. L.; Al-Hashimi, H. M. Characterizing RNA Dynamics at Atomic Resolution Using Solution-State NMR Spectroscopy. *Nat. Methods* **2011**, *8*, 919−931.
(174) Al-Hashimi, H. M.; Walter, N. G. RNA Dynamics: It Is about Time. *Curr. Opin. Struct. Biol.* **2008**, *18*, 321−329.
(175) Peng, J. W. Cross-Correlated ^{19}F Relaxation Measurements for the Study of Fluorinated Ligand-Receptor Interactions. *J. Magn. Reson.* **2001**, *153*, 32−47.
(176) Palmer III, A. G. NMR Characterization of the Dynamics of Biomacromolecules. *Chem. Rev.* **2004**, *104*, 3623−3640.
(177) Ishima, R.; Torchia, D. A. Protein Dynamics from NMR. *Nat. Struct. Biol.* **2000**, *7*, 740−743.
(178) Fushman, D.; Cowburn, D. Nuclear Magnetic Resonance Relaxation in Determination of Residue-Specific ^{15}N Chemical Shift Tensors in Proteins in Solution: Protein Dynamics, Structure, and Applications of Transverse Relaxation Optimized Spectroscopy. *Methods Enzymol.* **2001**, *339*, 109−122.
(179) Dayie, K. T.; Wagner, G.; Lefevre, J. F. Theory and Practice of Nuclear Spin Relaxation In Proteins. *Annu. Rev. Phys. Chem.* **1996**, *47*, 243−282.
(180) Fushman, D.; Tjandra, N.; Cowburn, D. Measurement of ^{15}N Chemical Shift Anisotropy in Solution. *J. Am. Chem. Soc.* **1998**, *120*, 10947−10952.
(181) Ying, J.; Grishaev, A.; Bryce, D. L.; Bax, A. Chemical Shift Tensors of Protonated Base Carbons in Helical RNA and DNA from NMR Relaxation and Liquid Crystal Measurements. *J. Am. Chem. Soc.* **2006**, *128*, 11443−11454.
(182) Lipari, G.; Szabo, A. Model-Free Approach to the Interpretation of Nuclear Magnetic Resonance Relaxation in Macromolecules. 1. Theory and Range of Validity. *J. Am. Chem. Soc.* **1982**, *104*, 4546−4559.
(183) Lipari, G.; Szabo, A. Model-free approach to the interpretation of nuclear magnetic resonance relaxation in macromolecules. 2. Analysis of experimental results. *J. Am. Chem. Soc.* **1982**, *104*, 4559−4570.
(184) Shajani, Z.; Varani, G. ^{13}C NMR Relaxation Studies of RNA Base and Ribose Nuclei Reveal a Complex Pattern of Motions in the RNA Binding Site for Human U1A Protein. *J. Mol. Biol.* **2005**, *349*, 699−715.
(185) Shajani, Z.; Drobny, G.; Varani, G. Binding of U1A Protein Changes RNA Dynamics as Observed by ^{13}C NMR Relaxation Studies. *Biochemistry* **2007**, *46*, 5875−5883.
(186) Hansen, A. L.; Al-Hashimi, H. M. Dynamics of Large Elongated RNA by NMR Carbon Relaxation. *J. Am. Chem. Soc.* **2007**, *129*, 16072−16082.
(187) Blad, H.; Reiter, N. J.; Abildgaard, F.; Markley, J. L.; Butcher, S. E. Dynamics and Metal Ion Binding in the U6 RNA Intramolecular Stem-Loop as Analyzed by NMR. *J. Mol. Bio.* **2005**, *353*, 540−555.
(188) Nam, H.; Becette, O.; LeBlanc, R. M.; Oh, D.; Case, D. A.; Dayie, T. K. Deleterious Effects of Carbon-Carbon Dipolar Coupling on RNA NMR Dynamics. *J. Biomol. NMR* **2020**, *74*, 321−331.
(189) Olenginski, L. T.; Dayie, T. K. Quantifying the Effects of Long-Range ^{13}C-^{13}C Dipolar Coupling on Measured Relaxation Rates in RNA. *J. Biomol. NMR* **2021**, *75*, 203−211.
(190) Zhang, Q.; Sun, X.; Watt, E. D.; Al-Hashimi, H. M. Resolving the Motional Modes That Code for RNA Adaptation. *Science* **2006**, *311*, 653−656.
(191) Boisbouvier, J.; Wu, Z.; Ono, A.; Kainosho, M.; Bax, A. Rotational Diffusion Tensor of Nucleic Acids from ^{13}C NMR Relaxation. *J. Biomol. NMR* **2003**, *27*, 133−142.
(192) Johnson, J. E.; Julien, K. R.; Hoogstraten, C. G. Alternate-Site Isotopic Labeling of Ribonucleotides for NMR Studies of Ribose

https://doi.org/10.1021/acs.chemrev.1c00845
Chem. Rev. 2022, 122, 9357−9394

Conformational Dynamics in RNA. *J. Biomol. NMR* **2006**, *35*, 261−274.
(193) Yamazaki, T.; Muhandiram, R.; Kay, L. E. NMR Experiments for the Measurement of Carbon Relaxation Properties in Highly Enriched, Uniformly ^{13}C,^{15}N-Labeled Proteins: Application to $^{13}C^{\alpha}$ Carbons. *J. Am. Chem. Soc.* **1994**, *116*, 8266−8278.
(194) Johnson, J. E., Jr; Hoogstraten, C. G. Extensive Backbone Dynamics in the GCAA RNA Tetraloop Analyzed Using ^{13}C NMR Spin Relaxation and Specific Isotope Labeling. *J. Am. Chem. Soc.* **2008**, *130*, 16757−16769.
(195) Dayie, K. T.; Wagner, G. Carbonyl Carbon Probe of Local Mobility in ^{13}C,^{15}N-Enriched Proteins Using High-Resolution Nuclear Magnetic Resonance. *J. Am. Chem. Soc.* **1997**, *119*, 7797−7806.
(196) Lakomek, N. A.; Ying, J.; Bax, A. Measurement of ^{15}N relaxation rates in perdeuterated proteins by TROSY-based methods. *J. Biomol. NMR* **2012**, *53*, 209−221.
(197) Palmer III, A. G.; Cavanagh, J.; Wright, P. E.; Rance, M. Sensitivity Improvement in Proton-Detected Two-Dimensional Heteronuclear Correlation NMR Spectroscopy. *J. Magn. Reson.* **1991**, *93*, 151−170.
(198) Kay, L.; Keifer, P.; Saarinen, T. Pure Absorption Gradient Enhanced Heteronuclear Single Quantum Correlation Spectroscopy with Improved Sensitivity. *J. Am. Chem. Soc.* **1992**, *114*, 10663−10665.
(199) Palmer III, A. G.; Koss, H. Chemical Exchange. *Methods Enzymol.* **2019**, *615*, 177−236.
(200) Palmer, A. G.; Kroenke, C. D.; Loria, J. P. Nuclear Magnetic Resonance Methods for Quantifying Microsecond-to-Millisecond Motions in Biological Macromolecules. *Methods Enzymol.* **2001**, *339*, 204−238.
(201) Anthis, N. J.; Clore, G. M. Visualizing Transient Dark States by NMR Spectroscopy. *Q. Rev. Biophys.* **2015**, *48*, 35−116.
(202) Palmer III, A. G.; Grey, M. J.; Wang, C. Solution NMR Spin Relaxation Methods for Characterizing Chemical Exchange in High-Molecular-Weight Systems. *Methods Enzymol.* **2005**, *394*, 430−465.
(203) Palmer, A. G., III; Massi, F. Characterization of the Dynamics of Biomacromolecules Using Rotating-Frame Spin Relaxation NMR Spectroscopy. *Chem. Rev.* **2006**, *106*, 1700−1719.
(204) Peng, J. W.; Thanabal, V.; Wagner, G. H. 2D Heteronuclear NMR Measurements of Spin-Lattice Relaxation Times in the Rotating Frame of X Nuclei in Heteronuclear HX Spin Systems. *J. Magn. Reson.* **1991**, *94*, 82−100.
(205) Luz, Z.; Meiboom, S. Nuclear Magnetic Resonance Study of the Protolysis of Trimethylammonium Ion in Aqueous Solution—Order of the Reaction with Respect to Solvent. *J. Chem. Phys.* **1963**, *39*, 366−370.
(206) Meiboom, S.; Gill, D. Modified Spin-Echo Method for Measuring Nuclear Relaxation Times. *Rev. Sci. Instrum.* **1958**, *29*, 688−691.
(207) Carr, H. Y.; Purcell, E. M. Effects of Diffusion on Free Precession in Nuclear Magnetic Resonance Experiments. *Phys. Rev.* **1954**, *94*, 630−638.
(208) Vallurupalli, P.; Bouvignies, G.; Kay, L. E. Studying "Invisible" Excited Protein States in Slow Exchange with a Major State Conformation. *J. Am. Chem. Soc.* **2012**, *134*, 8148−8161.
(209) Schanda, P.; Brutscher, B. Very Fast Two-Dimensional NMR Spectroscopy for Real-Time Investigation of Dynamic Events in Proteins on the Time Scale of Seconds. *J. Am. Chem. Soc.* **2005**, *127*, 8014−8015.
(210) Carver, J. P.; Richards, R. E. A General Two-Site Solution for the Chemical Exchange Produced Dependence of T_2 upon the Carr-Purcell Pulse Separation. *J. Magn. Reson.* **1972**, *6*, 89−105.
(211) Strebitzer, E.; Nußbaumer, F.; Kremser, J.; Tollinger, M.; Kreutz, C. Studying Sparsely Populated Conformational States in RNA Combining Chemical Synthesis and Solution NMR Spectroscopy. *Methods* **2018**, *148*, 39−47.
(212) Zhao, B.; Hansen, A. L.; Zhang, Q. Characterizing Slow Chemical Exchange in Nucleic Acids by Carbon CEST and Low Spin-Lock Field $R_{1\rho}$ NMR Spectroscopy. *J. Am. Chem. Soc.* **2014**, *136*, 20−23.
(213) McConnell, H. M. Reaction Rates by Nuclear Magnetic Resonance. *J. Chem. Phys.* **1958**, *28*, 430−431.
(214) Bouvignies, G.; Kay, L. E. Measurement of Proton Chemical Shifts in Invisible States of Slowly Exchanging Protein Systems by Chemical Exchange Saturation Transfer. *J. Phys. Chem. B* **2012**, *116*, 14311−14317.
(215) Helgstrand, M.; Härd, T.; Allard, P. Simulations of NMR Pulse Sequences during Equilibrium and Non-Equilibrium Chemical Exchange. *J. Biomol. NMR* **2000**, *18*, 49−63.
(216) Korzhnev, D. M.; Orekhov, V. Y.; Kay, L. E. Off-Resonance $R_{1\rho}$ NMR Studies of Exchange Dynamics in Proteins with Low Spin-Lock Fields: An Application to a Fyn SH3 Domain. *J. Am. Chem. Soc.* **2005**, *127*, 713−721.
(217) Kimsey, I. J.; Szymanski, E. S.; Zahurancik, W. J.; Shakya, A.; Xue, Y.; Chu, C. C.; Sathyamoorthy, B.; Suo, Z.; Al-Hashimi, H. M. Dynamic Basis for dG-dT Misincorporation via Tautomerization and Ionization. *Nature* **2018**, *554*, 195−201.
(218) van de Ven, F. J. M.; Philippens, V. E. P. Optimization of Constant-Time Evolution in Multidimensional NMR Experiments. *J. Magn. Reson.* **1992**, *97*, 637−644.
(219) Grzesiek, S.; Bax, A. Improved 3D Triple-Resonance NMR Techniques Applied to a 31 KDa Protein. *J. Magn. Reson.* **1992**, *96*, 432−440.
(220) Bax, A.; Freeman, R. Investigation of Complex Networks of Spin-Spin Coupling by Two-Dimensional NMR. *J. Magn. Reson.* **1981**, *44*, 542−561.
(221) Bax, A.; Mehlkopf, A. F.; Smidt, J. Homonuclear Broadband-Decoupled Absorption Spectra, with Linewidths Which Are Independent of the Transverse Relaxation Rate. *J. Magn. Reson.* **1979**, *35*, 167−169.
(222) Dayie, K. T. Resolution Enhanced Homonuclear Carbon Decoupled Triple Resonance Experiments for Unambiguous RNA Structural Characterization. *J. Biomol. NMR* **2005**, *32*, 129−139.
(223) Brutscher, B.; Boisbouvier, J.; Kupče, E.; Tisné, C.; Dardel, F.; Marion, D.; Simorre, J.-P. Base-Type-Selective High-Resolution ^{13}C Edited NOESY for Sequential Assignment of Large RNAs. *J. Biomol. NMR* **2001**, *19*, 141−151.
(224) Kupče, E.; Wagner, G. Multisite Band-Selective Decoupling in Proteins. *J. Magn. Reson.* **1996**, *110*, 309−312.
(225) Ferrage, F.; Eykyn, T. R.; Bodenhausen, G. Frequency-Switched Single-Transition Cross-Polarization: A Tool for Selective Experiments in Biomolecular NMR. *ChemPhysChem* **2004**, *5*, 76−84.
(226) Pelupessy, P.; Chiarparin, E.; Bodenhausen, G. Excitation of Selected Proton Signals in NMR of Isotopically Labeled Macromolecules. *J. Magn. Reson.* **1999**, *138*, 178−181.
(227) Chiarparin, E.; Pelupessy, P.; Bodenhausen, G. Selective Cross-Polarization in Solution State NMR. *Mol. Phys.* **1998**, *95*, 759−767.
(228) LeBlanc, R. M.; Longhini, A. P.; Tugarinov, V.; Dayie, T. K. NMR Probing of Invisible Excited States Using Selectively Labeled RNAs. *J. Biomol. NMR* **2018**, *71*, 165−172.
(229) Vallurupalli, P.; Scott, L.; Williamson, J. R.; Kay, L. E. Strong Coupling Effects during X-Pulse CPMG Experiments Recorded on Heteronuclear ABX Spin Systems: Artifacts and a Simple Solution. *J. Biomol. NMR* **2007**, *38*, 41−46.
(230) Zhou, Y.; Yang, D. $^{13}C_{\alpha}$ CEST Experiment on Uniformly ^{13}C-Labeled Proteins. *J. Biomol. NMR* **2015**, *61*, 89−94.
(231) Zhou, Y.; Yang, D. Effects of J Couplings and Unobservable Minor States on Kinetics Parameters Extracted from CEST Data. *J. Magn. Reson.* **2014**, *249*, 118−125.
(232) Zhao, B.; Baisden, J. T.; Zhang, Q. Probing Excited Conformational States of Nucleic Acids by Nitrogen CEST NMR Spectroscopy. *J. Magn. Reson.* **2020**, *310*, 106642.
(233) Rangadurai, A.; Kremser, J.; Shi, H.; Kreutz, C.; Al-Hashimi, H. M. Direct Evidence for (G)O6···H 2-N4(C) + Hydrogen Bonding in Transient G(Syn)-C + and G(Syn)-m 5 C + Hoogsteen Base Pairs in Duplex DNA from Cytosine Amino Nitrogen off-Resonance $R_{1\rho}$

https://doi.org/10.1021/acs.chemrev.1c00845
Chem. Rev. 2022, 122, 9357−9394

Relaxation Dispersion Measurements. *J. Magn. Reson.* **2019**, *308*, 106589.
(234) Chen, B.; LeBlanc, R.; Dayie, T. K. SAM-II Riboswitch Samples at Least Two Conformations in Solution in the Absence of Ligand: Implications for Recognition. *Angew. Chem., Int. Ed.* **2016**, *55*, 2724−2727.
(235) Kloiber, K.; Spitzer, R.; Tollinger, M.; Konrat, R.; Kreutz, C. Probing RNA Dynamics via Longitudinal Exchange and CPMG Relaxation Dispersion NMR Spectroscopy Using a Sensitive ^{13}C-Methyl Label. *Nucleic Acids Res.* **2011**, *39*, 4340−4351.
(236) Hansen, A. L.; Nikolova, E. N.; Casiano-Negroni, A.; Al-Hashimi, H. M. Extending the Range of Microsecond-to-Millisecond Chemical Exchange Detected in Labeled and Unlabeled Nucleic Acids by Selective Carbon $R_{1\rho}$ NMR Spectroscopy. *J. Am. Chem. Soc.* **2009**, *131*, 3818−3819.
(237) Alvey, H. S.; Gottardo, F. L.; Nikolova, E. N.; Al-Hashimi, H. M. Widespread Transient Hoogsteen Base Pairs in Canonical Duplex DNA with Variable Energetics. *Nat. Commun.* **2014**, *5*, 4786.
(238) Kimsey, I. J.; Petzold, K.; Sathyamoorthy, B.; Stein, Z. W.; Al-Hashimi, H. M. Visualizing Transient Watson-Crick-like Mispairs in DNA and RNA Duplexes. *Nature* **2015**, *519*, 315−320.
(239) Xue, Y.; Gracia, B.; Herschlag, D.; Russell, R.; Al-Hashimi, H. M. Visualizing the Formation of an RNA Folding Intermediate Through a Fast Highly Modular Secondary Structure Switch. *Nat. Commun.* **2016**, *7*, No. ncomms11768.
(240) Rangadurai, A.; Szymanski, E. S.; Kimsey, I.; Shi, H.; Al-Hashimi, H. M. Probing Conformational Transitions Towards Mutagenic Watson-Crick-like G·T Mismatches Using Off-Resonance Sugar Carbon $R_{1\rho}$ Relaxation Dispersion. *J. Biomol. NMR* **2020**, *74*, 457−471.
(241) Merriman, D. K.; Xue, Y.; Yang, S.; Kimsey, I. J.; Shakya, A.; Clay, M.; Al-Hashimi, H. M. Shortening the HIV-1 TAR RNA Bulge by a Single Nucleotide Preserves Motional Modes Over a Broad Range of Time Scales. *Biochemistry* **2016**, *55*, 4445−4456.
(242) Szymanski, E. S.; Kimsey, I. J.; Al-Hashimi, H. M. Direct NMR Evidence That Transient Tautomeric and Anionic States in dG·dT Form Watson-Crick-like Base Pairs. *J. Am. Chem. Soc.* **2017**, *139*, 4326−4329.
(243) Clay, M. C.; Ganser, L. R.; Merriman, D. K.; Al-Hashimi, H. M. Resolving Sugar Puckers in RNA Excited States Exposes Slow Modes of Repuckering Dynamics. *Nucleic Acids Res.* **2017**, *45*, No. e134.
(244) Shi, H.; Clay, M. C.; Rangadurai, A.; Sathyamoorthy, B.; Case, D. A.; Al-Hashimi, H. M. Atomic Structures of Excited State A-T Hoogsteen Base Pairs in Duplex DNA by Combining NMR Relaxation Dispersion, Mutagenesis, and Chemical Shift Calculations. *J. Biomol. NMR* **2018**, *70*, 229−244.
(245) Lee, J.; Dethoff, E. A.; Al-Hashimi, H. M. Invisible RNA State Dynamically Couples Distant Motifs. *Proc. Natl. Acad. Sci. U. S. A.* **2014**, *111*, 9485−9490.
(246) Bothe, J. R.; Stein, Z. W.; Al-Hashimi, H. M. Evaluating the Uncertainty in Exchange Parameters Determined from Off-Resonance $R_{1\rho}$ Relaxation Dispersion for Systems in Fast Exchange. *J. Magn. Reson.* **2014**, *244*, 18−29.
(247) Baronti, L.; Guzzetti, I.; Ebrahimi, P.; Friebe Sandoz, S.; Steiner, E.; Schlagnitweit, J.; Fromm, B.; Silva, L.; Fontana, C.; Chen, A. A.; et al. Base-Pair Conformational Switch Modulates miR-34a Targeting of Sirt1 mRNA. *Nature* **2020**, *583*, 139−144.
(248) Steiner, E.; Schlagnitweit, J.; Lundström, P.; Petzold, K. Capturing Excited States in the Fast-Intermediate Exchange Limit in Biological Systems Using ^{1}H NMR Spectroscopy. *Angew. Chem., Int. Ed.* **2016**, *128*, 16101−16104.
(249) Baisden, J. T.; Boyer, J. A.; Zhao, B.; Hammond, S. M.; Zhang, Q. Visualizing a Protonated RNA State That Modulates MicroRNA-21 Maturation. *Nat. Chem. Biol.* **2021**, *17*, 80−88.
(250) Zhao, B.; Guffy, S. L.; Williams, B.; Zhang, Q. An Excited State Underlies Gene Regulation of a Transcriptional Riboswitch. *Nat. Chem. Biol.* **2017**, *13*, 968−974.
(251) Zhao, B.; Zhang, Q. Measuring Residual Dipolar Couplings in Excited Conformational States of Nucleic Acids by CEST NMR Spectroscopy. *J. Am. Chem. Soc.* **2015**, *137*, 13480−13483.
(252) Schlagnitweit, J.; Steiner, E.; Karlsson, H.; Petzold, K. Efficient Detection of Structure and Dynamics in Unlabeled RNAs: The SELOPE Approach. *Chem.-Eur. J.* **2018**, *24*, 6067−6070.
(253) Liu, B.; Rangadurai, A.; Shi, H.; Al-Hashimi, H. M. Rapid Assessment of Watson-Crick to Hoogsteen Exchange in Unlabeled DNA Duplexes Using High-Power SELOPE Imino ^{1}H CEST. *Magn. Reson.* **2021**, *2*, 715−731.
(254) Otten, R.; Villali, J.; Kern, D.; Mulder, F. A. A. Probing Microsecond Time Scale Dynamics in Proteins by Methyl ^{1}H Carr-Purcell-Meiboom-Gill Relaxation Dispersion NMR Measurements. Application to Activation of the Signaling Protein NtrC^{r}. *J. Am. Chem. Soc.* **2010**, *132*, 17004−17014.
(255) Hansen, A. L.; Lundström, P.; Velyvis, A.; Kay, L. E. Quantifying Millisecond Exchange Dynamics in Proteins by CPMG Relaxation Dispersion NMR Using Side-Chain ^{1}H Probes. *J. Am. Chem. Soc.* **2012**, *134*, 3178−3189.
(256) Dethoff, E. A.; Petzold, K.; Chugh, J.; Casiano-Negroni, A.; Al-Hashimi, H. M. Visualizing Transient Low-Populated Structures of RNA. *Nature* **2012**, *491*, 724−728.
(257) Miclet, E.; Williams, D. C.; Clore, G. M.; Bryce, D. L.; Boisbouvier, J.; Bax, A. Relaxation-Optimized NMR Spectroscopy of Methylene Groups in Proteins and Nucleic Acids. *J. Am. Chem. Soc.* **2004**, *126*, 10560−10570.
(258) Abou Assi, H.; Rangadurai, A. K.; Shi, H.; Liu, B.; Clay, M. C.; Erharter, K.; Kreutz, C.; Holley, C. L.; Al-Hashimi, H. M. 2′-*O*-Methylation Can Increase the Abundance and Lifetime of Alternative RNA Conformational States. *Nucleic Acids Res.* **2020**, *48*, 12365−12379.
(259) Vaidyanathan, P. P.; AlSadhan, I.; Merriman, D. K.; Al-Hashimi, H.; Herschlag, D. Pseudouridine and N^{6}-Methyladenosine Modifications Weaken PUF Protein/RNA Interactions. *RNA* **2017**, *23*, 611−618.
(260) Liu, B.; Merriman, D. K.; Choi, S. H.; Schumacher, M. A.; Plangger, R.; Kreutz, C.; Horner, S. M.; Meyer, K. D.; Al-Hashimi, H. M. A Potentially Abundant Junctional RNA Motif Stabilized by m^{6}A and Mg^{2+}. *Nat. Commun.* **2018**, *9*, 2761.
(261) Chu, C.-C.; Liu, B.; Plangger, R.; Kreutz, C.; Al-Hashimi, H. M. m^{6}A Minimally Impacts the Structure, Dynamics, and Rev ARM Binding Properties of HIV-1 RRE Stem IIB. *PLoS One* **2019**, *14*, No. e0224850.
(262) Zaccara, S.; Ries, R. J.; Jaffrey, S. R. Reading, Writing and Erasing mRNA Methylation. *Nat. Rev. Mol. Cell Biol.* **2019**, *20*, 608−624.
(263) Roundtree, I. A.; Evans, M. E.; Pan, T.; He, C. Dynamic RNA Modifications in Gene Expression Regulation. *Cell* **2017**, *169*, 1187−1200.
(264) Fu, Y.; Dominissini, D.; Rechavi, G.; He, C. Gene Expression Regulation Mediated through Reversible m^{6}A RNA Methylation. *Nat. Rev. Genet.* **2014**, *15*, 293−306.
(265) Kim, G. W.; Siddiqui, A. N^{6}-Methyladenosine Modification of HCV RNA Genome Regulates Cap-Independent IRES-Mediated Translation via YTHDC2 Recognition. *Proc. Natl. Acad. Sci. U. S. A.* **2021**, *118*, No. e2022024118.
(266) Kim, G. W.; Siddiqui, A. Hepatitis B Virus X Protein Recruits Methyltransferases to Affect Cotranscriptional N^{6}-Methyladenosine Modification of Viral/Host RNAs. *Proc. Natl. Acad. Sci. U. S. A.* **2021**, *118*, No. e2019455118.
(267) Imam, H.; Khan, M.; Gokhale, N. S.; McIntyre, A. B.; Kim, G. W.; Jang, J. Y.; Kim, S. J.; Mason, C. E.; Horner, S. M.; Siddiqui, A. N^{6}-Methyladenosine Modification of Hepatitis B Virus RNA Differentially Regulates the Viral Life Cycle. *Proc. Natl. Acad. Sci. U. S. A.* **2018**, *115*, 8829−8834.
(268) Hesser, C. R.; Karijolich, J.; Dominissini, D.; He, C.; Glaunsinger, B. A. N^{6}-Methyladenosine Modification and the YTHDF2 Reader Protein Play Cell Type Specific Roles in Lytic

https://doi.org/10.1021/acs.chemrev.1c00845
Chem. Rev. 2022, 122, 9357−9394

Viral Gene Expression During Kaposi's Sarcoma-Associated Herpesvirus Infection. *PLoS Pathog.* **2018**, *14*, No. e1006995.
(269) Tirumuru, N.; Zhao, B. S.; Lu, W.; Lu, Z.; He, C.; Wu, L. N^6-Methyladenosine of HIV-1 RNA Regulates Viral Infection and HIV-1 Gag Protein Expression. *Elife* **2016**, *5*, No. e15528.
(270) Lichinchi, G.; Zhao, B. S.; Wu, Y.; Lu, Z.; Qin, Y.; He, C.; Rana, T. M. Dynamics of Human and Viral RNA Methylation During Zika Virus Infection. *Cell Host Microbe* **2016**, *20*, 666−673.
(271) Gokhale, N. S.; McIntyre, A. B. R.; McFadden, M. J.; Roder, A. E.; Kennedy, E. M.; Gandara, J. A.; Hopcraft, S. E.; Quicke, K. M.; Vazquez, C.; Willer, J.; et al. *N6*-Methyladenosine in *Flaviviridae* Viral RNA Genomes Regulates Infection. *Cell Host Microbe* **2016**, *20*, 654−665.
(272) Zhao, X.; Yang, Y.; Sun, B.-F.; Shi, Y.; Yang, X.; Xiao, W.; Hao, Y.-J.; Ping, X.-L.; Chen, Y.-S.; Wang, W.-J.; et al. FTO-Dependent Demethylation of N6-Methyladenosine Regulates mRNA Splicing and is Required for Adipogenesis. *Cell Res.* **2014**, *24*, 1403−1419.
(273) Wang, X.; Lu, Z.; Gomez, A.; Hon, G. C.; Yue, Y.; Han, D.; Fu, Y.; Parisien, M.; Dai, Q.; Jia, G.; et al. N^6-Methyladenosine-Dependent Regulation of Messenger RNA Stability. *Nature* **2014**, *505*, 117−120.
(274) Xiao, W.; Adhikari, S.; Dahal, U.; Chen, Y. S.; Hao, Y. J.; Sun, B. F.; Sun, H. Y.; Li, A.; Ping, X. L.; Lai, W. Y.; et al. Nuclear m^6A Reader YTHDC1 Regulates mRNA Splicing. *Mol. Cell* **2016**, *61*, 507−519.
(275) Weng, Y.-L.; Wang, X.; An, R.; Cassin, J.; Vissers, C.; Liu, Y.; Liu, Y.; Xu, T.; Wang, X.; Wong, S. Z. H.; et al. Epitranscriptomic m^6A Regulation of Axon Regeneration in the Adult Mammalian Nervous System. *Neuron* **2018**, *97*, 313−325.
(276) Tawa, K.; Knoll, W. Mismatching Base-pair Dependence of the Kinetics of DNA-DNA Hybridization Studied by Surface Plasmon Fluorescence Spectroscopy. *Nucleic Acids Res.* **2004**, *32*, 2372−2377.
(277) Xu, S.; Zhan, J.; Man, B.; Jiang, S.; Yue, W.; Gao, S.; Guo, C.; Liu, H.; Li, Z.; Wang, J.; Zhou, Y. Real-Time Reliable Determination of Binding Kinetics of DNA Hybridization Using a Multi-Channel Graphene Biosensor. *Nat. Commun.* **2017**, *8*, 14902.
(278) Cisse, I. I.; Kim, H.; Ha, T. A Rule of Seven in Watson-Crick Base Pairing of Mismatched Sequences. *Nat. Struct. Mol. Biol.* **2012**, *19*, 623−627.
(279) Engel, J. D.; Von Hippel, P. H. Effects of Methylation on the Stability of Nucleic Acid Conformations. Studies at the Polymer Level. *J. Biol. Chem.* **1978**, *253*, 927−961.
(280) Engel, J. D.; von Hippel, P. H. Effects of Methylation on the Stability of Nucleic Acid Conformations: Studies at the Monomer Level. *Biochemistry* **1974**, *13*, 4143−4158.
(281) Roost, C.; Lynch, S. R.; Batista, P. J.; Qu, K.; Chang, H. Y.; Kool, E. T. Structure and Thermodynamics of N^6-Methyladenosine in RNA: A Spring-Loaded Base Modification. *J. Am. Chem. Soc.* **2015**, *137*, 2107−2115.
(282) Ren, A.; Rajashankar, K. R.; Patel, D. J. Fluoride Ion Encapsulation by Mg^{2+} Ions and Phosphates in a Fluoride Riboswitch. *Nature* **2012**, *486*, 85−89.
(283) Baker, J. L.; Sudarsan, N.; Weinberg, Z.; Roth, A.; Stockbridge, R. B.; Breaker, R. R. Widespread Genetic Switches and Toxicity Resistance Proteins for Fluoride. *Science* **2012**, *335*, 233−235.
(284) Bartel, D. P. Metazoan MicroRNAs. *Cell* **2018**, *173*, 20−51.
(285) Schirle, N. T.; MacRae, I. J. The Crystal Structure of Human Argonaute2. *Science* **2012**, *336*, 1037−1040.
(286) Nakanishi, K.; Weinberg, D. E.; Bartel, D. P.; Patel, D. J. Structure of Yeast Argonaute with Guide RNA. *Nature* **2012**, *486*, 368−374.
(287) Grimson, A.; Farh, K. K. H.; Johnston, W. K.; Garrett-Engele, P.; Lim, L. P.; Bartel, D. P. MicroRNA Targeting Specificity in Mammals: Determinants beyond Seed Pairing. *Mol. Cell* **2007**, *27*, 91−105.
(288) Nielsen, C. B.; Shomron, N.; Sandberg, R.; Hornstein, E.; Kitzman, J.; Burge, C. B. Determinants of Targeting by Endogenous and Exogenous MicroRNAs and siRNAs. *RNA* **2007**, *13*, 1894−1910.
(289) Elkayam, E.; Kuhn, C.-D.; Tocilj, A.; Haase, A. D.; Greene, E. M.; Hannon, G. J.; Joshua-Tor, L. The Structure of Human Argonaute-2 in Complex with miR-20a. *Cell* **2012**, *150*, 100−110.
(290) Filipowicz, W.; Bhattacharyya, S. N.; Sonenberg, N. Mechanisms of Post-Transcriptional Regulation by MicroRNAs: Are the Answers in Sight? *Nat. Rev. Genet.* **2008**, *9*, 102−114.
(291) Sheu-Gruttadauria, J.; Xiao, Y.; Gebert, L. F.; MacRae, I. J. Beyond the Seed: Structural Basis for Supplementary MicroRNA Targeting by Human Argonaute2. *EMBO J.* **2019**, *38*, No. e101153.
(292) Wee, L. M.; Flores-Jasso, C. F.; Salomon, W. E.; Zamore, P. D. Argonaute Divides Its RNA Guide into Domains with Distinct Functions and RNA-Binding Properties. *Cell* **2012**, *151*, 1055−1067.
(293) Brancati, G.; Großhans, H. An Interplay of miRNA Abundance and Target Site Architecture Determines miRNA Activity and Specificity. *Nucleic Acids Res.* **2018**, *46*, 3259−3269.
(294) Broughton, J. P.; Lovci, M. T.; Huang, J. L.; Yeo, G. W.; Pasquinelli, A. E. Pairing Beyond the Seed Supports MicroRNA Targeting Specificity. *Mol. Cell* **2016**, *64*, 320−333.
(295) Sheng, G.; Zhao, H.; Wang, J.; Rao, Y.; Tian, W.; Swarts, D. C.; van der Oost, J.; Patel, D. J.; Wang, Y. Structure-Based Cleavage Mechanism of Thermus Thermophilus Argonaute DNA Guide Strand-Mediated DNA Target Cleavage. *Proc. Natl. Acad. Sci. U. S. A.* **2014**, *111*, 652−657.
(296) Wang, Y.; Juranek, S.; Li, H.; Sheng, G.; Wardle, G. S.; Tuschl, T.; Patel, D. J. Nucleation, Propagation and Cleavage of Target RNAs in Ago Silencing Complexes. *Nature* **2009**, *461*, 754−761.
(297) Yuwen, T.; Huang, R.; Kay, L. E. Probing Slow Timescale Dynamics in Proteins Using Methyl ^1H CEST. *J. Biomol. NMR* **2017**, *68*, 215−224.
(298) Yuwen, T.; Sekhar, A.; Kay, L. E. Separating Dipolar and Chemical Exchange Magnetization Transfer Processes in ^1H-CEST. *Angew. Chem., Int. Ed.* **2017**, *56*, 6122−6125.
(299) Sekhar, A.; Rosenzweig, R.; Bouvignies, G.; Kay, L. E. Hsp70 Biases the Folding Pathways of Client Proteins. *Proc. Natl. Acad. Sci. U. S. A.* **2016**, *113*, E2794−E2801.
(300) Lundström, P.; Akke, M. Off-Resonance Rotating-Frame Amide Proton Spin Relaxation Experiments Measuring Microsecond Chemical Exchange in Proteins. *J. Biomol. NMR* **2005**, *32*, 163−173.
(301) Eichmüller, C.; Skrynnikov, N. R. A New Amide Proton $R_{1\rho}$ Experiment Permits Accurate Characterization of Microsecond Time-Scale Conformational Exchange. *J. Biomol. NMR* **2005**, *32*, 281−293.
(302) Ishima, R.; Wingfield, P. T.; Stahl, S. J.; Kaufman, J. D.; Torchia, D. A. Using Amide ^1H and ^{15}N Transverse Relaxation To Detect Millisecond Time-Scale Motions in Perdeuterated Proteins: Application to HIV-1 Protease. *J. Am. Chem. Soc.* **1998**, *120*, 10534−10542.
(303) Rangadurai, A.; Shi, H.; Al-Hashimi, H. M. Extending the Sensitivity of CEST NMR Spectroscopy to Micro-to-Millisecond Dynamics in Nucleic Acids Using High-Power Radio-Frequency Fields. *Angew. Chem., Int. Ed.* **2020**, *59*, 11262−11266.
(304) Su, Z.; Zhang, K.; Kappel, K.; Li, S.; Palo, M. Z.; Pintilie, G. D.; Rangan, R.; Luo, B.; Wei, Y.; Das, R.; et al. Cryo-EM Structures of Full-Length Tetrahymena Ribozyme at 3.1 Å Resolution. *Nature* **2021**, *596*, 603−607.
(305) Kappel, K.; Zhang, K.; Su, Z.; Watkins, A. M.; Kladwang, W.; Li, S.; Pintilie, G.; Topkar, V. V.; Rangan, R.; Zheludev, I. N.; et al. Accelerated Cryo-EM-Guided Determination of Three-Dimensional RNA-Only Structures. *Nat. Methods* **2020**, *17*, 699−707.
(306) Bonilla, S. L.; Sherlock, M. E.; MacFadden, A.; Kieft, J. S. A Viral RNA Hijacks Host Machinery Using Dynamic Conformational Changes of a tRNA-like Structure. *Science* **2021**, *374*, 955−960.
(307) Luchinat, E.; Barbieri, L.; Cremonini, M.; Banci, L. Protein In-Cell NMR Spectroscopy at 1.2 GHz. *J. Biomol. NMR* **2021**, *75*, 97−107.

https://doi.org/10.1021/acs.chemrev.1c00845
Chem. Rev. 2022, 122, 9357−9394

(308) Kovacs, H.; Moskau, D.; Spraul, M. Cryogenically Cooled Probes—A Leap in NMR Technology. *Prog. Nucl. Magn. Reson. Spectrosc.* **2005**, *46*, 131−155.
(309) Boeszoermenyi, A.; Chhabra, S.; Dubey, A.; Radeva, D. L.; Burdzhiev, N. T.; Chanev, C. D.; Petrov, O. I.; Gelev, V. M.; Zhang, M.; Anklin, C.; et al. Aromatic ^{19}F-^{13}C TROSY: A Background-Free Approach to Probe Biomolecular Structure, Function, and Dynamics. *Nat. Methods* **2019**, *16*, 333−340.
(310) Kitevski-LeBlanc, J. L.; Hoang, J.; Thach, W.; Larda, S. T.; Prosser, R. S. ^{19}F NMR Studies of a Desolvated Near-Native Protein Folding Intermediate. *Biochemistry* **2013**, *52*, 5780−5789.
(311) Kim, T. H.; Mehrabi, P.; Ren, Z.; Sljoka, A.; Ing, C.; Bezginov, A.; Ye, L.; Pomès, R.; Prosser, R. S.; Pai, E. F. The Role of Dimer Asymmetry and Protomer Dynamics in Enzyme Catalysis. *Science* **2017**, *355*, No. eeag2355.
(312) Hoang, J.; Prosser, R. S. Conformational Selection and Functional Dynamics of Calmodulin: A ^{19}F Nuclear Magnetic Resonance Study. *Biochemistry* **2014**, *53*, 5727−5736.
(313) Aramini, J. M.; Hamilton, K.; Ma, L.-C.; Swapna, G. V. T.; Leonard, P. G.; Ladbury, J. E.; Krug, R. M.; Montelione, G. T. ^{19}F NMR Reveals Multiple Conformations at the Dimer Interface of the Nonstructural Protein 1 Effector Domain from Influenza A Virus. *Structure* **2014**, *22*, 515−525.
(314) Overbeck, J. H.; Kremer, W.; Sprangers, R. A Suite of ^{19}F Based Relaxation Dispersion Experiments to Assess Biomolecular Motions. *J. Biomol. NMR* **2020**, *74*, 753−766.
(315) Liebau, J.; Tersa, M.; Trastoy, B.; Patrick, J.; Rodrigo-Unzueta, A.; Corzana, F.; Sparrman, T.; Guerin, M. E.; Mäler, L. Unveiling the Activation Dynamics of a Fold-Switch Bacterial Glycosyltransferase by ^{19}F NMR. *J. Biol. Chem.* **2020**, *295*, 9868−9878.
(316) Strickland, M.; Catazaro, J.; Rajasekaran, R.; Strub, M.-P.; O'Hern, C.; Bermejo, G. A.; Summers, M. F.; Marchant, J.; Tjandra, N. Long-Range RNA Structural Information via a Paramagnetically Tagged Reporter Protein. *J. Am. Chem. Soc.* **2019**, *141*, 1430−1434.
(317) Favier, A.; Brutscher, B. Recovering Lost Magnetization: Polarization Enhancement in Biomolecular NMR. *J. Biomol. NMR* **2011**, *49*, 9−15.
(318) Solyom, Z.; Schwarten, M.; Geist, L.; Konrat, R.; Willbold, D.; Brutscher, B. BEST-TROSY Experiments for Time-Efficient Sequential Resonance Assignment of Large Disordered Proteins. *J. Biomol. NMR* **2013**, *55*, 311−321.

https://doi.org/10.1021/acs.chemrev.1c00845
Chem. Rev. 2022, 122, 9357−9394